

Subwavelength High-Contrast Grating (HCG) and its Applications in Optoelectronic Devices

Ye Zhou



Electrical Engineering and Computer Sciences
University of California at Berkeley

Technical Report No. UCB/EECS-2008-172

<http://www.eecs.berkeley.edu/Pubs/TechRpts/2008/EECS-2008-172.html>

December 18, 2008

Copyright 2008, by the author(s).
All rights reserved.

Permission to make digital or hard copies of all or part of this work for personal or classroom use is granted without fee provided that copies are not made or distributed for profit or commercial advantage and that copies bear this notice and the full citation on the first page. To copy otherwise, to republish, to post on servers or to redistribute to lists, requires prior specific permission.

**Subwavelength High-Contrast Grating (HCG) and its Applications in
Optoelectronic Devices**

by

Ye Zhou

B.E. (Tsinghua University) 2003

A dissertation submitted in partial satisfaction of the

requirements for the degree of

Doctor of Philosophy

in

Engineering – Electrical Engineering and Computer Sciences

in the

Graduate Division

of the

UNIVERSITY *of* CALIFORNIA, BERKELEY

Committee in charge:

Professor Constance J. Chang-Hasnain, Chair
Professor Ming C. Wu
Professor Yuri Suzuki

Fall 2008

The dissertation of Ye Zhou is approved:

Professor Constance J. Chang-Hasnain, Chair

Date

Professor Ming C. Wu

Date

Professor Yuri Suzuki

Date

University of California, Berkeley

Fall 2008

Subwavelength High-Contrast Grating (HCG) and its Applications in Optoelectronic
Devices
© 2008

by Ye Zhou

ABSTRACT

Subwavelength High-Contrast Grating (HCG) and its Applications in Optoelectronic Devices

by

Ye Zhou

Doctor of Philosophy in Engineering – Electrical Engineering and Computer Sciences

University of California, Berkeley

Professor Constance J. Chang-Hasnain, Chair

Optical grating is a research topic with a long history. It has been extensively studied over the years due to its various applications in holography, spectroscopy, lasers, and many other optoelectronic devices. In this dissertation, we present a novel single-layer subwavelength high-index-contrast grating (HCG) which opens a new era in the study of grating. HCGs can serve as surface normal broadband ($\Delta\lambda/\lambda \sim 35\%$), high-reflectivity (>99%) mirrors, which can be used to replace conventional distributed Bragg reflectors (DBRs) in optical devices. Different designs of HCGs can also serve as narrow band, surface emitting, high-quality (Q) factor optical resonators or shallow angle reflectors. In this dissertation, we will review the recent advances in high-index-contrast grating and its applications in optoelectronic devices, including vertical-cavity surface-emitting lasers (VCSELs), high-Q optical resonators, and hollow-core waveguides.

We first present a novel HCG-based VCSEL where the conventional DBR mirror is replaced with a HCG-based mirror. A systematic and comprehensive review of the experimental and numerical simulation results is presented to demonstrate many desirable

attributes of HCG-based VCSELs, including polarization selection, transverse mode control and a large fabrication tolerance.

Next, we present an ultra-fast tuning, HCG-based tunable VCSEL. By integrating a mechanically movable actuator with a single-layer HCG as the VCSEL top mirror, precise, wide continuous wavelength tuning (~ 18 nm) was achieved at room temperature. The small footprint of the HCG enables each of the mechanical actuator dimensions to be scaled down by at least a factor of 10, resulting in a greater than 1000 times reduction in mass, and an increase in the mechanical resonant frequency. It also allows for a record-fast, HCG-based tunable VCSEL with a tuning time in the ~ 10 ns range to be obtained.

Besides the HCG-based VCSELs/tunable VCSELs, we also present a HCG-based surface normal high-Q resonator with a simulated Q-factor as large as 500,000 and an experimentally measured Q-factor of $\sim 14,000$. The unique feature of a high-Q with surface normal emission is highly desirable, as the topology facilitates a convenient and high output coupling with free-space or fiber optics. This feature is promising for array fabrication of lasers and filters, as well as high throughput sensor arrays.

In addition, we propose a HCG-based hollow-core waveguide design with an ultralow propagation loss of < 0.01 dB/m, three orders of magnitude lower than the lowest loss of the state-of-art chip-scale hollow waveguides. This novel HCG hollow-core waveguide design will serve as a basic building block in many chip-scale integrated photonic circuits, enabling system-level applications including optical interconnects, optical delay lines, and optical sensors.

Professor Constance J. Chang-Hasnain
Dissertation Committee Chair

To my family for their love and support

TABLE OF CONTENTS

TABLE OF CONTENTS.....	ii
LIST OF FIGURES	iv
ACKNOWLEDGEMENT	xi
CHAPTER 1 INTRODUCTION	1
1.1 HISTORY OF OPTICAL GRATINGS.....	1
1.2 GRATING THEORY	2
1.3 SUBWAVELENGTH GRATINGS.....	9
1.4 DISSERTATION OVERVIEW	11
CHAPTER 2 HIGH-CONTRAST GRATING (HCG).....	13
2.1 INTRODUCTION	13
2.2 HCG AS SURFACE NORMAL BROADBAND MIRRORS.....	17
2.2.1 TM-HCG and TE-HCG	18
2.2.2 Dimension Sensitivity.....	21
2.2.3 Scalability	27
2.3 HCG AS SURFACE NORMAL HIGH-Q RESONATORS	28
2.4 HCG AS SHALLOW ANGLE REFLECTORS.....	29
2.5 SUMMARY.....	32
CHAPTER 3 HCG-BASED VCSEL.....	33
3.1 INTRODUCTION	33
3.2 DESIGN.....	35
3.3 FABRICATION.....	38
3.4 OPTICAL CHARACTERISTICS.....	42
3.4.1 TM-HCG-based VCSEL.....	42
3.4.2 TE-HCG-based VCSEL.....	44
3.4.3 Near Field Characteristics.....	44
3.5 POLARIZATION CONTROL	46
3.5.1 Introduction.....	46
3.5.2 CW Polarization Control.....	46
3.5.3 Dynamic Polarization Control	49
3.5.4 Lithographically Defined Polarization	50
3.6 TRANSVERSE MODES CONTROL	52
3.6.1 Introduction.....	52
3.6.2 Oxide Aperture Dependence.....	54
3.6.3 Large Aperture Single Mode Device	58
3.6.4 HCG Size Dependence	60
3.7 LARGE FABRICATION TOLERANCE	65
3.7.1 Introduction.....	65
3.7.2 Simulation and Experiment.....	66
3.7.3 Dimension Tolerance for Uniform Gratings.....	67
3.7.4 Dimension Tolerance for Non-uniform Gratings.....	69
3.7.5 Lithography Alignment Tolerance.....	71

3.8 SUMMARY	72
CHAPTER 4 HCG-BASED TUNABLE VCSEL	74
4.1 INTRODUCTION	74
4.2 DESIGN.....	76
4.3 FABRICATION.....	78
4.4 OPTICAL CHARACTERISTICS.....	82
4.5 WAVELENGTH TUNING RANGE	85
4.5.1 Tuning Principle	85
4.5.2 Devices With 4 Pairs of p-DBR.....	86
4.5.3 Devices With 4 Pairs of p-DBR.....	88
4.6 WAVELENGTH TUNING SPEED.....	90
4.6.1 Measurement Method	90
4.6.2 TM-HCG-based Tunable VCSEL.....	91
4.6.3 TE-HCG-based Tunable VCSEL.....	92
4.6.4 Comparison.....	94
4.6 SUMMARY	95
CHAPTER 5 HCG-BASED SURFACE NOMRAL HIGH-Q RESONATOR	97
5.1 INTRODUCTION	97
5.2 DESIGN.....	99
5.2.1 Device Design and Simulation.....	99
5.2.2 Sensitivity Study and Applications.....	105
5.3 EXPERIMENT	107
5.4 SUMMARY	110
CHAPTER 6 HCG-BASED LOW LOSS HOLLOW-CORE WAVEGUIDE	112
6.1 INTRODUCTION	112
6.1 1D HCG HOLLOW-CORE WAVEGUIDE	114
6.2.1 Basic Principle	114
6.2.2 Designe and Simulation.....	117
6.2.3 Nonlinearity	122
6.2.4 Dispersion	123
6.2.5 Temperature Variation.....	124
6.3 2D HCG HOLLOW-CORE WAVEGUIDE	124
6.4 SUMMARY	126
CHAPTER 7 CONCLUSION.....	128
BIBLIOGRAPHY	130

LIST OF FIGURES

Figure 1.1 Schematic of a classic optical grating showing the phase relation between diffracted rays from two adjacent grooves.....	3
Figure 1.2 k-space schematic of the grating diffraction order wave vectors.....	5
Figure 1.3 Schematic for using the Rigorous Coupled-Wave Analysis (RCWA) method to solve a simple step-profile grating problem.	7
Figure 1.4 SEM image of some previous subwavelength grating work. (a) L.Zhuang, et al., <i>J. Vac. Sci. Technol. B</i> , 1996 [16]. (b) S. Goeman, et al., <i>IEEE Photon. Tech. Lett.</i> , 1998 [17]. (c) A. Haglund et al., <i>Electron. Lett.</i> , 2006 [18].	10
Figure 2.1 Schematic of the subwavelength high-contrast grating reflector based on a silicon-on-insulator (SOI) wafer designed for 1.55 μm center wavelength.....	14
Figure 2.2 Calculated reflectivity spectrum for the 1.55 μm SOI HCG structure using Rigorous Coupled Wave Analysis (RCWA) and finite difference time-domain (FDTD) methods. An extraordinarily broad ($\Delta\lambda/\lambda \sim 35\%$), high-reflectivity (>99%) spectrum is obtained from both methods, ranging from 1.33 μm to 1.80 μm	15
Figure 2.3 Calculated reflectivity spectrum comparison between a HCG (in red) and DBR (in gray). HCG provides reflectivity equivalent to 40 pairs of DBR, but with a much wider bandwidth and 10 \times thickness reduction.....	16
Figure 2.4 Schematic of (a) TM polarized and (b) TE polarized high-contrast grating (HCG). Red arrows show the light propagation directions. The black arrows attached to them show the E-field polarization directions.....	19
Figure 2.5 Calculated reflectivity spectra for surface-normal incident plane waves with E-field along x (blue) and y (red) directions for (a) TM- and (b) TE- HCG. The TM-HCG has a very high reflectivity for E-field aligned in x direction but significantly lower for y direction. The opposite is true for TE-HCG.....	20
Figure 2.6 Calculated reflectivity spectra as a function of grating period (Λ) for (a) TM-HCG (b) TE-HCG. The 99% reflectivity contour line is shown in black	23
Figure 2.7 Calculated reflectivity spectra as a function of grating duty cycle (η) for (a) TM-HCG (b) TE-HCG. The 99% reflectivity contour line is shown in black.	24
Figure 2.8 Calculated reflectivity spectra as a function of grating thickness (t) for (a) TM-HCG (b) TE-HCG. The 99% reflectivity contour line is shown in black.	25
Figure 2.9 Calculated reflectivity spectra as a function of incident angle for (a) TM-HCG (b) TE-HCG. The 99% reflectivity contour line is shown in black.....	26
Figure 2.10 Calculated reflected spectra for (a) a TM-HCG with grating period (Λ) = 380 nm, thickness (t) =235 nm, duty cycle (η) =65% and (b) a TM-HCG with grating period (Λ) = 3.8 μm , thickness (t) =2.35 μm , duty cycle (η) =65%. The reflection band shifts from 0.7-1 μm to 7-10 μm	27

Figure 2.11 Calculated reflectivity spectrum of HCG grating using RCWA shown in blue circles. Red curve is the fitted Fano resonance line shape.	28
Figure 2.12 Schematic of a HCG structure with oblique incident light. Two incident characteristic angles θ and φ are used to identify the incident direction. θ and φ are the angle between incident beam and y - z plane and the angle between incident beam and x - z plane, respectively.	30
Figure 2.13 Calculated reflectivity spectrum of HCG with grating period (Λ) = 665 nm, thickness (t) =410 nm, duty cycle (η) =46%, for $\theta=3^\circ$ and $\varphi=0^\circ$ TE polarized light.	31
Figure 2.14 Calculated reflectivity of HCG with grating period (Λ) = 665 nm, thickness (t) =410 nm, duty cycle (η) =46%, for 1550 nm TE polarized light, when θ and φ are scanned.	32
Figure 3.1 The cross-section schematic of HCG-based VCSEL. The top mirror consists of a freely-suspending HCG and M-pairs DBRs. M= 2 or 4.	36
Figure 3.2 Calculated TM-HCG-based mirror reflectivity for TM and TE polarized light. The reflectivity is also calculated for a grating with 0% and 100% duty cycles (η). $\eta = 0$ corresponds to no HCG layer, while $\eta = 100$ means an additional uniform layer of AlGaAs is used to provide extra reflectivity.	37
Figure 3.3 Fabrication process flow of a HCG-based VCSEL. (a) starting epitaxial wafer (b) top metal contact deposition (c) device mesa etch (d) bottom metal contact deposition (e) thermal oxidation (f) electron-beam lithography and reactive ion etching (RIE) (g) selective wet etching removing sacrificial layer and critical point drying. Step (a)-(e) are the same as a standard VCSEL process	38
Figure 3.4 (a) SEM image of fabricated HCG-integrated VCSEL, where the grating is aligned to the center of the device mesa. (b) Close-up SEM image of the freely-suspending grating, where a stress-relief trench is used to eliminate buckling of the grating. (c) Zoomed-in SEM image of the fabricated individual grating stripes..	41
Figure 3.5 (a) A HCG without the stress-relief trench. After sacrificial layer underneath the grating layer is removed, the some grating stripes buckle up due to the residual stress. (b) A HCG with a stress-relief trench after the sacrificial layer removal. The trench releases the residual stress in the material and the grating buckling issue is completely solved.....	42
Figure 3.6 (a) Optical characteristic of typical optical TM-HCG-based VCSEL showing output power versus input current (LI) and voltage versus current (VI) under room temperature. The device has a very low threshold current of 0.5 mA and an output power of ~1 mW. (b) Measured single-mode emission spectra under different bias currents, showing a 40 dB suppression of higher-order transverse modes.	43
Figure 3.7 (a) Optical characteristic of typical optical TE-HCG-based VCSEL showing output power versus input current (LI) and voltage versus current (VI) under room temperature. The device has a low threshold current of 1 mA and an	

output power of ~ 2 mW. (b) Measured single-mode emission spectrum under a bias current of 4 mA, showing a 45 dB suppression of higher-order transverse modes.....	44
Figure 3.8 Measured optical near-field beam profile of the TM-HCG-based VCSEL with integrated HCG top mirror. The optical emission has a symmetrical, fundamental mode Gaussian beam profile.....	45
Figure 3.9 Measured polarization-resolved light intensity-current (LI) characteristics for a TM-HCG-based VCSEL.....	47
Figure 3.10 Measured polarization-resolved optical spectra for a HCG VCSEL, with the polarizer rotated to the two orthogonal angles with respect to the grating stripes.....	48
Figure 3.11 Measured polarization-resolved optical spectra for a TM-HCG-based VCSEL under a large-signal on-off modulation.....	49
Figure 3.12 SEM image of the TM-HCG-based top mirrors, where gratings are patterned at different angles with respect to the [011] crystal axis.....	50
Figure 3.13 Measured polarization-resolved optical spectra of a HCG VCSEL, with the polarizer rotated to various angles with respect to the grating stripes.....	51
Figure 3.14 Measured spectral peak intensity as a function of the polarizer angle for four HCG-based VCSELs with their gratings patterned in different angles with respect to [011] crystal axis	52
Figure 3.15 (a) Measured optical emission spectra of TM-HCG VCSELs with $6 \times 6 \mu\text{m}^2$ grating top mirror and different oxide aperture sizes. All devices exhibit single fundamental mode emission with a SMSR between 40~45 dB. (b) Schematic of HCG-based VCSEL in this study. (c) SEM image of the $6 \times 6 \mu\text{m}^2$ TM-HCG.....	55
Figure 3.16 Finite difference time-domain (FDTD) simulation of mirror loss for 1st (solid) and 2nd (dotted) order modes of a $6 \mu\text{m}$ (9 period) TE-HCG and standard top DBR (24 pairs). The 2nd order mode sees high mirror loss and will not lase in HCG case, but will lase in apertures larger than $\sim 3 \mu\text{m}$ in a standard VCSEL structure.....	56
Figure 3.17 Measured emission spectra of TE-HCG-based VCSEL with $5.5 \mu\text{m}$ HCG size and DBR-based VCSEL with similar aperture size ($\sim 5 \mu\text{m}$). DBR-based device is highly multimode while HCG-based device is single mode.....	58
Figure 3.18 Measured optical emission spectra of TM-HCG VCSELs with $12 \times 12 \mu\text{m}^2$ grating top mirror and different oxide aperture sizes. A $10 \mu\text{m}$ aperture single mode HCG-based VCSEL is obtained.....	59
Figure 3.19 (a) The measured light intensity as a function of the injected current for a VCSEL with a $12 \times 12 \mu\text{m}^2$ HCG top mirror. (b) the emission septum for each device when biased at $1.2I_{\text{th}}$, $1.5I_{\text{th}}$, and $1.8I_{\text{th}}$. The HCG VCSEL operates in single mode (30 dB SMSR) despite having the large $10 \mu\text{m}$ oxide aperture.....	60

Figure 3.20 (a) SEM images of an ultra compact TM-HCG-based VCSEL utilizing a 4x4 μm^2 TM-HCG as the top mirror. (b) SEM image of the freely suspended TM-HCG, which consists of merely 11 Al _{0.6} Ga _{0.4} As grating stripes with a thickness of 230 nm.	61
Figure 3.21 SEM image of the freely suspended TE-HCG with only 4 periods or a size of 3 μm x 3 μm	62
Figure 3.22 SEM images of the fabricated (a) TM-HCG and (b) TE-HCG mirrors on VCSELs, each with a different grating area as shown. VCSELs with all these HCGs achieved single mode lasing condition	62
Figure 3.23 Optical characteristics for HCG VCSELs, showing the light intensity versus injected current for the set of identical TE-HCG VCSELs with different grating sizes and 2 μm oxide apertures.....	63
Figure 3.24 FDTD simulation of mirror loss for TE-HCGs at different finite grating sizes with two sizes of oxide apertures 2.5 μm and 3.0 μm . The HCG mirror loss is nearly constant until it has less than 4.8 μm (7 periods), indicating that the HCG does not require many periods to achieve high reflectivity.	64
Figure 3.25 Simulated top mirror reflectivity as a function of grating spacing and period for fixed $\lambda = 840$ nm. The white dots represent the combination of grating spacings and periods of the lasing TM-HCG-based VCSELs.	66
Figure 3.26 (a) Contour plot showing the relative parameters for four TM-HCG-based VCSELs with same period (392 nm) but with different grating spacing. (b) Measured spectra for fabricated TM-HCG-based VCSELs.	68
Figure 3.27 (a) Contour plot showing the relative parameters for four TM-HCG-based VCSELs with same grating spacing (94 nm) but with different grating periods. (b) Measured spectra for the fabricated TM-HCG-based VCSELs.	69
Figure 3.28 (a) SEM image of a non-uniform grating with random grating spacing. (b) Grating spacing distribution of the non-uniform grating. (c) LI curve of a HCG-based VCSEL with the non-uniform grating	70
Figure 3.29 (a) SEM image of a non-uniform grating with random grating periods. (b) Grating period distribution of the non-uniform grating. (c) LI curve of a HCG-based VCSEL with the non-uniform grating.	71
Figure 3.30 SEM image of a 12x12 μm^2 TM-HCG with an estimated aperture alignment tolerance window	72
Figure 4.1 Schematic of the HCG-based tunable VCSEL using the highly reflective subwavelength high-contrast grating as its top mirror, instead of conventional distributed Bragg reflectors.....	76
Figure 4.2 Schematic showing the cross-section epitaxial design of a HCG-based tunable VCSEL using the highly reflective HCG top mirror.	77
Figure 4.3 Fabrication process flow of a HCG-based tunable VCSEL. (a) starting epitaxial wafer (b) device mesa formation (c) thermal oxidation (d) top and back	

metal contact deposition (e) laser contact etch and deposition (f) electron-beam lithography and reactive ion etching (RIE) (g) selective wet etching removing sacrificial layer and critical point drying	79
Figure 4.4 SEM image of the fabricated TM-HCG-based tunable VCSEL.	80
Figure 4.5 SEM image of the freely suspended HCG mirror with a variety of MEM structure including (a) cantilever, (b) bridge, (c) folded-beam, and (d) membrane. ...	80
Figure 4.6 (a) SEM image of a fabricated TM-HCG with a grating thickness of 235 nm. (b) SEM image of a fabricated TE-HCG with a grating thickness of 145 nm. ...	81
Figure 4.7 SEM images of (a) a DBR-based tunable VCSEL and (b) a HCG-based tunable VCSEL.	82
Figure 4.8 Optical characteristic of typical optical TM-HCG-based tunable VCSEL with 2 pairs and 4 pairs p-doped DBR, showing output power versus input current (LI) and voltage versus current (VI) under room temperature. For the HCG-based tunable VCSEL with 2 pairs of p-doped DBR, a very low threshold current of 200 μ A is obtained	83
Figure 4.9 Measured single-mode emission spectrum for a TM-HCG-based tunable VCSEL, with a SMSR of 40 dB.	84
Figure 4.10 (a) Optical characteristic of typical optical TE-HCG-based tunable VCSEL showing output power versus input current (LI) under room temperature. The device has a low threshold current of 0.7 mA and an output power of >1.6 mW. (b) Measured single-mode emission spectrum when biased at twice the threshold current, showing a <40 dB SMSR	85
Figure 4.11 (a) CW tuning spectra for the TM-HCG-based tunable VCSEL with 4 pairs of p-DBRs under various external applied voltages across the HCG cantilever. (b) Measured emission wavelength as a function of applied external voltage and measured peak spectral intensity as a function of applied voltage.....	86
Figure 4.12 CW tuning spectra for the TE-HCG-based tunable VCSEL with 4 pairs of p-DBRs under various external applied voltages across the HCG cantilever	87
Figure 4.13 Measured continuous wavelength tuning spectra of a TM-HCG-based tunable VCSEL, with an 18 nm tuning range.	88
Figure 4.14 Measured laser threshold current and slope efficiency of the TM-HCG-based VCSEL under the corresponding emission wavelengths.....	89
Figure 4.15 Calculated wavelength tuning behavior of the TM-HCG-based tunable VCSEL (blue curves) and the TM-HCG reflection bandwidth (color-coded contour) as a function of the airgap thickness. The dotted white curve is the >99.9% reflection line.....	90
Figure 4.16 Optical setup used to characterize the mechanical frequency response for HCG structures, by using an optical spectrum analyzer to monitor the wavelength broadening under modulation.	91

Figure 4.17 Measured mechanical response of various HCG tuning structures by using an optical spectrum analyzer while modulating the mechanical actuator	92
Figure 4.18 Measured frequency response of TE-HCG-based tunable VCSELs with mirror sizes of 4×4, 6×6, 8×8 and 10×10 μm^2	93
Figure 4.19 Measured resonance and 3 dB frequency as a function of TE-HCG mirror size.	94
Figure 4.20 Calculated tuning speed and voltage as a function of mechanical beam length when utilizing different mirror structures (DBR, TM-HCG, and TE-HCG) integrated with different mechanical actuators: cantilever (solid) and membrane (dashed). The solid data points represent data obtained here and in references. Excellent agreements are obtained.....	95
Figure 5.1 Schematic of a HCG structure with TE polarized light incident from surface normal direction	99
Figure 5.2 Simulated reflectivity spectrum of HCG grating using RCWA shown in blue circles. Red curve is the fitted Fano resonance line shape. Q factor is ~500,000.	100
Figure 5.3 (a) Schematic of HCG high-Q resonator. (b) Schematic of middle HCG grating with three In _{0.2} Ga _{0.8} As quantum wells embedded inside grating layer. (c) Schematic of side mix-DBR grating mirror which is a combination of 1st-order and 3rd-order DBR gratings.....	101
Figure 5.4 Simulated electric field intensity profile in the HCG resonator using finite-difference time-domain (FDTD) method. Color is labeled in log scale. Q is estimated to be 500,000	102
Figure 5.5 Normalized electrical field decay as a function of time in the HCG resonator for different number of HCG periods (3 periods, 5 periods, 7 periods and 15 periods). Q is estimated to be 900, 4000, 17000 and 500000 respectively...	103
Figure 5.6 Simulated electric field intensity profiles in the HCG resonators with different number of HCG periods (3 periods, 5 periods, 7 periods and 15 periods). Q is estimated to be 900, 4000, 17000 and 500000 respectively.....	104
Figure 5.7 Simulation results for a HCG biosensor. The resonant wavelength red shift when biomolecule layers with different thicknesses are deposited onto the HCG structure.....	105
Figure 5.8 Simulation results for HCG resonant wavelength and Q factor as a function of temperature. Resonant wavelength only shifts 0.5 Å/K and the Q factor of the HCG cavity remains almost constant when temperature is changed from 0 °C to 100 °C.....	106
Figure 5.9 SEM images of (a) the top view and (b) the side view of a fabricated HCG high-Q resonator.	108
Figure 5.10 Emission spectrum of HCG resonator (in red) and emission spectrum in the area without grating (in blue). The inset shows a zoomed-in picture of the	

HCG emission spectrum. The FWHM of the HCG resonator emission peak is $\sim 0.07\text{nm}$ and Q is ~ 14000	109
Figure 5.11 Emission spectra of HCG resonator under $10\mu\text{W}$, $100\mu\text{W}$, $300\mu\text{W}$ optical pumping, respectively.....	110
Figure 6.1 Schematic of high contrast grating (HCG). High index gratings (blue) are surrounded by low index material, typically air. The incident angle, θ , is measured from the plane of the grating.....	114
Figure 6.2 (a) Schematic of a 1D HCG hollow-core slab waveguide structure consisting of two reflecting HCGs. (b) Ray optics model for guided mode in a hollow-core slab waveguide. Two reflective surfaces extend infinitely in the y - z plane and light propagates in the z direction. The spacing D between the planes forms the core of the waveguide. Light within the core can be expressed via a plane wave expansion, where the plane waves within the core are characterized by the wave vector k	115
Figure 6.3 Calculation of waveguide loss α (dB/m) at $1.55\ \mu\text{m}$ for a $15\text{-}\mu\text{m}$ core slab HCG-HW as a function of (a) grating period and semiconductor width (b) thickness and semiconductor width. 0.1dB/m and 0.01dB/m lines are labeled in the plots.....	117
Figure 6.4 Calculation of waveguide loss α (dB/m) at $1.55\ \mu\text{m}$ for a $15\text{-}\mu\text{m}$ core slab HCG-HW as a function of wavelength. 0.1dB/m and 0.01dB/m lines are labeled in the plots.....	118
Figure 6.5 Propagation loss of 1D slab HCG-HW vs θ for the first four TE modes in a $15\ \mu\text{m}$ HCG-HW. Due to symmetry, one can avoid launching into the second order mode. Hence the difference between the first and third order modes is the most important for modal screening. In this case, the loss of 3 rd mode (2 nd lowest odd order mode) is drastically higher, 200 times, than that of the 1st mode.....	119
Figure 6.6 Simulated electric field intensity profile of HCG-HW. Color is labeled in log scale. The field intensity outside the HCG-HW is only 10^{-8} of the intensity at the center of the hollow core.....	120
Figure 6.7 Normalized electrical field inside HCG-HW as a function of waveguide length. Linear regression is used to fit the curve as plotted in the red dash line. A waveguide propagation loss of $0.006\pm 0.0024\text{dB/m}$ with 95% fitting confidence bounds is obtained.....	121
Figure 6.8 Schematic of a 2D rectangular HCG-HW.....	124
Figure 6.9 Schematic of HCG cladding grating in 2D rectangular HCG-HW. There are two incident characteristic angles θ and ϕ , which are the angle between incident beam and y - z plane and the angle between incident beam and x - z plane, respectively.....	125
Figure 6.10 A round trip ray trace looking along the z axis direction. The sizes of the hollow core in x and y direction are D_x and D_y , respectively.....	126

ACKNOWLEDGEMENT

First, I would like to give special thanks to my advisor, Professor Connie Chang-Hasnain, for her guidance and support over the years. She has been an excellent advisor, as she is a great source not only of knowledge, experience, and insight, but also of encouragement and inspiration. Her dedication, vision, and passion have guided me through many tough times and helped me overcome countless obstacles. Without her guidance and mentorship, I don't think I could finish this work. In addition, I would like to thank Prof. Ming Wu, Prof. Yuri Suzuki, and Prof. Nathan Cheung for taking time to serve on my qualifying exam and dissertation committee, and for offering useful comments and advice.

Next, I would like to thank my former groupmate Mike Huang, with whom I worked collaboratively for four years. We spent countless days and nights together working in the lab and doing experiments, and I am very grateful for all his help, advice, and discussions. I would also like to thank all my co-workers: Chris Chase, Michael Moewe, Wendy Xiaoxue Zhao, Benjamin Cheng, Bala Pesala, Lukas Chrostowski, Johannes Kern, Vadim Karagodsky, and Forrest Sedgwick for all of their helpful discussions and collaborative work. I am also grateful to other current and former members of the Prof. Chang-Hasnain Optoelectronics group for their help and friendship: Chih-Hao Chang, Pei-Cheng Ku, Carlos Mateus, Zhangyuan Chen, Matthias Kuntz, Shanna Crankshaw, Linus Chuang, Devang Parekh, Roger Chen, Frank Yi Rao, Wilson Ko, Billy Ng, Thai-Truong Du Tran, and Weijian Yang.

In addition, I would like to thank the staff members of Berkeley Microfabrication Laboratory for their help and support. I would also like to thank Landmark Optoelectronic Corporation for helping us grow epitaxy wafers.

Lastly, I would like to thank my family for their love, support, and encouragement. Without them, my life would not have the meaning and purpose that it has now.

Chapter 1 Introduction

1.1 History of Optical Gratings

Optical grating is a research topic with a long history. It has been extensively studied over the years due to its wide applications in holography, spectroscopy, lasers, and many other optoelectronic devices.

Diffraction grating was discovered by James Gregory (1638-1675), a Scottish mathematician and astronomer, when he observed the diffraction patterns from passing sunlight through a bird feather. The first man-made diffraction grating was made in 1786 by an American astronomer, David Rittenhouse, who constructed a half-inch wide grating by wrapping fine wire around the threads of a pair of fine-pitch screws, with an approximate spacing of about 100 lines per inch [1]. However, Rittenhouse didn't develop this prototype further, or use it for serious scientific experiments, so instead it is the German physicist Joseph von Fraunhofer who deserves the credit for the invention of diffraction grating. Independently of Rittenhouse, Fraunhofer used a similar method to

develop a wire diffraction grating [2] in 1821. He also built the first ruling engine, and his research resulted in gratings of sufficient quality to enable him to measure the absorption lines of the solar spectrum-- now generally referred to as the Fraunhofer lines. He went on to explain the phenomenon of diffracted orders, and to derive and verify the grating equation; thus, he is credited with laying the foundation for the modern optical grating theory [3]. Since the manufacture tolerances required for an optical grating are quite small, usually a tiny fraction of the optical wavelength, in the early days of grating study they were manufactured by watchmakers, who were the only people with experience in working with such a high precision level and fine scale. In 1882, at Johns Hopkins University, U.S. physicist Henry Augustus Rowland constructed sophisticated ruling engines, which could fabricate gratings with much higher precision than anything available before. Rowland published a famous paper [4] in 1882, which opened up a new era of spectral analysis and established grating as the primary optical element of spectroscopic technology.

More than 180 years have passed since Fraunhofer first developed the grating theory. Today, gratings and other periodic structures have been widely used, not only in spectroscopy, but also in many other areas of science and engineering, such as: solid state physics, optoelectronics, acoustics, nonlinear optics, holography, and x-ray instrumentation.

1.2 Grating Theory

A classic optical grating is a 1D periodic structure consisting of a series of equally spaced grooves as shown in Figure 1.1. When light is incident onto the grating surface, it can be diffracted by the grooves. Each groove serves as a very small source of

reflected/transmitted light. There exists a unique set of angles where the light scattered from all the grooves is in phase and constructively interfere with each other. In Figure 1.1, a plane wave is incident at an angle θ_i with respect to the grating surface normal direction. For the light diffracted with an angle θ_d , the optical path difference between two adjacent grooves can be expressed as $\Lambda \sin \theta_i - \Lambda \sin \theta_d$, where Λ is the period of the grating. When this optical path difference equals to an integral multiple of the incident light wavelength, or $\Lambda \sin \theta_i - \Lambda \sin \theta_d = m\lambda$ $m = 0, \pm 1, \pm 2, \dots$, the light will be in phase and constructive interfere with each other. Therefore, the diffracted light in these angles will be enhanced. However, for all other angles, there will be destructive interference between the light diffracted from adjacent grooves and the diffracted light will be cancelled.

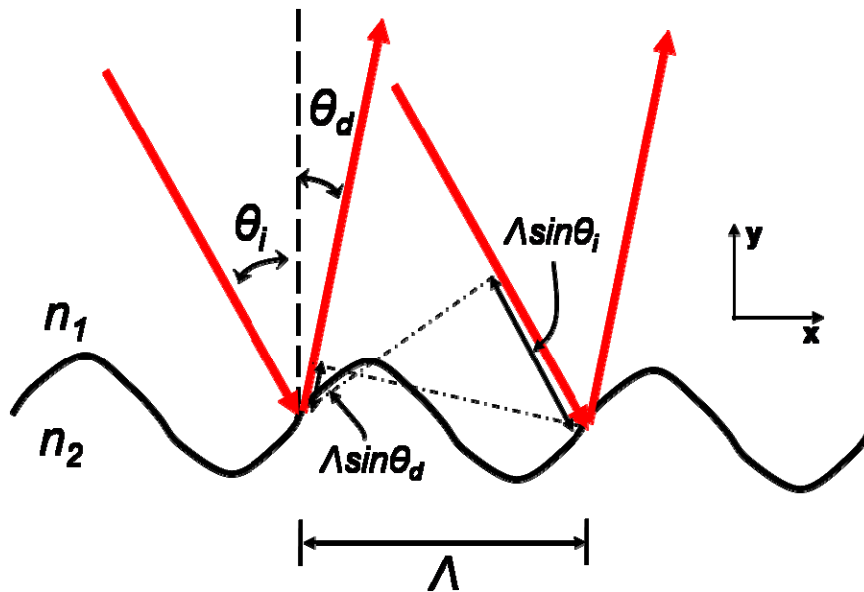


Figure 1.1 Schematic of a classic optical grating showing the phase relation between diffracted rays from two adjacent grooves

The above analysis shows that gratings can diffract incident light in a unique set of angles. This property of grating can be expressed in a simple equation, called the grating equation:

$$\sin \theta_{d,m} = \sin \theta_i + m \frac{\lambda}{\Lambda} \quad m = 0, \pm 1, \pm 2, \dots \quad (1.1)$$

where θ_i and $\theta_{d,m}$ are the angle between the incident light and the grating surface normal direction, and the angle between the m -th order diffraction light and the grating surface normal direction, respectively. λ is the wavelength, Λ is the period of the grating, and m is an integer that denotes the diffraction order. This equation assumes that the incident light is monochromatic and perfectly collimated (plane wave). However, if the incident light is non-monochromatic and non-collimated, for a linear media grating, the diffraction can be expressed as a superposition of the diffraction of all its plane-wave components using equation 1.1. When m is equal to zero, the grating acts as a simple reflective mirror and all wavelength components are superimposed. In the cases where $m \neq 0$, the angle of diffraction depends on the wavelength, and different wavelengths will be separated angularly.

In the case of transmission gratings, a similar equation can be derived to determine the propagation direction of the transmission orders as shown in the following equation 1.2:

$$n_2 \sin \theta_{t,m} = n_1 \sin \theta_i + m \frac{\lambda}{\Lambda} \quad m = 0, \pm 1, \pm 2, \dots \quad (1.2)$$

where $\theta_{t,m}$ is the angle between the m -th order transmission light and the grating surface normal direction. n_1 and n_2 are the refractive indices as shown in Figure 1.1.

We can transform both equation 1.1 and equation 1.2 into a general equation using wave vectors:

$$k_{m,x} = k_{i,x} + m \frac{2\pi}{\Lambda} \quad m = 0, \pm 1, \pm 2, \dots \quad (1.3)$$

where $k_{m,x}$ and $k_{i,x}$ are the diffracted and incident wave vectors in the x direction. Here we define the grating periodicity direction as the x direction. The quantity

$$K = \frac{2\pi}{\Lambda} \quad (1.4)$$

is defined as the grating wave number (or grating vector), which is inversely proportional to the grating period Λ .

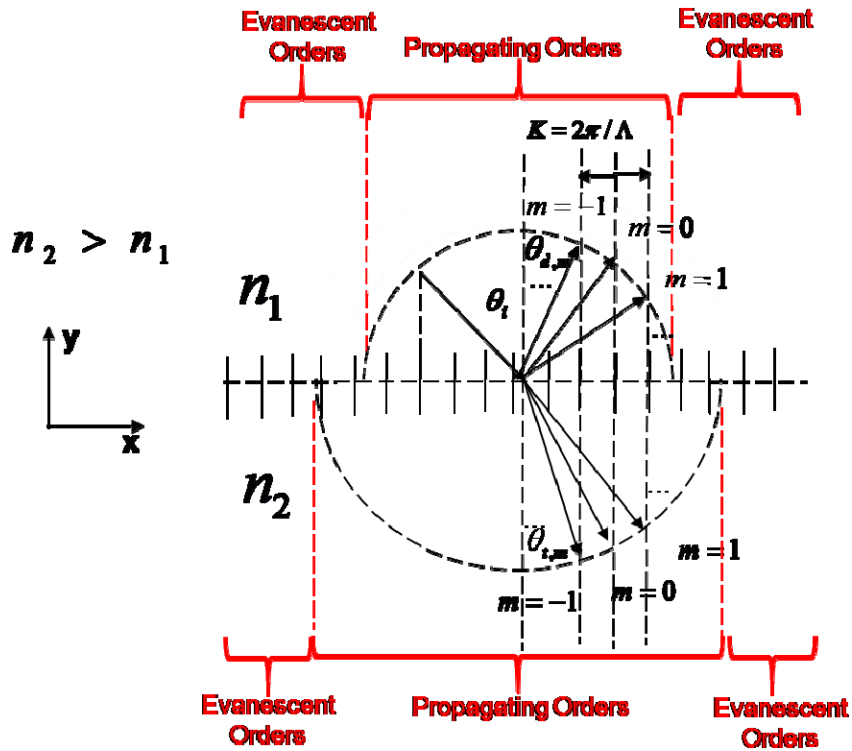


Figure 1.2 k -space schematic of the grating diffraction order wave vectors.

Figure 1.2 shows a k -space schematic of the grating diffraction order wave vectors in the x - y plane. θ_i , $\theta_{d,m}$, and $\theta_{r,m}$ are the incident angle, reflected diffraction angle, and transmitted diffraction angle, respectively. n_1 and n_2 are the refractive indices, and $n_1 > n_2$. The k vectors in the n_1 region end on a circle with a radius of $\frac{2\pi}{\lambda} n_1$ and k vectors in the n_2 region end on a circle with a radius of $\frac{2\pi}{\lambda} n_2$. For the adjacent diffraction orders, k vectors in x direction have a difference of $K = \frac{2\pi}{\Lambda}$.

In equations 1.1 and 1.2, for a given set of incident angles, grating period, and wavelength values, the grating equation can be satisfied for more than one value of m . However, only when $|\sin \theta_m| < 1$ is satisfied, will there be a solution(s) for θ_m . In this case, k_y is a real number and these diffraction orders are called propagation orders. However, in other orders, where $|\sin \theta_m| > 1$, k_y will become an imaginary number; these are evanescent orders. They have exponentially delayed fields in the y direction, thus they cannot be detected at a distance greater than a few wavelengths from the grating surface. However, they do play an important role in some surface-enhanced grating properties, and so must be taken into account in any electromagnetic theory of gratings. These orders also have very important applications, such as waveguide couple gratings.

Many grating theories and methods have been developed over the years to deal with all kinds of grating problems. Important ones include: Rayleth Theory [5], Differential Theory [6, 7], Method of Moharam and Gaylord (Rigorous Coupled-Wave Analysis) [8, 9], Classical Modal Method [10, 11], Integral Theory [12, 13], and Method of Coordinate Transformation [14, 15]. Among these theories and methods, Moharam and Gaylord's

Rigorous Coupled-Wave Analysis (RCWA) is one of the most widely used methods for accurate analysis of the diffraction of electromagnetic waves by periodic structures. In this dissertation, we will use RCWA as a primary analysis tool to design and analyze grating properties.

Here we will give a brief overview on how to use the Rigorous Coupled-Wave Analysis (RCWA) method to solve a simple grating problem. Figure 1.3 shows a simple grating with step-like profile. The grating is periodic and infinite in the x direction and is uniform and infinite in the y direction. In the z direction, it is divided into three regions: Region I with refractive index n_I , Region II with refractive index n_{II} , and the Grating Region, where the refractive index alters periodically between n_I and n_{II} with a period of Λ . The thickness of the Grating Region is d .

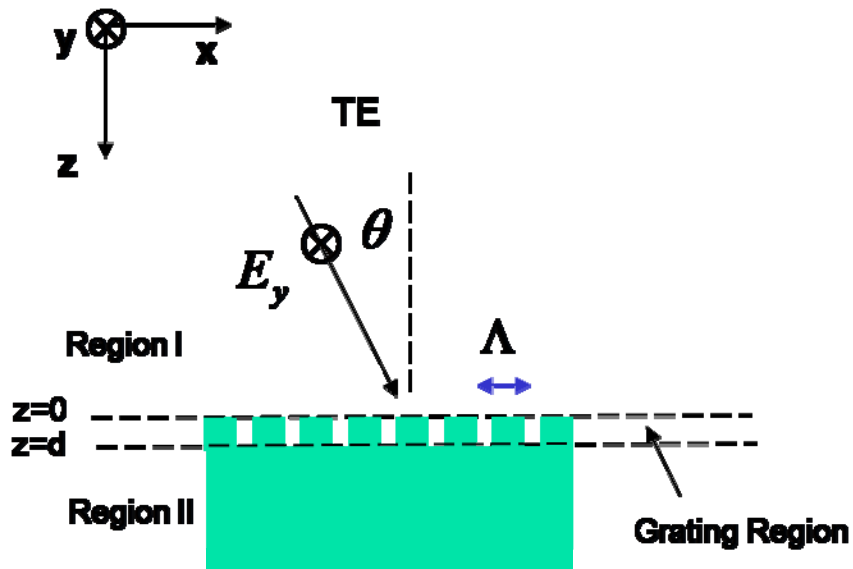


Figure 1.3 Schematic for using the Rigorous Coupled-Wave Analysis (RCWA) method to solve a simple step-profile grating problem.

In Figure 1.3, a transverse-electric (TE) polarized light is incident onto the grating surface with incident angle θ . TE polarization is defined as electric field (E-field) parallel

to the grating groove direction (the y direction in this case). We can write the normalized incident electric field as:

$$E_{inc,y} = \exp[-jk_0 n_I (\sin \theta \cdot x + \cos \theta \cdot z)] \quad (1.5)$$

where $E_{inc,y}$ is the normalized incident electric field, and k_0 is the wave vector in vacuum.

In Region I and Region II, the diffracted electric fields from the grating can be written in the following two equations:

$$E_{I,y} = E_{inc,y} + \sum_i R_i \exp[-j(k_{xi}x - k_{I,zi}z)] \quad (1.6)$$

$$E_{II,y} = \sum_i T_i \exp\{-j[k_{xi}x - k_{II,zi}(z-d)]\} \quad (1.7)$$

where: subscript i denotes the diffraction order number; k_{xi} is the x component of the the i -th order wave vector; $k_{I,zi}$ and $k_{II,zi}$ are the z components of the i -th order wave vector in Region I and Region II, respectively; R_i and T_i are the reflection and transmission coefficients of the i -th order diffraction. Based on the grating equation, k_{xi} can be written as:

$$k_{xi} = k_0 [n_I \sin \theta - i(\lambda_0 / \Lambda)] \quad (1.8)$$

In the Grating Region, the electric field can be written in following format:

$$E_{gy} = \sum_i S_{yi}(z) \exp(-jk_{xi}x) \quad (1.9)$$

where E_{gy} is the electric field in the Grating Region and $S_{yi}(z)$ is the normalized amplitude of the i -th wave field in the Grating Region.

To obtain the diffracted amplitudes of $S_{yi}(z)$, we can substitute equations 1.5-1.9 into the wave equation and we will get an infinite set of coupled-wave equations. By writing these equations in a linear system format, we can solve the eigenvalue problem. By

matching the boundary conditions at $z=0$ and $z=d$, R_i and T_i can be rigorously solved. The details of the derivation process can be found in reference [8].

Although the grating solved above has a step-like profile, for gratings with arbitrary profiles, we can divide the profile into many thin slides in the z direction. Similar analysis can be used to solve for the reflection and transmission coefficients of different diffraction orders. As long as the slides are thin enough, the step-like profile can serve as a good approximation for any profile form. Since the RCWA method is based on a state-variables representation, a unifying, easily computer-implementable matrix formulation can be achieved for general planar-grating diffraction problems.

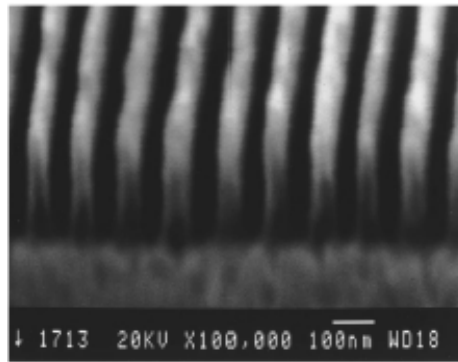
1.3 Subwavelength Gratings

Most diffraction gratings have a grating period larger than the optical wavelength. However, when the period of grating becomes smaller than the wavelength, the grating will exhibit many interesting behaviors, and many grating properties will need to be re-examined.

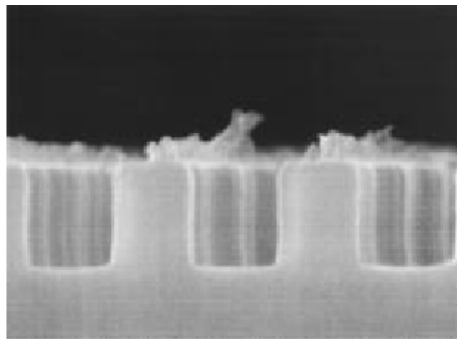
A grating with a period smaller than the wavelength is called a subwavelength grating. If light is incident normal onto a subwavelength grating surface, from grating equation 1.1 we can see that for any non-zero m value, $|\sin \theta_m| > 1$ will be satisfied. This means only the 0-th order diffraction exists as a propagation mode; all the higher diffraction orders are evanescent modes. The grating will basically serve as a simple mirror.

Several research groups studied subwavelength grating in the past a few years [16-18]. It has been reported that subwavelength gratings can be used to select the

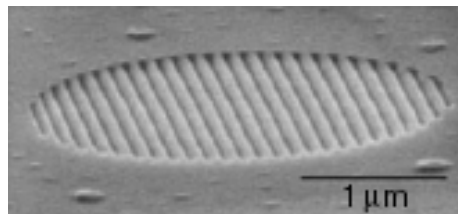
polarization and suppress higher order modes for the output light of vertical cavity surface emitting lasers (VCSELs) [16-18]. Figure 1.4 shows the scanning electron microscopy (SEM) images of these subwavelength gratings.



(a)



(b)



(c)

Figure 1.4 SEM image of some previous subwavelength grating work. (a) L.Zhuang, et al., *J. Vac. Sci. Technol. B*, 1996 [16]. (b) S. Goeman, et al., *IEEE Photon. Tech. Lett.*, 1998 [17]. (c) A. Haglund et al., *Electron. Lett.*, 2006 [18].

As shown in Figure 1.4, all these subwavelength gratings were fabricated on a substrate by dry etching technology. Since the etched surface only creates a refractive

index modulation on the substrate, there is no index contrast between the high index region of the grating and the substrate it sits on. In this dissertation, we will focus on another type of subwavelength grating: high-index-contrast subwavelength grating, or high-contrast grating (HCG), where the high index grating strips are completely surrounded by low index material. We will show that this novel grating structure has many unique properties with a wide range of applications.

1.4 Dissertation Overview

In this dissertation, we will present a novel single-layer subwavelength high contrast grating (HCG). HCG can serve as a surface normal broadband ($\Delta\lambda/\lambda \sim 35\%$), high-reflectivity ($>99\%$) mirror which can be used to replace a conventional distributed Bragg reflector (DBR). Different designs of HCG can also serve as a narrow band surface emitting high-quality (Q) factor optical resonators or a shallow angle reflector. In this dissertation, we will review the recent advances on high-index-contrast grating and its applications in optoelectronic devices, including vertical-cavity surface-emitting lasers (VCSELs), high-Q optical resonators, and hollow-core waveguides.

This dissertation is divided into the following sections. Chapter 2 will give an overview of different types of HCGs that can be used in different applications, including surface normal broadband mirrors, surface normal narrow band reflectors, and shallow angle reflectors. Chapter 3 shows the development of a novel HCG-based VCSEL by replacing a conventional DBR mirror with a HCG-based mirror. A systematic and comprehensive review of the experimental and numerical simulation results will be presented to demonstrate the many desirable attributes in HCG-based VCSELs, including polarization selection, transverse mode control, and a large fabrication tolerance. Chapter

4 shows the development of an ultrafast HCG-based tunable VCSEL. By integrating a mechanically movable actuator with a single-layer HCG as the VCSEL top mirror, precise and wide continuous wavelength tuning (~ 18 nm) was achieved at room temperature. The small footprint of HCG each of the mechanical actuator dimensions to be scaled down by at least a factor of 10, leading to a greater than 1000 times reduction in mass, and an increase in the mechanical resonant frequency. A HCG tunable VCSEL with tuning time in ~ 10 ns range is obtained. Chapter 5 reports a HCG-based surface normal high-Q resonator with a simulated Q-factor as large as 500,000 and an experimentally measured Q-factor $\sim 14,000$. The unique feature of high-Q with surface-normal emission is highly desirable, as the topology facilitates convenient and high output coupling with free-space or fiber optics. This feature is promising for array fabrication of lasers and filters, as well as for high throughput sensor arrays. Chapter 6 reports a HCG-based hollow core waveguide design with an ultralow propagation loss of < 0.01 dB/m, three orders of magnitude lower than the lowest loss of the state-of-art chip-scale hollow waveguides. This novel HCG hollow-core waveguide design will serve as a basic building block in many chip-scale integrated photonic circuits, enabling system-level applications, including optical interconnects, optical delay lines, and optical sensors. Finally in Chapter 7, we will summarize the entire dissertation.

Chapter 2 High-Contrast Grating (HCG)

2.1 Introduction

High-Contrast Grating (HCG) is a single-layer subwavelength grating where the refractive index contrast between the grating high index region and low index region is relatively high. In 2004, our group reported the first proposal of a subwavelength high-contrast grating that could be used as a surface normal broadband, high-reflectivity mirror [19]. Figure 2.1 shows a schematic of such a subwavelength HCG mirror. The HCG structure consists of a single layer of periodic grating structure with a highly refractive index material (e.g. AlGaAs or Si, labeled in blue) that is completely surrounded by low index material (e.g. air or oxide). The HCG design provides extraordinarily high reflectivity over a wide bandwidth for transverse-magnetic (TM) polarized light, with an electric field perpendicular to the grating incident from the surface-normal direction.

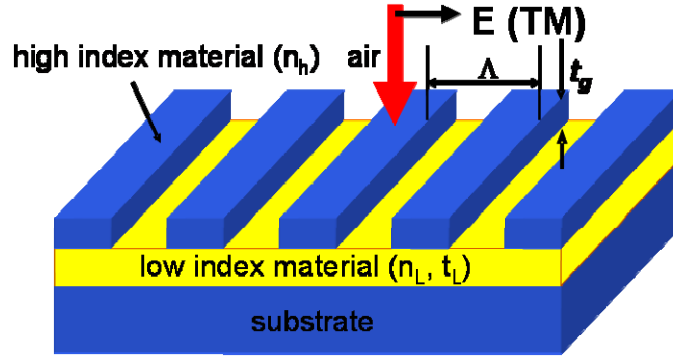


Figure 2.1 Schematic of the subwavelength high-contrast grating reflector based on a silicon-on-insulator (SOI) wafer designed for 1.55 μm center wavelength.

In Figure 2.1, the HCG consists of Si stripes (in blue), with air as the low index medium on top and between the stripes. Another low index material, SiO_2 (in yellow), is used below the gratings, as the structure could be easily fabricated on silicon-on-insulator (SOI) substrates. After choosing the high index and low index materials, the design parameters for the structure include the grating period (Λ), grating thickness (t_g), grating duty cycle (η), and the thickness of the low index layer under the grating (t_L). The duty cycle (η) is defined as the ratio of the width of the high index material with respect to the period. This SOI HCG is designed for 1.55 μm center wavelength, and the design parameters are: $n_{\text{substrate}} = 3.48$ (Si), $n_{\text{superstrate}} = 1$ (air), $n_H = 3.48$ (Si.), $n_L = 1$ (air), $n_L = 1.47$ (SiO_2), $\Lambda = 0.7 \mu\text{m}$, $t_g = 0.46 \mu\text{m}$ and $\eta = 0.75$.

The theoretical calculations were performed for this HCG structure using both Rigorous Coupled Wave Analysis (RCWA) [8] and finite difference time-domain (FDTD) methods [20, 21]. Figure 2.2 shows the calculated reflectivity spectrum for a TM polarized incident light from surface normal direction. The results from both calculation methods agree very well with each other, and an extraordinarily broad ($\Delta\lambda/\lambda \sim 35\%$), high-reflectivity ($>99\%$) spectrum, ranging from 1.33 μm to 1.80 μm , is obtained

from both RCWA and FDTD methods. For a higher reflectivity requirement ($R > 99.9\%$), the HCG mirror can still provide a very broad reflection bandwidth from 1.40-1.67 μm .

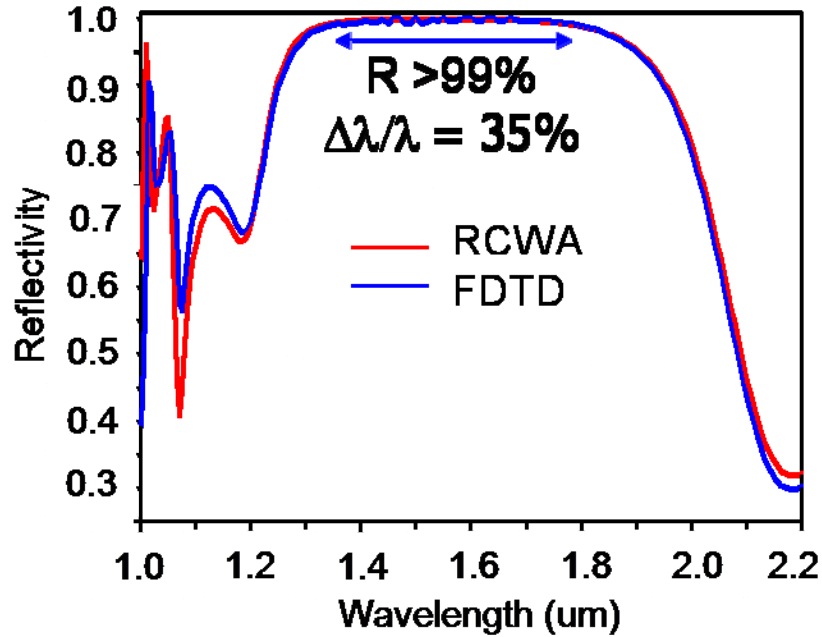


Figure 2.2 Calculated reflectivity spectrum for the 1.55 μm SOI HCG structure using Rigorous Coupled Wave Analysis (RCWA) and finite difference time-domain (FDTD) methods. An extraordinarily broad ($\Delta\lambda/\lambda \sim 35\%$), high-reflectivity ($>99\%$) spectrum is obtained from both methods, ranging from 1.33 μm to 1.80 μm .

As a comparison, the reflectivity spectrum of a $\sim 5\mu\text{m}$ DBR with 40 pairs of GaAs/ $\text{Al}_{0.9}\text{Ga}_{0.1}\text{As}$ alternating layers is plotted together with the reflectivity spectrum of HCG in Figure 2.3. For a fair comparison, the wavelengths of both reflectivity spectra are normalized to 1. As shown in Figure 2.3, HCG can provide reflectivity equivalent to 40 pairs of DBR, but with a much wider bandwidth and $10\times$ thickness reduction. In addition, unlike DBR structure, HCG only provides high reflectivity for one polarization, which is very desirable for many applications such as VCSEL mirrors.

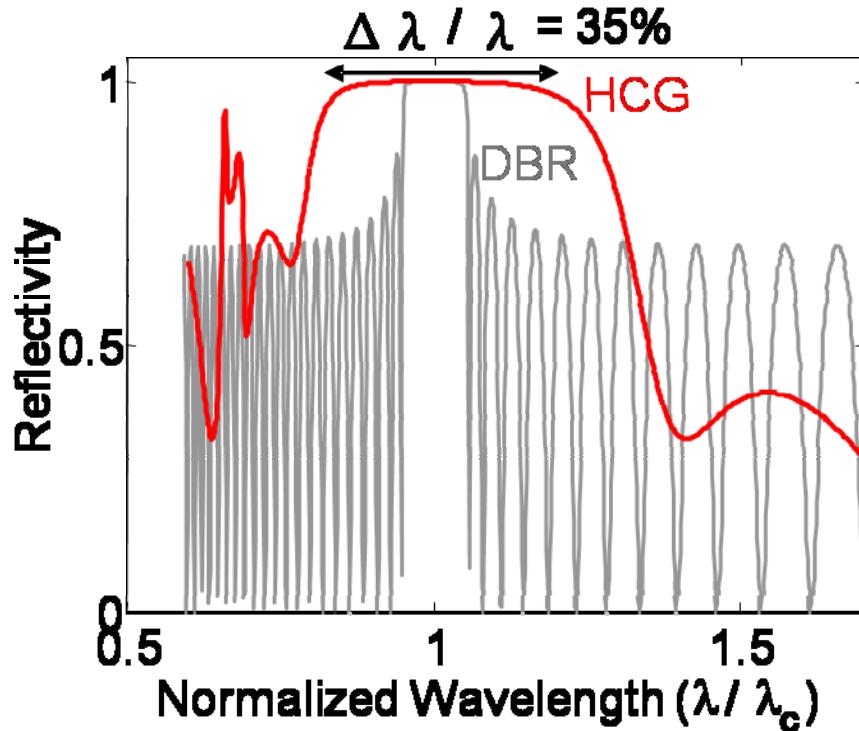


Figure 2.3 Calculated reflectivity spectrum comparison between a HCG (in red) and DBR (in gray). HCG provides reflectivity equivalent to 40 pairs of DBR, but with a much wider bandwidth and 10× thickness reduction.

Shortly after the proposal of the first HCG structure, our group carried out experimental work together with Prof. Yuri Suzuki and her former student Dr. Lu Chen at Cornell University. A silicon/silicon dioxide based HCG structure was fabricated, and a broadband (1.12-1.62 μm), high reflectivity ($R > 98.5\%$) HCG mirror for TM polarized light was experimentally demonstrated [22].

The proposal of the first HCG broadband mirror opens a new era in subwavelength grating study. We believe the extraordinarily broad band and the high reflectivity from the HCG are the results of the unique arrangement of high-index gratings that are completely surrounded by low-index media. However, as we will show in the rest of this chapter, HCG structure is far more than just a surface normal TM polarized broadband

mirror. By carefully designing and optimizing the dimensions of the grating structure, HCG can achieve very different functionalities and can be used in a wide range of applications.

In this chapter, we will give a comprehensive review on different types of HCGs. First, we will look at the HCG designs that can be used as surface normal broad band high-reflectivity mirrors for both TM polarized light and TE polarized light. Then, we will look at HCG designs which can be used as surface normal narrow-band reflectors or high-Q resonators. Finally, we will look at the HCG designs as shallow angle reflectors. We will go over the design processes of different types of HCGs and study many useful properties of the HCG structure, including polarization dependence, dimension sensitivity, and wavelength scalability.

2.2 HCG As Surface Normal Broadband Mirrors

Broadband mirrors with very high reflectivity have a wide range of applications in optoelectronics, including semiconductor lasers, optical filters, and tunable optical devices. Metal mirrors have very wide reflection bands, but due to the high absorption loss of the metals, most metal mirrors cannot achieve reflectivity larger than 99%. They are also not suitable for mirrors which require transmission applications. The distributed Bragg reflector (DBR), which consists of multiple layers of alternating dielectric materials with periodic variation of refractive indices, has been widely used as the high-reflectivity mirrors in most surface emitting lasers [23, 24]. However, due to the relatively small available index contrast in a lattice matching system, a large number of DBR pairs are required to achieve high reflectivity, which leads to epitaxial challenges in many material systems. As we will show in this section, HCG structure can be an ideal

structure to serve as a broadband ($\Delta\lambda/\lambda > 15\%$), high-reflectivity ($R > 99\%$) mirror with ONE single layer.

2.2.1 TM-HCG and TE-HCG

Figure 2.4 shows the schematic of the proposed broadband high-reflectivity HCG structures. Before we discuss the details in the HCG designs, it is necessary to distinguish between the two cases of polarization for a grating. If the incident wave is linearly polarized and the electric field vector is perpendicular to the grating stripe direction (perpendicular to the y direction in this case), both the reflected and transmitted lights have the same polarization. It is called TM polarization. In the other case, when the electric field is parallel to the grating stripe direction (parallel to the y direction), both the reflected and transmitted lights also preserve the polarization direction, and this is called TE polarization. Any other polarization state can be represented as a linear combination of the two fundamental polarizations. Therefore, it is only necessary to investigate the HCG response for these two polarizations.

We call the HCGs that can serve as broadband high-reflectivity mirrors for TM polarized light TM-HCGs, and the ones that can serve as broadband high-reflectivity mirrors for TE polarized light TE-HCGs. In Figure 2.4 (a) and (b), we show examples of TM-HCG and TE-HCG designs, respectively. These HCGs are designed for 850-nm wavelength and consist of periodic $\text{Al}_{0.6}\text{Ga}_{0.4}\text{As}$ stripes as the high index material, surrounded by air as the low index material. For TM-HCG, the grating parameters are: the period (Λ) = 380 nm, spacing (a) = 130 nm and thickness (t) = 235 nm. For TE-HCG, the grating parameters are: the period (Λ) = 620 nm, spacing (a) = 400 nm and thickness (t) = 140 nm. Although we use $\text{Al}_{0.6}\text{Ga}_{0.4}\text{As}$ /air as an example here in designing the

broadband HCG mirrors, the basic principle can be applied to almost all systems with high refractive index contrast, such as Si/air/SiO₂, GaAs/Al₂O₃, GaN/air, and ZnSe/CaF₂. In general, the larger the index contrast is, the broader band it is possible to achieve.

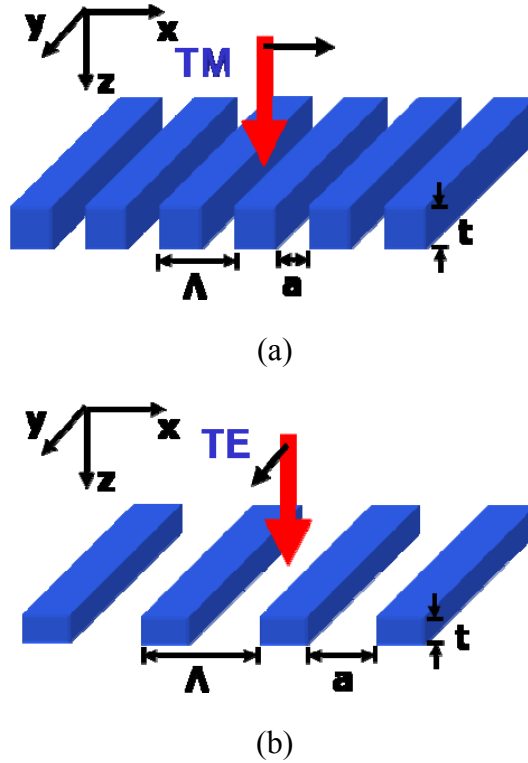
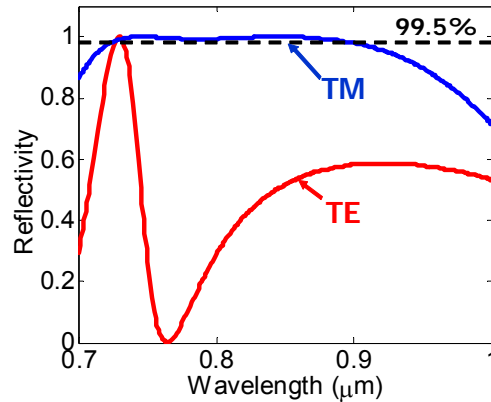


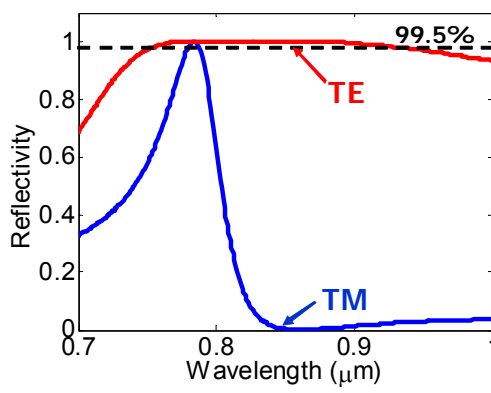
Figure 2.4 Schematic of (a) TM polarized and (b) TE polarized high-contrast grating (HCG). Red arrows show the light propagation directions. The black arrows attached to them show the E-field polarization directions.

The reflectivity spectra for E-fields parallel (TE) and perpendicular (TM) to the grating direction (y) for TM- and TE- HCGs are calculated using rigorous coupled wave analysis (RCWA), as shown in Figure 2.5. In this calculation, the index of refraction is assumed to be constant over the wavelength range, and optical loss is neglected (imaginary part of refractive index is 0), which is a reasonable approximation for the considered wavelength range. In Figure 2.5, the reflectivity spectra for TM and TE polarized light are plotted in blue and red, respectively. As shown here, if the reflectivity

is optimized for one E-field orientation (e.g. 99.5%), the reflectivity for the other direction can be significantly lower, e.g. <60%. This shows that the HCG structure has a very strong polarization dependence. This property is very useful in applications that require polarization selection, such as surface-emitting lasers.



(a)



(b)

Figure 2.5 Calculated reflectivity spectra for surface-normal incident plane waves with E-field along x (blue) and y (red) directions for (a) TM- and (b) TE-HCG. The TM-HCG has a very high reflectivity for E-field aligned in x direction but significantly lower for y direction. The opposite is true for TE-HCG.

The best way to visualize the high reflectivity is by the fact that, due to large index contrast and the need of matched boundary conditions, the incident plane wave excites in-

plane k-vectors immediately after entering the grating. The in-plane waves (modes) cannot propagate in the in-plane direction due to a large stop-band arising from a large index contrast. The thickness of the grating can be chosen so that these modes are canceled at the exiting plane of $z=t$. The incident light does not have any diffraction order (due to the subwavelength period). It also cannot couple to in-plane propagation or propagate through the grating, and thus must reflect nearly 100%.

It is worth noticing that for the same wavelength, TE-HCG has a much thinner thickness than the TM-HCG. The reason for this may be the larger effective index for TE polarized grating. By simple boundary condition considerations and spatial weighting of the electrical and displacement fields [15], the effective relative permittivity for TM polarized light and TE polarized light for gratings in Figure 2.4 can be calculated as

$$\varepsilon_{TM} = \frac{\varepsilon}{\eta + \varepsilon(1 - \eta)} \text{ and } \varepsilon_{TE} = 1 + \eta(\varepsilon - 1),$$

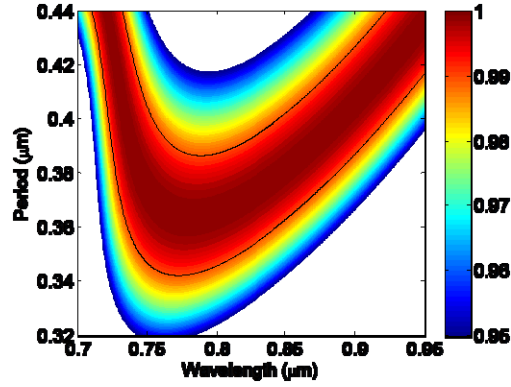
where ε is the relative permittivity for high index material, and η is the grating duty cycle defined as the ratio of the width of the high index material with respect to the period. It can be easily shown that the effective relative permittivity (square of the effective index) for TE polarized light is larger than the effective relative permittivity for TM polarized light. Therefore, TE-HCG, as a grating structure that is optimized for strong TE light reflection, can have a thinner thickness than that of TM-HCG.

2.2.2 Dimension Sensitivity

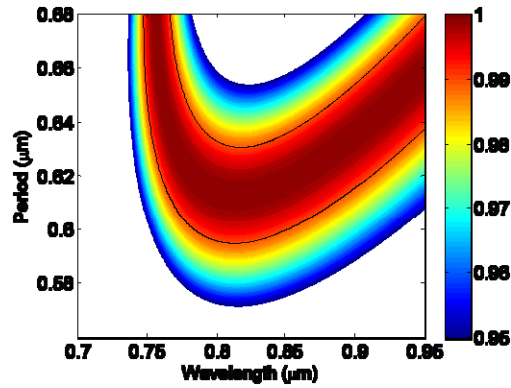
In a HCG design, important design parameters include grating period (Λ), grating thickness (t), and grating duty cycle (η). In this section, we study how the HCG reflectivity spectrum varies when we change these parameters. We will show design-

sensitive analysis by varying one parameter at a time, while keeping the others constant. We will study dimension sensitivity for both TM-HCG and TE-HCG, whose designs are the same as described in Section 2.2.1.

The grating period (Λ) sensitivity study is shown in Figure 2.6 for both TM-HCG and TE-HCG. In this study, we fix TM-HCG grating parameters at $\eta = 65\%$ and $t = 235$ nm and scan the grating period (Λ) from 320 nm to 440 nm. For TE-HCG, we fix the grating parameters at $\eta = 35\%$ and $t = 140$ nm, and scan the grating period (Λ) from 560 nm to 680 nm. For both HCGs, the high index material is $\text{Al}_{0.6}\text{Ga}_{0.4}\text{As}$, with the refractive index $n=3.2137$, and the low index material is air with $n=1$. Figure 2.6 shows the calculated reflectivity spectra as a function of grating period (Λ), using RCWA for both TM- and TE-HCG. The 99% reflectivity contour line is shown in black. As shown in Figure 2.6, both TM- and TE-HCG can tolerate at least 40 nm variation in a period while still maintaining a high reflectivity $>99\%$. Grating period can usually be controlled accurately in most deep UV lithography or e-beam lithography systems as well as in nano-imprint systems. Therefore, a 40 nm fabrication tolerance is more than enough for most systems, and high reflectivity can be easily achieved.



(a)

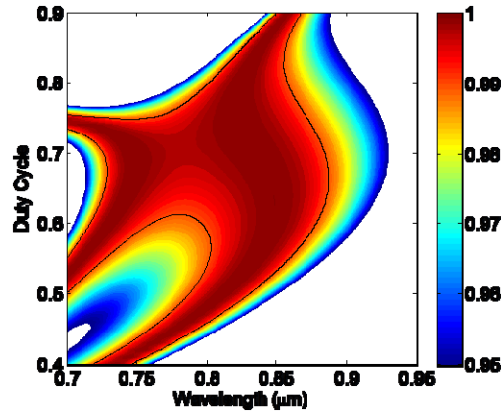


(b)

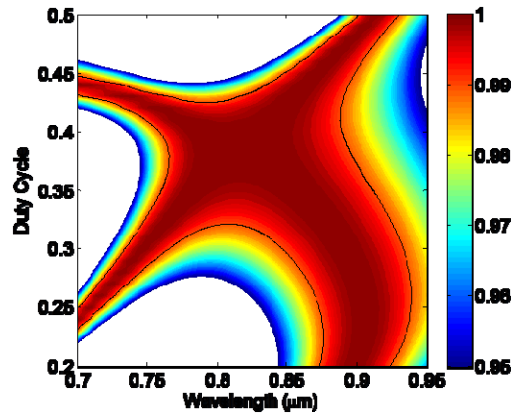
Figure 2.6 Calculated reflectivity spectra as a function of grating period (Λ) for (a) TM-HCG (b) TE-HCG. The 99% reflectivity contour line is shown in black.

The duty cycle (η) sensitivity study is shown in Figure 2.7. In this study, we fix TM-HCG grating parameters as $\Lambda = 380$ nm and $t = 235$ nm and scan the duty cycle (η) from 40% to 90%. For TE-HCG, then we fix the grating parameters as $\Lambda = 620$ nm and $t = 140$ nm and scan the duty cycle (η) from 20% to 50%. Figure 2.7 shows the calculated reflectivity spectra as a function of duty cycle (η) using RCWA for both TM- and TE-HCG. The 99% reflectivity contour line is again plotted in black. As shown in Figure 2.7 (a), TM-HCG can tolerate duty cycle variation from 55% to 85% at a wavelength of 850 nm. This translates into a grating air spacing variation from 55 nm to 170 nm. Compared

to the designed air spacing value of 130 nm, this is a $\pm 40\%$ fabrication tolerance window. Since the air spacing value is the smallest fabrication dimension in TM-HCG, having a large fabrication tolerance window is extremely important to achieve a high-yield HCG fabrication with low cost, high throughput process, such as nano-imprint or deep UV lithography technology. For TE-HCG, duty cycle variation at 850 nm can be from 30% to 45%, or a 90 nm air spacing fabrication tolerance window to achieve 99% reflectivity. This window is also large enough for many lithography systems.

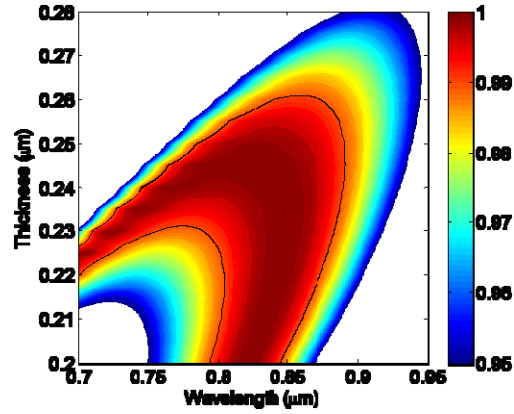


(a)

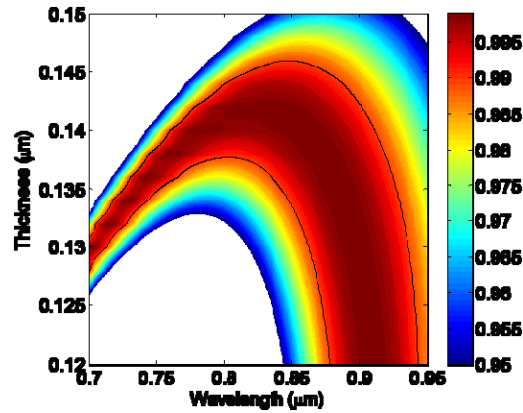


(b)

Figure 2.7 Calculated reflectivity spectra as a function of grating duty cycle (η) for (a) TM-HCG (b) TE-HCG. The 99% reflectivity contour line is shown in black.



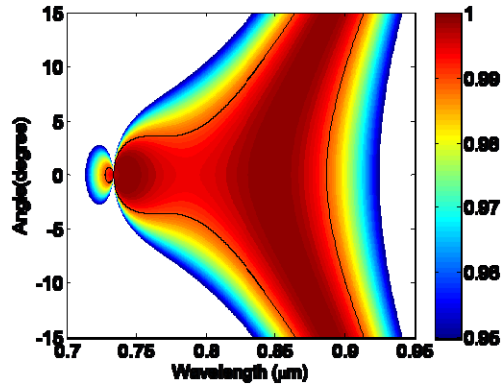
(a)



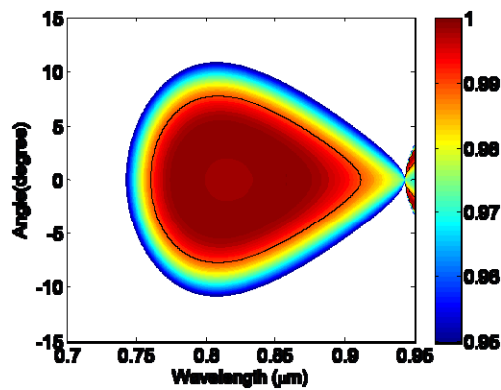
(b)

Figure 2.8 Calculated reflectivity spectra as a function of grating thickness (t) for (a) TM-HCG (b) TE-HCG. The 99% reflectivity contour line is shown in black.

Similarly, the sensitivity of grating thickness (t) has also been studied. In this study, we fix the TM-HCG grating parameters at $\Lambda = 380$ nm and $\eta = 65\%$ and scan the grating thickness (t) from 200 nm to 280 nm. For TE-HCG, we fix the grating parameters at $\Lambda = 620$ nm and $\eta = 35\%$ and scan the grating thickness (t) from 120 nm to 150 nm. As shown in Figure 2.8, a reasonable tolerance can be obtained for both HCGs.



(a)



(b)

Figure 2.9 Calculated reflectivity spectra as a function of incident angle for (a) TM-HCG (b) TE-HCG. The 99% reflectivity contour line is shown in black.

All of the discussions above assume the light is incident on the grating in surface normal direction. However, for many applications, the HCG needs to provide high reflectivity for incident waves with the k -vector deviating from surface-normal. In laser applications, the incident angle tolerance is determined by the beam divergence angle. In many passive device applications, the incident angle tolerance is determined by the numerical aperture of the focusing lens. Figure 2.9 shows the reflectivity spectra as the angle of the incident optical source deviates from surface normal for both TM- and TE-HCG. The 99% reflectivity contour line is again shown in black. For TM-HCG design, an

incident angle up to ± 10 degrees can be tolerated at 850nm. For TE-HCG, the angular tolerance is about ± 6 degrees.

2.2.3 Scalability

One nice property of HCG is that it is scalable with wavelength. Figure 2.10 (a) shows the calculated reflectivity spectra for a TM-HCG with grating period (Λ) = 380 nm, thickness (t) =235 nm, and duty cycle (η) =65%. Figure 2.10 (b) shows a calculated reflectivity spectra for a TM-HCG with grating period (Λ) = 3.8 μm , thickness (t) =2.35 μm , and duty cycle (η) =65%. By simply multiplying the dimensions by a constant, in this case 10, while keeping the other parameters the same, the reflection band shifts from 0.7-1 μm to a 7-10 μm wavelength range with all features and values being identical. Therefore, we can easily design HCG in other wavelength regimes by scaling wavelength, as long as the refractive index doesn't change much. Although we used TM-HCG as an example here, this wavelength scalability applies to all other HCG designs.

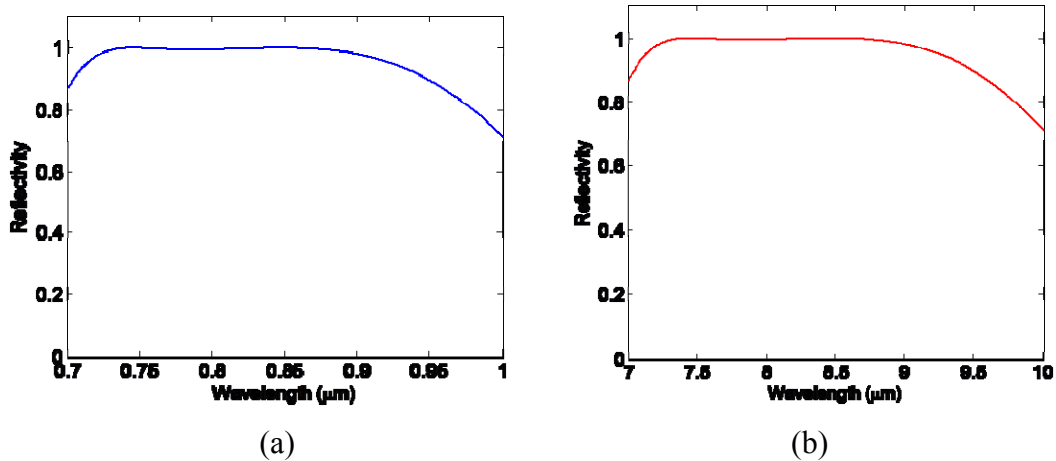


Figure 2.10 Calculated reflected spectra for (a) a TM-HCG with grating period (Λ) = 380 nm, thickness (t) =235 nm, duty cycle (η) =65% and (b) a TM-HCG with grating period (Λ) = 3.8 μm , thickness (t) =2.35 μm , duty cycle (η) =65%. The reflection band shifts from 0.7-1 μm to 7-10 μm .

2.3 HCG As Surface Normal High-Q resonators

In the previous section, we discussed designing HCG as a broadband mirror. In this section, we will show that by properly designing the dimensions of the HCG, it can also work as a narrow-band mirror or a high-Q resonator. The detailed discussion on this topic will be presented in Chapter 5 of this dissertation.

The narrow-band mirror we present here is designed for 1550 nm. The grating high index material is $\text{Al}_{0.6}\text{Ga}_{0.4}\text{As}$ with refractive index $n=3.0789$ at 1550 nm. The low index material is air with $n=1$. The grating is designed for TE polarized light. The HCG parameters are grating period (Λ) = 812 nm, thickness (t) = 625 nm, duty cycle (η) = 64%. The reflectivity spectrum of this HCG structure is calculated using RCWA as shown in blue circles in Figure 2.11. We obtain a reflectivity spectrum with a sharp asymmetric line shape whose reflectivity varies from 0 to 1 over a very narrow wavelength range.

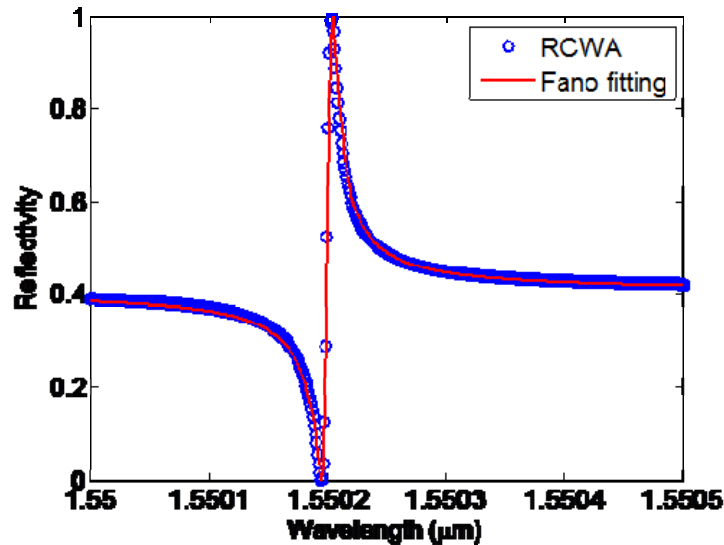


Figure 2.11 Calculated reflectivity spectrum of HCG grating using RCWA shown in blue circles. Red curve is the fitted Fano resonance line shape.

This asymmetric resonance has been previously reported in photonic crystals and is referred to as Fano resonance [26]. It is the result of interference between the normal incidence beam and the in-plane resonance of the HCG. The Q factor of the resonance can be extracted by fitting the simulated reflectivity spectrum with the following Fano-resonance equation [26]:

$$R = \frac{r^2(\omega - \omega_0)^2 + t^2(1/\tau)^2 - 2rt(\omega - \omega_0)(1/\tau)}{(\omega - \omega_0)^2 + (1/\tau)^2} \quad (2.1)$$

where ω_0 and τ are the center frequency and the lifetime of the resonance, and r and t are the electric field reflectivity and transmittance of a uniform slab with the same thickness as the HCG layer and with an effective dielectric constant. The Q factor of the resonance can be calculated using $Q = \omega_0\tau$. The red curve in Figure 2.11 shows the fitted Fano-resonance curve based on equation 2.1. The extracted Q factor in this case is calculated to be $\sim 360,000$.

Higher Q values ($>500,000$) can be obtained by further fine-tuning of the structure. In Chapter 5 of this dissertation, we will discuss using the HCG structure as a high-Q optical resonator and its applications in details. We will also present some experimental results on this topic.

2.4 HCG As Shallow Angle Reflectors

All the HCG structures discussed so far are designed for surface normal operation. However, in many applications, a broadband high-reflectivity mirror for an oblique incident beam is required. In fact, by changing the dimensions of the HCG structure, we can optimize the HCG structure as a high-reflectivity mirror for almost any incident angle. In this section, we will present HCG designs that are optimized for shallow angle

reflection. This type of HCG is very useful in designing ultra-low loss hollow-core waveguides, which will be discussed in detail in Chapter 6.

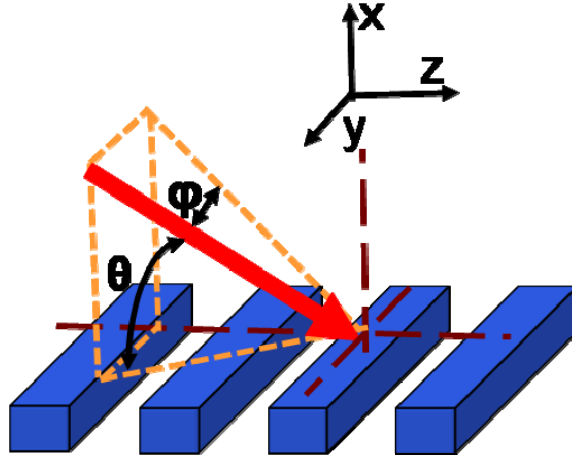


Figure 2.12 Schematic of a HCG structure with oblique incident light. Two incident characteristic angles θ and ϕ are used to identify the incident direction. θ and ϕ are the angle between incident beam and y - z plane and the angle between incident beam and x - z plane, respectively.

Figure 2.12 shows a schematic of a HCG structure with oblique incident light. Two incident characteristic angles, θ and ϕ , are used to identify the incident direction. θ and ϕ are the angle between the incident beam and the y - z plane, and the angle between the incident beam and the x - z plane, respectively. For specific θ and ϕ , high reflectivity can be obtained by optimizing the grating dimensions using Rigorous Coupled-Wave Analysis (RCWA).

The shallow angle HCGs in this section are optimized for small θ and ϕ , and are designed for 1550 nm. The refractive index of grating high index material is 3.6. The low index material is air, with $n=1$. For $\theta=3^\circ$ and $\phi=0^\circ$ TE polarized light, the HCG parameters are period (Λ) = 665 nm, thickness (t) = 410 nm, and duty cycle (η) = 46%. The reflectivity spectrum of this HCG structure is calculated using RCWA as shown in

Figure 2.13. A very broadband (~500 nm), high-reflectivity (>99.9%) reflector is obtained. Although this HCG is optimized for TE polarized light, we can also design the HCG with the proper dimensions for providing a broadband, high-reflectivity spectrum for TM polarized light.

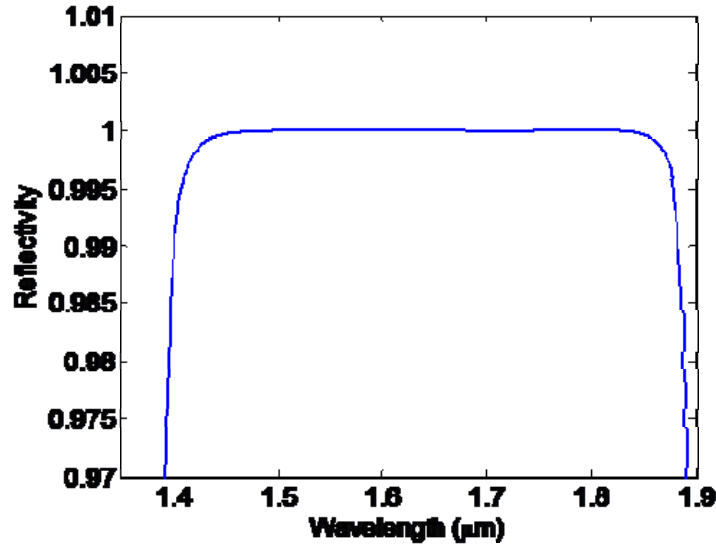


Figure 2.13 Calculated reflectivity spectrum of HCG with grating period (Λ) = 665 nm, thickness (t) = 410 nm, duty cycle (η) = 46%, for $\theta=3^\circ$ and $\varphi=0^\circ$ TE polarized light.

Reflectivity angular dependence study is performed for the same HCG structure at 1550 nm. Figure 2.14 shows the calculated reflectivity of HCG with 1550 nm TE polarized incident light when θ and φ are scanned. It shows that the shallow angle HCG design can achieve extremely high reflectivity (>99.99%) within a wide range of small θ and φ . However, when θ and φ increase, the reflectivity gradually drops. The HCG with such an angular dependence can be an ideal candidate for the side walls of a low loss hollow-core waveguide. In Chapter 6, we will discuss the shallow angle HCG and HCG-based ultra-low loss hollow-core waveguide in detail.

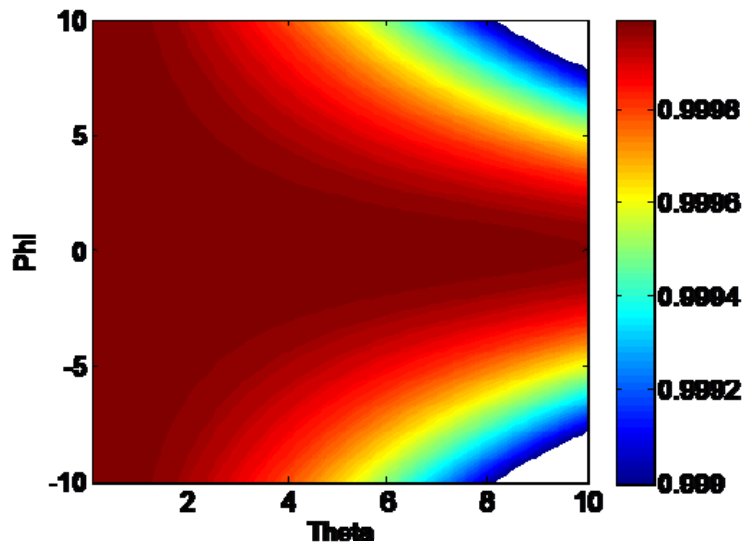


Figure 2.14 Calculated reflectivity of HCG with grating period (Λ) = 665 nm, thickness (t) =410 nm, duty cycle (η) =46%, for 1550 nm TE polarized light, when θ and ϕ are scanned.

2.5 Summary

We have presented a novel subwavelength high-contrast grating (HCG) structure that can offer different functionalities by changing the grating dimensions. First, we show that HCG can be optimized to provide a broadband reflection spectrum for both TM and TE polarized light under normal incident condition. Our dimension analysis shows that HCG can afford a large dimension variance while still maintaining high reflectivity. This is desirable for a low cost, high throughput manufacture process. We also show that the HCG structure can be easily scaled to a different wavelength window by simply multiplying the dimensions by a constant. Next, we show that HCG can be optimized as a surface normal narrow-band reflector or a high-Q optical resonator. This may have many interesting applications in lasers and filters, as well as optical sensors. Finally, we show that HCG can also serve as a broadband shallow angle reflector.

Chapter 3 HCG-based VCSEL

3.1 Introduction

Semiconductor diode lasers have a wide range of applications including high-speed optical communications, optical sensing, lasing printing, displays, and solid-state lighting. Among them, vertical-cavity surface-emitting lasers (VCSELs) [27-29] are particularly promising. Because they emit light normal to the wafer surface, it is possible to extract light more efficiently and to fabricate two-dimensional device arrays. VCSELs can offer many other advantages, including single wavelength emission, low cost manufacturing, wafer-scale fabrication and testing, and direct modulation over 10 GHz [30].

A typical VCSEL consists of a short active cavity sandwiched between two thick distributed Bragg reflector (DBR) mirrors for optical feedback. DBR is a structure formed from a stack of alternating high and low refractive index materials. Because of the short cavity length in a VCSEL, usually a very high reflectivity (>99.5%) is required

in order for the VCSEL to lase. However, because of epitaxial growth constraints for matching the material lattice constants, materials used in DBR structures often have small refractive index differences. Therefore, a large number of DBR pairs (usually 25-40 pairs) are required to achieve high reflectivity, leading to epitaxial challenges in many material systems. This problem is one of the main impediments in the development of VCSELs and other DBR-based optoelectronic devices in many wavelength regimes, such as blue-green and mid-infrared [31, 32]. In addition, during the material growth process the DBR layer thickness and composition must be very precisely controlled in order to achieve high reflectivity.

The broadband high-reflectivity subwavelength high-contrast grating we presented in the previous chapter can be an ideal candidate to replace DBR structure in VCSELs and other DBR-based optical devices. As we discussed in the previous chapter, HCG can achieve very high reflectivity with only a single layer of grating. It can easily achieve the reflectivity of a 5 μm thick DBR with 40 pairs of GaAs/AlGaAs layers, but with a much thinner thickness. For an $\text{Al}_{0.6}\text{Ga}_{0.4}\text{As}$ TM-HCG designed for 850 nm center wavelength, the mirror thickness is only 235 nm. For an $\text{Al}_{0.6}\text{Ga}_{0.4}\text{As}$ TE-HCG designed for 850 nm, the mirror thickness is even thinner at 140 nm. This is a 20-40 times reduction in the epitaxial growth thickness. Thus, by using HCGs to replace DBR structures, we can significantly simplify the epitaxial growth process and potentially develop low cost surface-emitting devices in blue-green and mid-infrared wavelength regions.

In this chapter, we present a novel HCG-based vertical-cavity surface-emitting laser (VCSEL) by using a single-layer high contrast grating (HCG) as its top reflector. We will show that HCG not only provides enough optical feedback to make the VCSEL lasing,

but also improves the VCSEL performance, in many areas such as: stable and controllable output polarization, suppression of higher order transverse modes, and an exceedingly large fabrication tolerance.

3.2 Design

Figure 3.1 shows the schematic of a typical HCG-based VCSEL. The device consists of a conventional semiconductor-based bottom n-DBR mirror, a λ -cavity layer, and an HCG-based top mirror. The λ -cavity contains three quantum wells as an active region. The top mirror consists of two parts: an M-pair p-doped DBR and a freely-suspended HCG. The M-pair p-DBR is mainly used for providing current injection into the active region while protecting the active region during the fabrication process. In our fabrication work, we showed M can be 2 or 4. While the p-DBR does increase the overall reflectivity of the top mirror, as we have shown in Chapter 2, the number of p-DBR pairs can be reduced or eliminated because a single-layer HCG is capable of providing sufficient reflectivity ($R > 99.9\%$) as the VCSEL top mirror. Electric current injection is conducted through the top metal contact via the p-doped HCG layer and through the bottom metal contact via the n-DBR. Current confinement of the VCSEL is achieved through the use of an aluminum oxide aperture, which is formed from the thermal oxidation of an $\text{Al}_{0.98}\text{Ga}_{0.02}\text{As}$ layer in the p-DBR section right above the cavity layer.

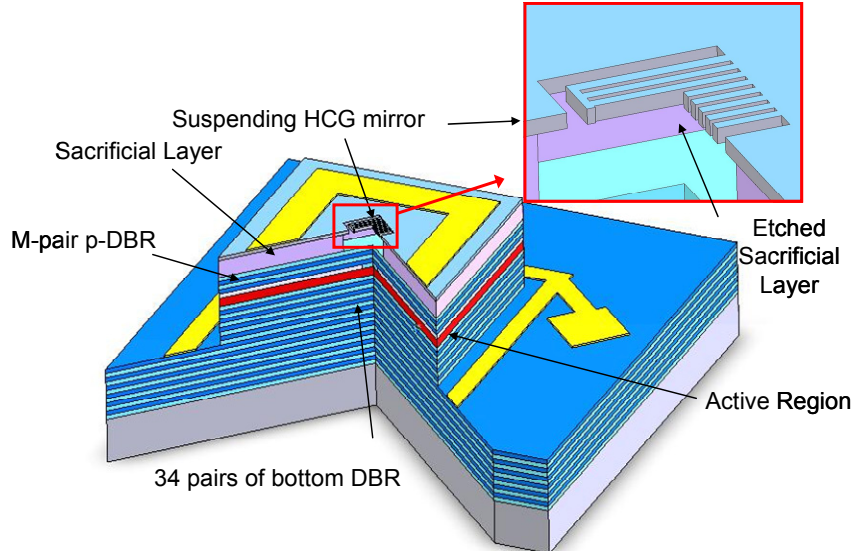


Figure 3.1 The cross-section schematic of HCG-based VCSEL. The top mirror consists of a freely-suspending HCG and M-pairs DBRs. $M=2$ or 4 .

The HCG structure used in the VCSEL top mirror can be either TM-HCG or TE-HCG. Both HCGs consist of periodic $\text{Al}_{0.6}\text{Ga}_{0.4}\text{As}$ stripes as the high index material with air as the low-index cladding layers on the top and bottom, as shown in the inset of Fig. 3.1. The dimensions of the HCGs are optimized for a wavelength of 850 nm. For TM-HCG, the grating parameters are: the period (Λ) = 380 nm, air spacing (a) = 130 nm and thickness (t) = 235 nm. For TE-HCG, the grating parameters are: the period (Λ) = 620 nm, air spacing (a) = 400 nm, and thickness (t) = 140 nm. The air gap distance between the HCG and M-pairs of DBR is designed to be 1.05 μm , which is $\sim 5\lambda/4$ for $\lambda=850$ nm. Grating sizes of these HCGs are typically $12 \mu\text{m} \times 12 \mu\text{m}$. The most critical lithography dimension for both TE- and TM- HCGs is the air spacing (a); for TM-HCG, it is ~ 130 nm, but for TE-HCG, it is as large as 400 nm. Therefore, in terms of lithograph dimension, TE-HCG is much easier to fabricate than TM-HCG.

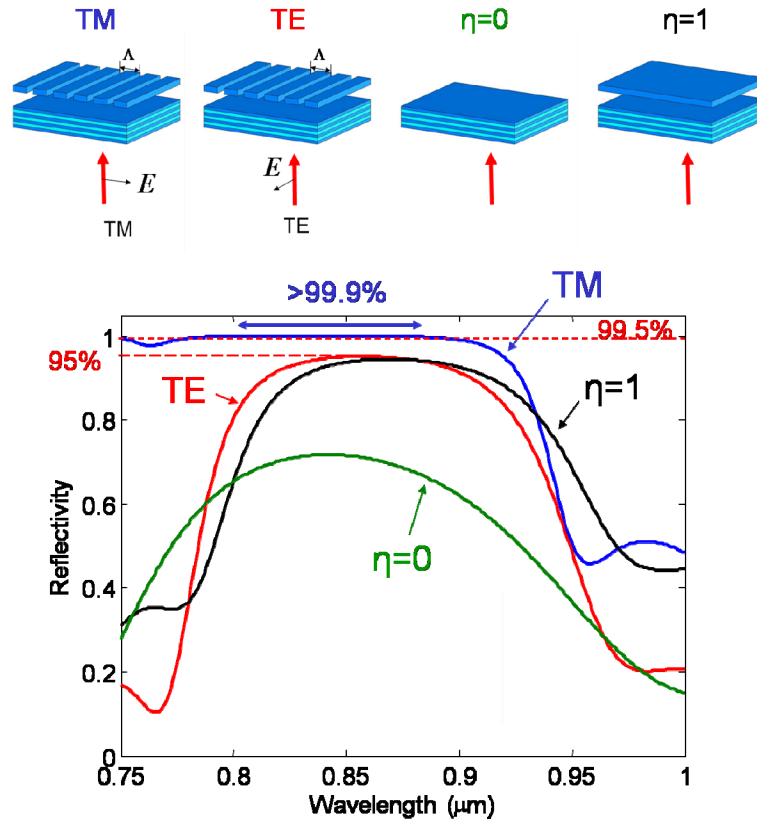


Figure 3.2 Calculated TM-HCG-based mirror reflectivity for TM and TE polarized light. The reflectivity is also calculated for a grating with 0% and 100% duty cycles (η). $\eta = 0$ corresponds to no HCG layer, while $\eta = 100$ means an additional uniform layer of AlGaAs is used to provide extra reflectivity.

The HCG-based top mirror is designed so that it only provides high reflectivity for one polarization. Here we look at a TM-HCG-based mirror, which a TM-HCG plus four pairs of DBR. Figure 3.2 shows the calculated reflectivity for the TM and TE polarized incident plane wave. In Figure 3.3, the reflectivity for the TM polarized light is $>99.9\%$ for wavelength ranges of $0.8\text{-}0.88\mu\text{m}$, whereas that for TE polarized light is around 95% at best. Since a reflectivity value of $>99.5\%$ is typically required for a VCSEL to lase, only TM polarization light will achieve lasing condition. As a comparison, the reflectivity spectrum is also calculated for gratings with duty cycle (η) of 0% and 100% . $\eta = 0$ corresponds to no HCG layer, while $\eta = 100$ means an additional uniform layer of

AlGaAs is used to provide extra reflectivity. In both cases, the calculated reflectivity is not high enough for VCSEL to achieve lasing.

3.3 Fabrication

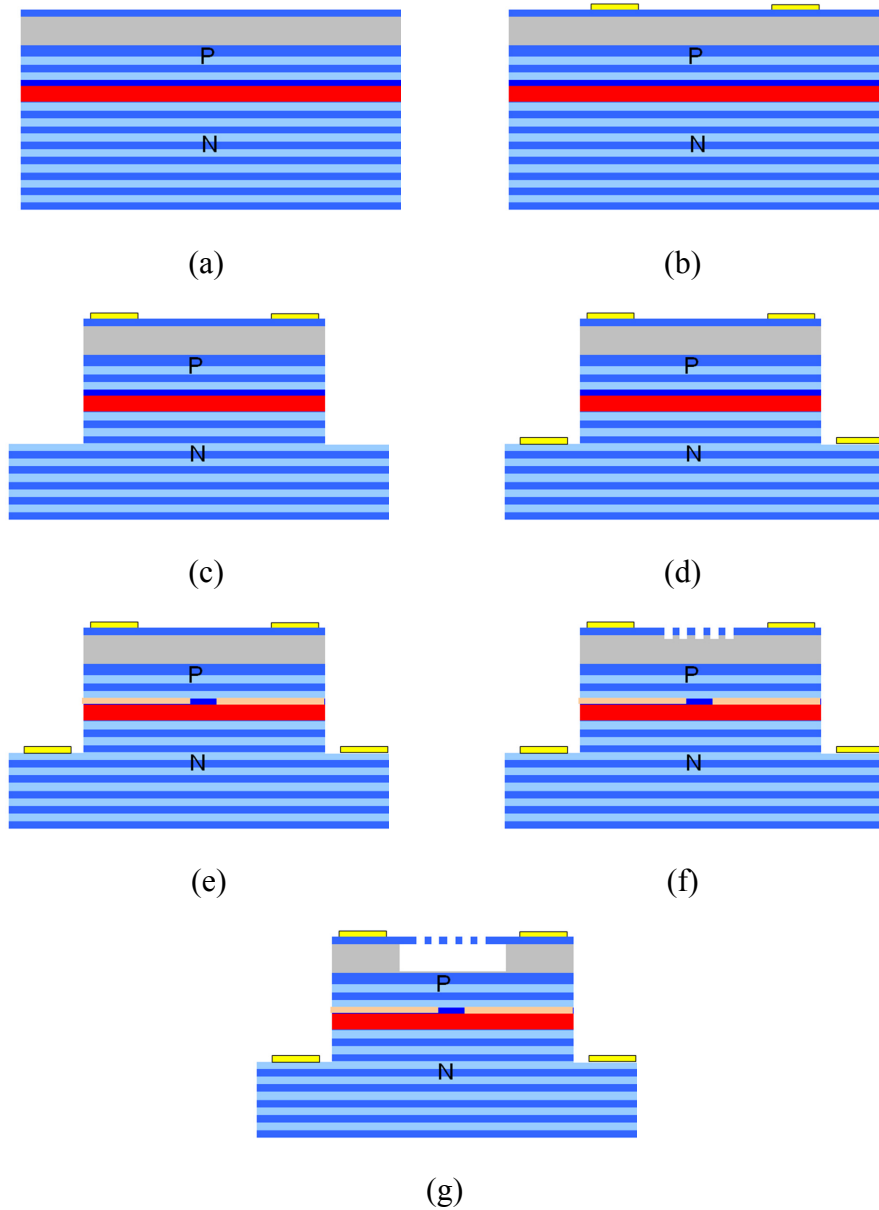


Figure 3.3 Fabrication process flow of a HCG-based VCSEL. (a) starting epitaxial wafer (b) top metal contact deposition (c) device mesa etch (d) bottom metal contact deposition (e) thermal oxidation (f) electron-beam lithography and reactive ion etching (RIE) (g) selective wet etching removing sacrificial layer and critical point drying. Step (a)-(e) are the same as a standard VCSEL process.

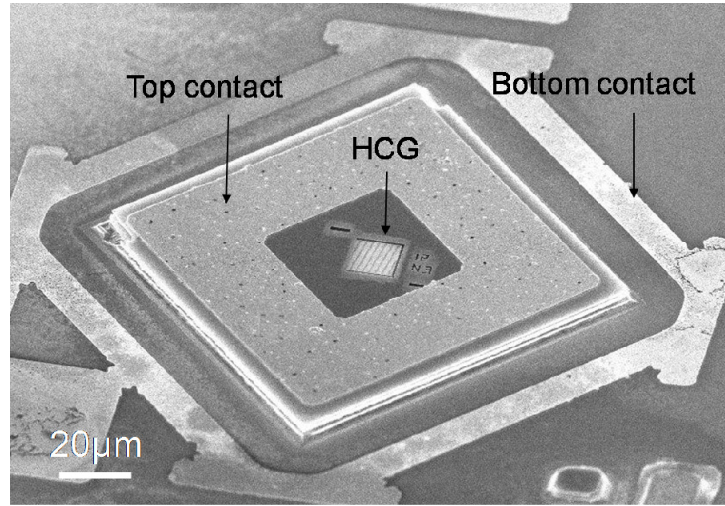
The fabrication process of the HCG-based VCSEL is similar to that of a standard VCSEL, including two metal depositions, mesa formation etch, thermal oxidation, and HCG definition. Figure 3.3 shows the fabrication process flow of a HCG-based VCSEL. The process starts with an epitaxial GaAs wafer grown by metal organic chemical vapor deposition (MOCVD) (Figure 3.3 (a)). The first step is the top metal contact deposition of Ti-Au alloy by electron beam evaporation on the p-doped HCG layer (Figure 3.2 (b)). After that, a wet chemical-based vertical etch is used to etch down to the bottom n-type DBR layers and form the VCSEL mesa structure (Figure 3.3 (c)). $\text{H}_2\text{SO}_4:\text{H}_2\text{O}_2:\text{H}_2\text{O}$ (1:8:40) wet etchant is used from this mesa etch. A Ni-Ge-Au alloy metal is then deposited to form the bottom contact on the n-DBR layers (Figure 3.3 (d)). Then the device goes through a thermal oxidation process at 450°C to form the aluminum oxide aperture for electrical and optical confinement (Figure 3.3 (e)). After this, the HCG is patterned by electron-beam lithography on poly-methyl methacrylate (PMMA) photoresist, which provides the design flexibility in terms of the grating period and duty cycle. The lithography patterns are then transferred through a reactive ion etching (RIE) process (Figure 3.3 (f)). Due to non-idealistic grating sidewall undercut from our particular etching process, the grating sometimes has a 20-30 nm undercut on each side of the grating side wall. Consequently, the required device critical lithography dimension may be 40-60 nm smaller than the nominal value obtained from the simulation. Finally, a selective etch process is carried out, followed immediately by a CO_2 critical point drying process, to remove the GaAs sacrificial material underneath the HCG layer and to form the freely suspending grating structure (Figure 3.3 (g)).

To accomplish this, a highly selective etch is required, and so for the release process, we developed a citric acid-based etching solution, which is of critical importance for the success of our device fabrication. The etching solution was prepared from 1:1 anhydrous citric acid: DI water (w/w). The citric acid was mixed with NH_4OH solution to adjust its pH to 6.5. Finally, the mixture of the pH-adjusted citric acid and H_2O_2 solution in a volume ratio of 5:1 was heated to 60°C . The heating drastically increases the diffusion of the etching solution and thus significantly shortens the etching time.

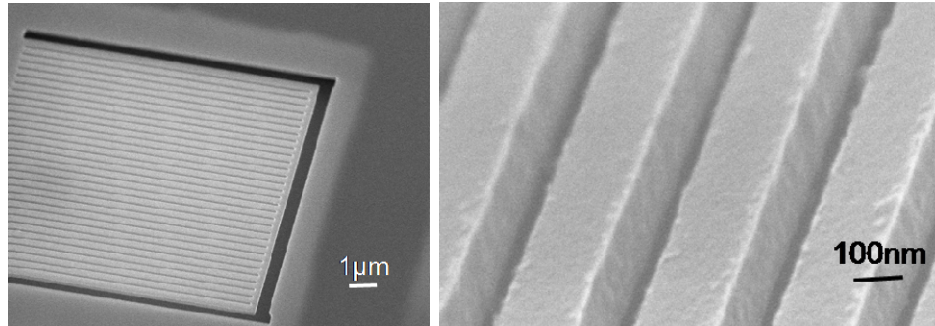
In the HCG-based VCSEL fabrication process, the HCG is defined after a standard VCSEL fabrication process (Figure 3.3 (a)-(e)); therefore, current VCSEL fabrication processes and facilities can be adapted to HCG-based VCSEL fabrication. The critical dimension of the HCG lithography is its air gap spacing. For TM-HCG, it is 140 nm and for TE-HCG, it is 400 nm. Although for research purposes we use electron-beam lithography in our process, because of its flexibility in patterning different grating dimensions, high-throughput fabrication processes such as deep UV lithography can also be implemented at these critical dimensions for large volume batch processing. As we will show later in this chapter, HCG is very robust to fabrication imperfection and has a large tolerance to dimension variations. Therefore, some low-cost, less accurate processes, such as nano-imprint technology, can also be used for HCG-based VCSEL fabrication.

Scanning electron microscope (SEM) images of the fabricated HCG-based VCSEL are shown in Figure 3.4. Figure 3.4 (a) shows the overview of a HCG-based VCSEL, with top contact, bottom contact, and HCG labeled in the figure. HCG is patterned in the center of the VCSEL mesa aligned with the oxide aperture. Figure 3.4 (b) is a close-up

SEM image of the freely-suspending HCG, where a stress-relief trench is used to eliminate buckling of the grating. Figure 3.4 (c) shows the zoomed-in SEM image of the fabricated individual grating stripes.



(a)



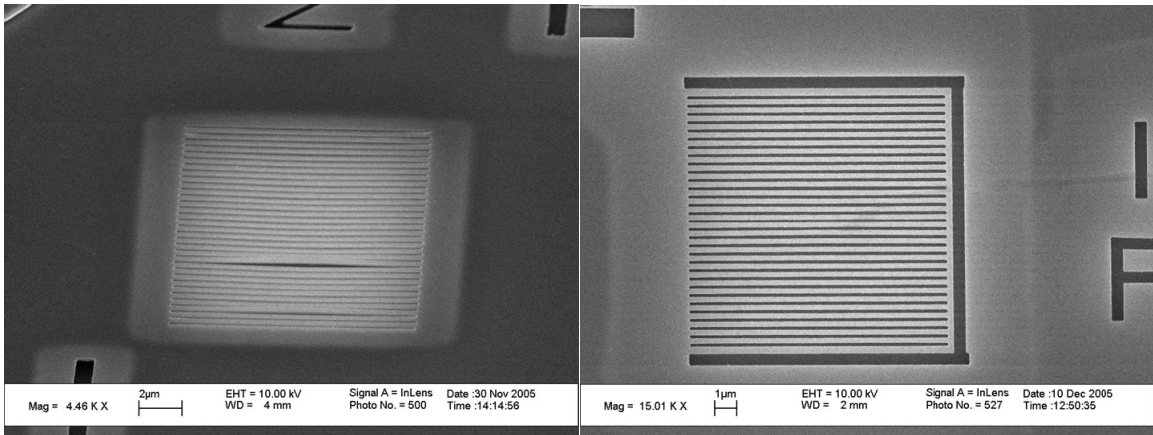
(b)

(c)

Figure 3.4 (a) SEM image of fabricated HCG-integrated VCSEL, where the grating is aligned to the center of the device mesa. (b) Close-up SEM image of the freely-suspending grating, where a stress-relief trench is used to eliminate buckling of the grating. (c) Zoomed-in SEM image of the fabricated individual grating stripes.

A novel C-shape stress-relief trench is developed to release the residual stress accumulated in the epitaxial growth process. Figure 3.5 (a) shows a HCG without the stress-relief trench. After the sacrificial layer underneath the grating layer is removed by

selective etching, some grating stripes buckle up due to the residual stress. Figure 3.5 (b) shows a HCG with a stress-relief trench after the sacrificial layer removal. The trench releases the residual stress on the material and completely solves the grating buckling issue.



(a)

(b)

Figure 3.5 (a) A HCG without the stress-relief trench. After sacrificial layer underneath the grating layer is removed, the some grating stripes buckle up due to the residual stress. (b) A HCG with a stress-relief trench after the sacrificial layer removal. The trench releases the residual stress in the material and the grating buckling issue is completely solved.

3.4 Optical Characteristics

Single mode, continuous-wave (CW) operation of HCG-based VCSELs, was demonstrated for both TM-HCG and TE-HCG at room temperature.

3.4.1 TM-HCG-based VCSEL

Figure 3.6(a) shows typical optical output power versus input current (LI) and voltage versus current (VI) characteristics for a TM-HCG-based VCSEL under room temperature. The device has a very low threshold current of 0.5 mA and an output power of ~ 1 mW. As a comparison, a conventional VCSEL grown by the same epitaxy wafer

vendor typically has a threshold current of 1 mA. Therefore, there is a 50% threshold current reduction from replacing the top DBR structure with a HCG-based mirror, which is due to the higher reflectivity provided by top HCG-based mirror. From the lasing operation of the HCG-based VCSEL, we experimentally demonstrated that HCG can provide a reflectivity larger than 99.5%.

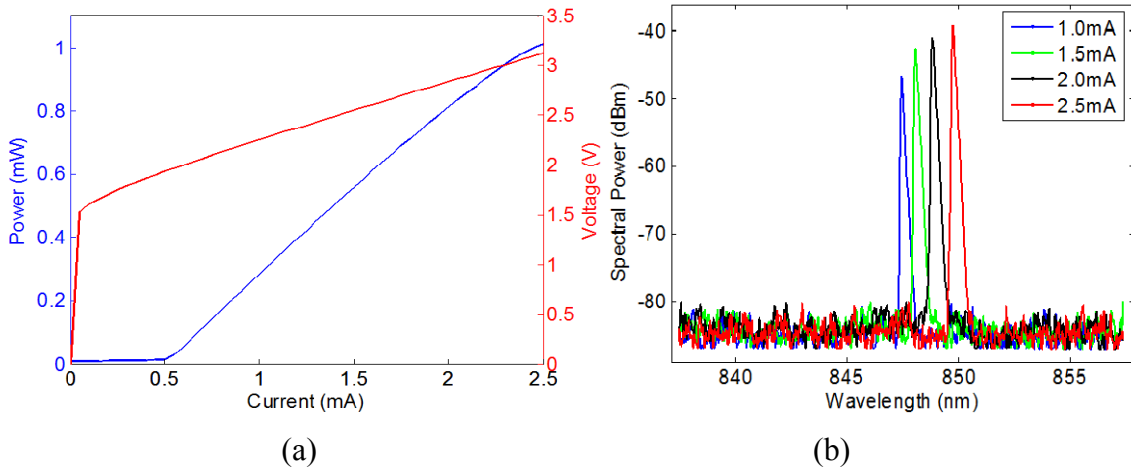


Figure 3.6 (a) Optical characteristic of typical optical TM-HCG-based VCSEL showing output power versus input current (LI) and voltage versus current (VI) under room temperature. The device has a very low threshold current of 0.5 mA and an output power of ~1 mW. (b) Measured single-mode emission spectra under different bias currents, showing a 40 dB suppression of higher-order transverse modes.

Figure 3.6 (b) shows the emission spectra of a TM-HCG-based VCSEL under various injected currents. Single mode emission with a >40 dB side mode suppression ratio (SMSR) was obtained. The high SMSR can be attributed to the optical confinement of aluminum oxide aperture and an angular dependence of HCG reflectivity. Due to the thermal heating effects, the emission spectrum of the device red-shifts when the biased current increases, due to the thermal heating effects.

3.4.2 TE-HCG-based VCSEL

The optical characteristics of TE-HCG-based VCSEL are shown in Figure 3.7. Figure 3.7(a) shows the optical output power versus input current (LI) and voltage versus current (VI) characteristics for a TE-HCG based VCSEL under room temperature. A threshold current of 1 mA and an output power of 2 mW are obtained. Figure 3.6 (b) shows the emission spectrum of this device at a bias current of 4 mA. Single mode emission with a >40 dB side mode suppression ratio (SMSR) was achieved.

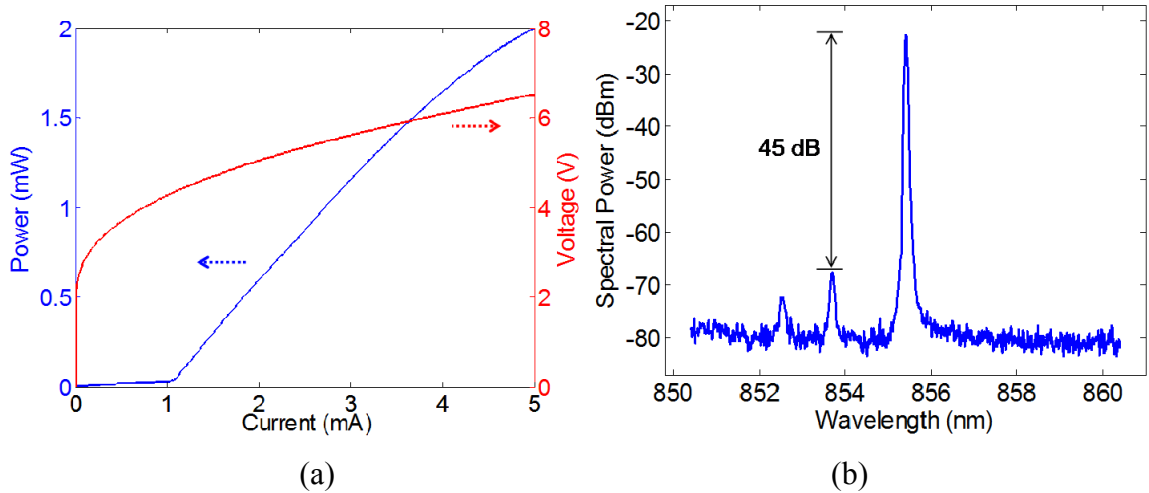


Figure 3.7 (a) Optical characteristic of typical optical TE-HCG-based VCSEL showing output power versus input current (LI) and voltage versus current (VI) under room temperature. The device has a low threshold current of 1 mA and an output power of ~ 2 mW. (b) Measured single-mode emission spectrum under a bias current of 4 mA, showing a 45 dB suppression of higher-order transverse modes.

3.4.3 Near Field Characteristics

Figure 3.8 shows the near field optical characteristics of the emission beam from a TM-HCG-based VCSEL. Despite the grating having a rectangular structure, the optical emission output remains a symmetrical, fundamental mode Gaussian profile. The beam

diameter is measured to be about $3\ \mu\text{m}$, which is characterized by the width of the 99% drop in intensity. The near field intensity distribution for a TE-HCG VCSEL is very similar.

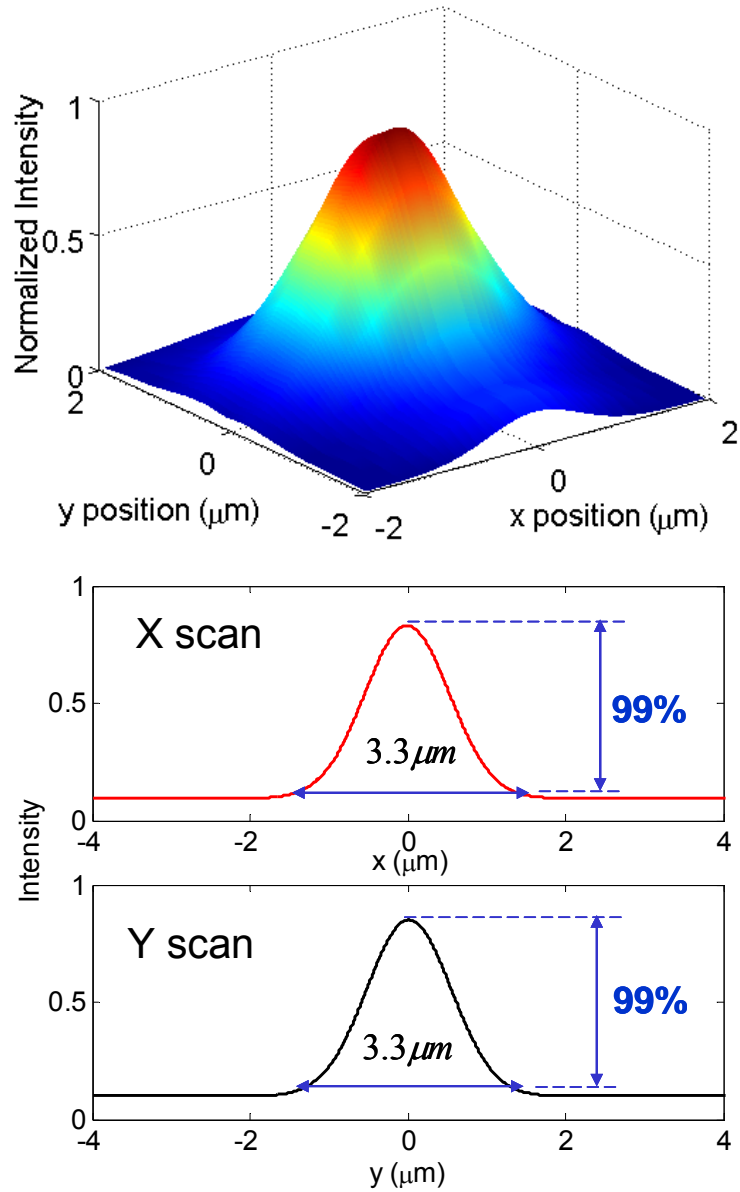


Figure 3.8 Measured optical near-field beam profile of the TM-HCG-based VCSEL with integrated HCG top mirror. The optical emission has a symmetrical, fundamental mode Gaussian beam profile.

3.5 Polarization Control

3.5.1 Introduction

In a conventional DBR-based VCSEL, it is hard to control the polarization of the output light due to the lack of pre-determined polarization control in distributed Bragg reflectors (DBRs). In a conventional VCSEL, polarization modes are degenerated transverse modes. Due to the lack of polarization selection, polarization mode hopping of a VCSEL can cause mode partition noise in an optical communication link [33]. The polarization state in VCSELs can be controlled by introducing anisotropy in the waveguide such that only one polarization state is supported, or by providing a polarization dependent gain or loss. For instance, by using anisotropic optical gain in (311)B substrate [34], or by using anisotropic optical loss by surface relief grating etched onto the top DBR [35-37], stable-polarization operation in VCSELs has been achieved.

In this section, we present highly effective and deterministic polarization mode control in HCG-based VCSEL under both CW and dynamic operation. We will use TM-HCG-based VCSEL as an example. However, similar results can also be obtained for TE-HCG-based VCSELs.

3.5.2 CW Polarization Control

Since the HCG design contains 1D symmetry, its optical property is polarization sensitive. In a TM-HCG-based VCSEL, TM polarized light with an electric field perpendicular to the grating stripes sees a much higher reflectivity than TE polarized light. As shown in Figure 3.2 in the design section, the calculated reflectivity for the TM polarized light is $>99.9\%$ for 830-880 nm wavelength ranges, while that for TE polarized light is merely $\leq 95\%$, thus making the HCG an excellent VCSEL top mirror for

polarization control. Compared to other VCSEL polarization control techniques, the inherent reflectivity difference between TM and TE polarized light in HCG results in a large polarization-dependant modal loss. The calculated threshold gain required for the TE polarization ($g_{th,TE}$) is approximately 4 times larger than that required for the TM polarization ($g_{th,TM} \approx 740 \text{ cm}^{-1}$).

Figure 3.9 shows a polarization-resolved light intensity-current (LI) measurement for a TM-HCG-based VCSEL, plotted in log scale. In this measurement, a Glen-Thompson polarizer with an extinction ratio of $\sim 40 \text{ dB}$ was used to differentiate TM and TE emission light. We see a distinctive polarization preference in the light emission of this HCG-based VCSEL. Only TM polarization mode can achieve lasing condition, and TE polarization mode remains in spontaneous emission within the current sweeping range. Above threshold, the TM polarized light has a power that is 22 dB higher than the power from TE polarized light.

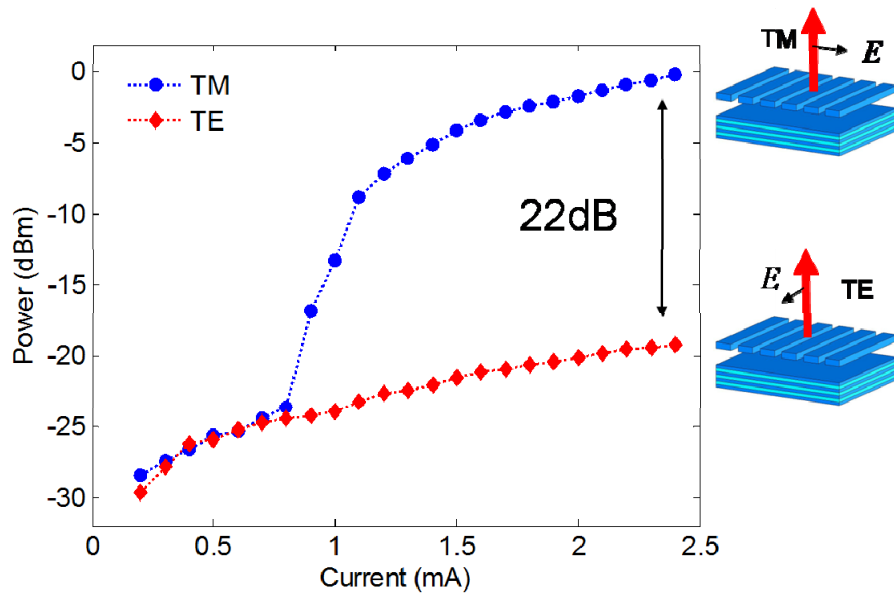


Figure 3.9 Measured polarization-resolved light intensity-current (LI) characteristics for a TM-HCG-based VCSEL.

From the polarization-resolved LI characteristics, it is evident that the power of TM emission light starts to differentiate from the power of TE polarized light when the laser reaches above the threshold condition. However, since the intensity measurement contains many spectral contents, a better way to identify and quantify the two orthogonal polarization modes is by spectral measurement. Figure 3.10 shows the polarization-resolved spectra when the polarizer is perpendicular (TM) or parallel (TE) to the grating stripes. It can be clearly seen that the TM polarized lasing peak is >30 dB higher than the TE peak. In other words, orthogonal polarization suppression ratio (OSPR) is >30 dB, which is higher than the 22 dB value measured from the polarization-resolved LI in Figure 3.9. This is due to the fact that the power of TE polarized light also contains a significant amount of power from spontaneous emission of the quantum well gain peak.

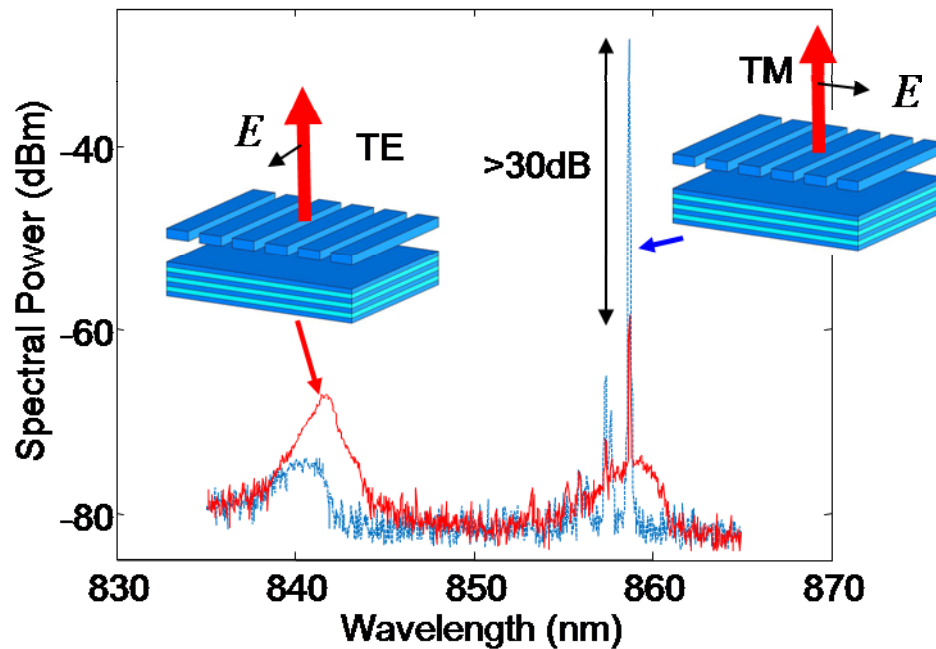


Figure 3.10 Measured polarization-resolved optical spectra for a HCG VCSEL, with the polarizer rotated to the two orthogonal angles with respect to the grating stripes.

3.5.3 Dynamic Polarization Control

We investigated the time-dependant OPSR under large-signal direct modulation to examine the difference in the polarization stability under CW and dynamic operation. This is perhaps the most stringent test criteria for polarization mode selection, where the laser is switched from being totally off to on. In this study, the laser was tested without a DC bias and is modulated with 5 V_{pp} rectangular pulses, with an electrical pulse width of 1 μs width and a repetition rate of 5 μs. Fig. 3.11 shows the measured polarization-resolved emission spectra of a TM-HCG-based VCSEL. A very large OPSR of 28 dB is maintained showing the effectiveness of HCG in polarization selection under dynamic modulation. Due to the large carrier transient and chirp as well as thermal heating effects under pulsed modulation, the measured spectrum was broadened in this case.

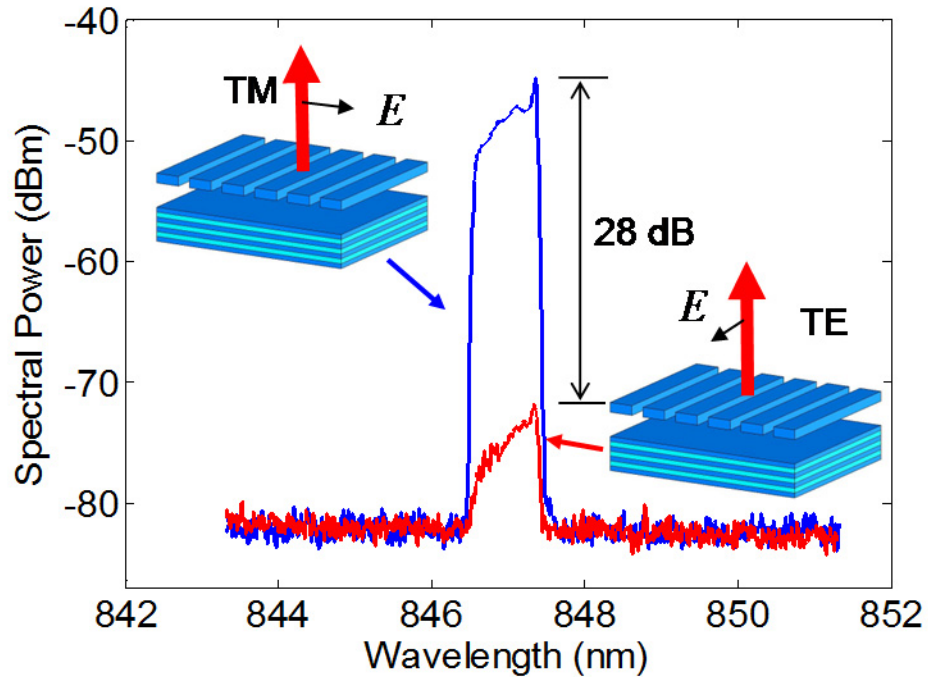


Figure 3.11 Measured polarization-resolved optical spectra for a TM-HCG-based VCSEL under a large-signal on-off modulation.

3.5.4 Lithographically Defined Polarization

To determine the feasibility of using lithography to deterministically control the emission polarization of VCSELs, we fabricated TM-HCG-based VCSELs on the same wafer with grating stripes oriented in various angles with respect to the [011] crystal axis direction at a step of 30 degrees, as shown in Figure 3.12. To ensure a fair comparison between the devices with different grating orientations, all device parameters were kept constant.

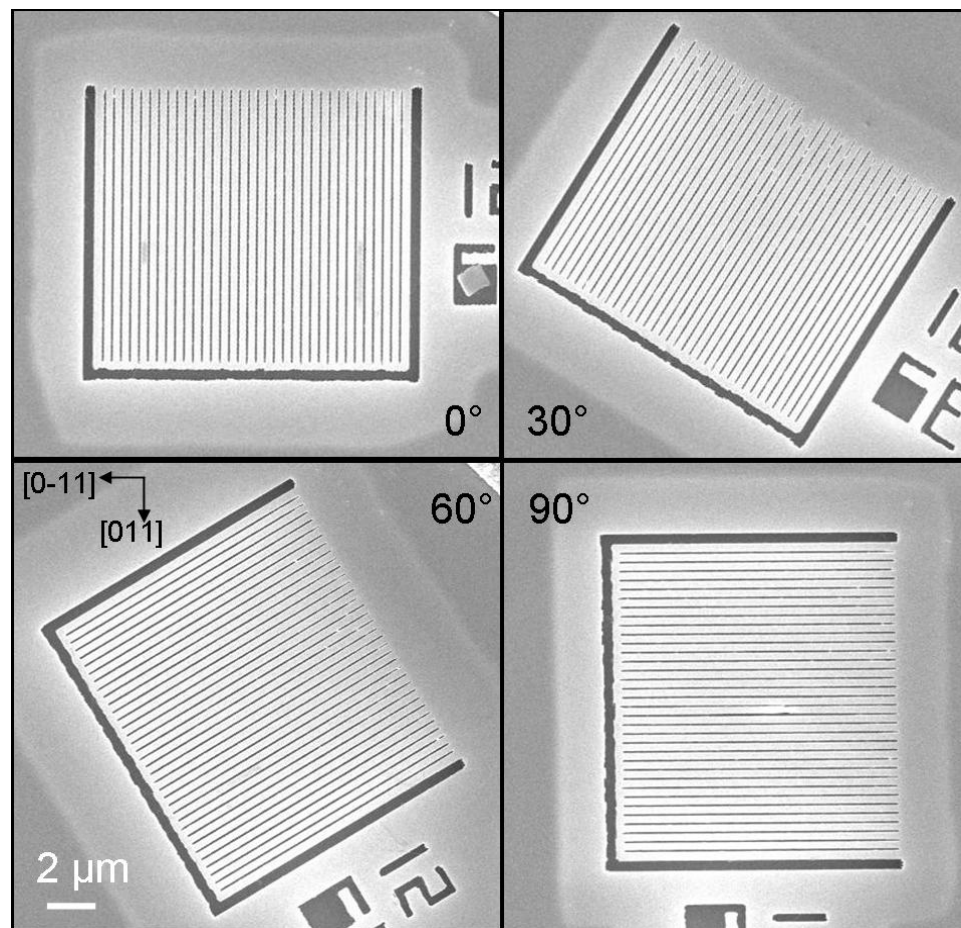


Figure 3.12 SEM image of the TM-HCG-based top mirrors, where gratings are patterned at different angles with respect to the [011] crystal axis.

We measured this set of VCSELs using polarization-resolved spectral measurement. For each device, we measured a set of spectra by rotating the output polarizer from parallel to [011] (0°) to perpendicular to [011] (90° or [0-11] direction). Figure 3.13 shows the measured polarization-resolved optical spectrum for a TM-HCG-based VCSEL with its grating defined at 0° with respect to [011], showing a set of family curves as the polarizer was rotated. The measured spectra peak intensity increased from 65 to 29 dBm as the polarizer is rotated from 0° to 90° . An orthogonal polarization suppression ratio of 36 dB is obtained.

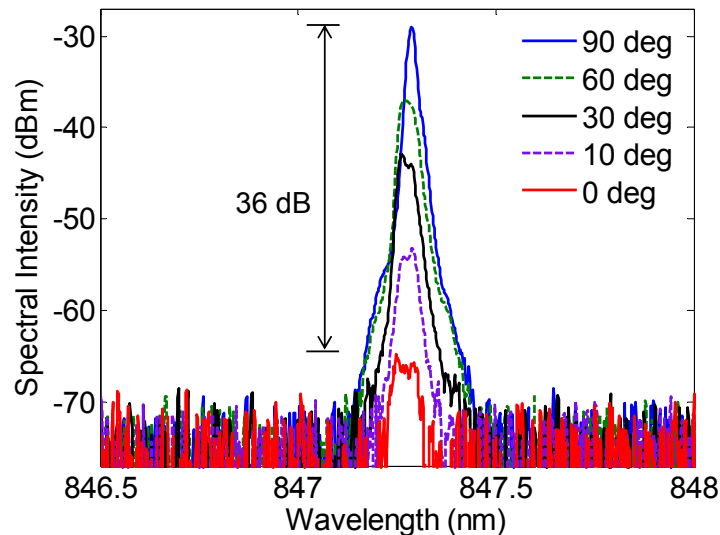


Figure 3.13 Measured polarization-resolved optical spectra of a HCG VCSEL, with the polarizer rotated to various angles with respect to the grating stripes.

We measured all the four devices with different HCG orientation using the same method. Figure 3.14 shows the measured spectral peak intensity as a function of the polarizer angle for the four TM-HCG-based VCSELs. The result illustrates that the maximal spectral intensity is always obtained when the polarizer is rotated perpendicular to the grating stripes, and the minimum when the polarizer is parallel. Furthermore, a

maximal orthogonal polarization suppression ratio of ~ 30 dB can be obtained when the HCG is patterned in the $[011]$ and $[0-11]$ direction.

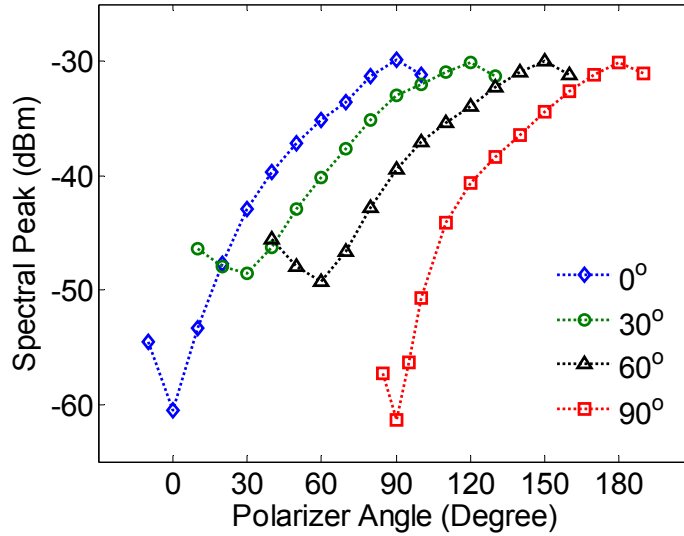


Figure 3.14 Measured spectral peak intensity as a function of the polarizer angle for four HCG-based VCSELs with their gratings patterned in different angles with respect to $[011]$ crystal axis.

From all these measurements, we clearly demonstrate that the output polarization of the HCG-based VCSEL can be lithographically determined with a mode discrimination as large as 25-36 dB.

3.6 Transverse Mode Control

3.6.1 Introduction

Single mode operation with a fundamental transverse mode is important for achieving high performance in optical communication systems [33]. A VCSEL operates with a single longitudinal mode by virtue of its extremely short cavity length. However, if the lateral diameter of the active region is large, multiple transverse mode operation typically occurs [33, 38]. When a VCSEL has a transverse dimension that is much larger

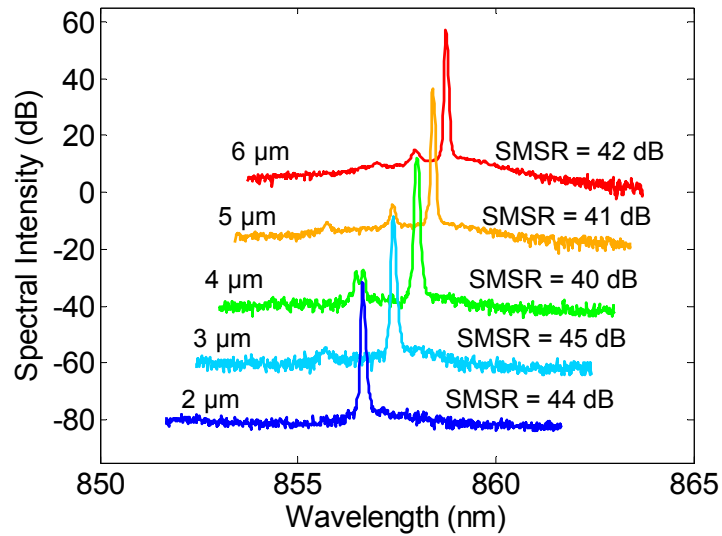
than its emission wavelength, several transverse modes can be supported and consequently the laser has the tendency to lase at multiple wavelengths. For an 850 nm VCSEL, single transverse mode operation requires an aperture size smaller than 2-3 μm . Thermal oxidation can be used to achieve a small aperture size [38]; however, the use of oxide aperture in VCSELs requires a tightly controlled oxidation process. In addition, due to the small aperture size, high power operation in the fundamental mode is difficult to achieve. In order to achieve single mode operation with high output power, extra loss structures can be introduced to increase the loss of higher order transverse mode inside a VCSEL and to suppress them from lasing. These structures include passive antiguide region [39], shallow surface relief [40], and photonic crystal defects [41]. While these methods have shown effectiveness in controlling the emission mode, they generally require additional structural complexity and stringent fabrication control.

The HCG reflectivity can be designed to vary with incident angle, which has shown to be effective in transverse mode control. A HCG-based mirror can suppress high order transverse modes and achieve single mode operation with a larger aperture size, hence providing higher output power. In this section, we will first present the oxide aperture size dependence study for HCG-based VCSELs, and show that we can achieve single mode operation with an oxide aperture size up to 10 μm . Then, we will show a HCG size dependence study on HCG-based VCSEL optical characteristics. We will also show the smallest TM-HCG and TE-HCG based mirrors which can still provide sufficient high reflectivity for VCSELs to lase.

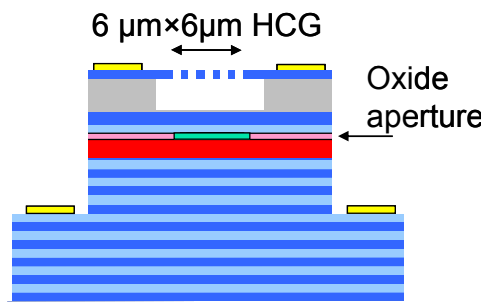
3.6.2 Oxide Aperture Dependence

First, let us look at a set of TM-HCG-based VCSELs with different oxide aperture sizes, but with a fixed finite HCG size. We fabricated a set of devices containing 16 individual TM-HCG-based VCSELs, each having a different mesa size from 100 to 115 μm . After the thermal oxidation process, VCSELs with a mesa size below 106 μm were completely oxidized, and the rest of the devices had different oxide aperture sizes ranging from 1 to 10 μm with a step of 1 μm . On each device, a fixed size of $6 \times 6 \mu\text{m}^2$ TM-HCG is patterned as the VCSEL top mirror. All the HCG parameters were kept constant in these devices for a fair comparison.

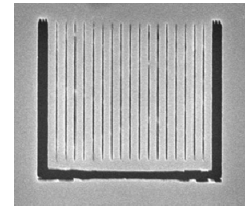
Figure 3.15 (a) shows the measured emission spectra for the fabricated HCG VCSELs with a grating size of $6 \times 6 \mu\text{m}^2$ and oxide aperture size ranging from 2 to 6 μm , while biased at 2 times the threshold current. All of these devices exhibit a single fundamental mode emission with a large SMSR ranging from 40 to 45dB. The schematic of devices are shown in Figure 3.15 (b) and the SEM image of the $6 \times 6 \mu\text{m}^2$ TM-HCG top mirror is shown in Figure 3.15 (c). Standard oxide-confined VCSELs with both top and bottom DBR mirrors from the same epitaxy manufacturer were fabricated as a comparison. Instead of using HCG-based mirrors in these devices, 24 pairs of DBR were used as the top mirror. For such device structures, the VCSEL maintains single mode operation only when the oxide aperture size is 1-2 μm . For a device with 3 μm oxide aperture, it will reach the multimode condition. A finite size HCG can differentiate against higher order modes well because they have higher angular components in the electric field, whereas a finite-sized HCG does not have high reflectivity.



(a)



(b)



**6 μm x 6 μm
(16 periods)**

(c)

Figure 3.15 (a) Measured optical emission spectra of TM-HCG VCSELs with $6 \times 6 \mu\text{m}^2$ grating top mirror and different oxide aperture sizes. All devices exhibit single fundamental mode emission with a SMSR between 40~45 dB. (b) Schematic of HCG-based VCSEL in this study. (c) SEM image of the $6 \times 6 \mu\text{m}^2$ TM-HCG.

We also observed that, in general, HCG-based VCSELs with an extremely small, $1 \mu\text{m}$ oxide aperture could not reach lasing operation, due to thermal heating and insufficient reflectivity from the HCG that resulted from a larger divergence angle, regardless of the size of the grating area. On the other hand, lasing operation also could not be obtained for the fabricated devices with an oxide aperture $>6 \mu\text{m}$, due to the insufficient reflectivity from the finite area of HCG. A general rule-of-thumb from our

experimental observation is that in order to ensure the sufficiently high reflectivity required for lasing, the HCG area needs to be at least as large as the oxide aperture of the VCSEL.

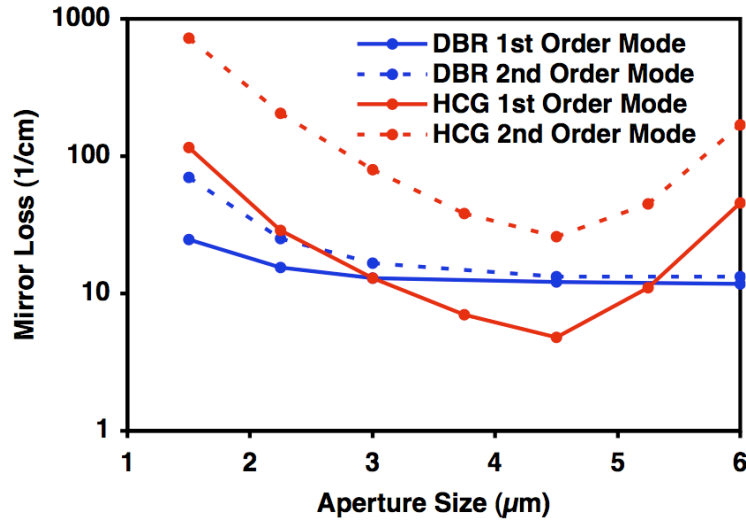


Figure 3.16 Finite difference time-domain (FDTD) simulation of mirror loss for 1st (solid) and 2nd (dotted) order modes of a 6 μm (9 period) TE-HCG and standard top DBR (24 pairs). The 2nd order mode sees high mirror loss and will not lase in HCG case, but will lase in apertures larger than ~ 3 μm in a standard VCSEL structure.

Numerical simulation is performed to study the oxide aperture size dependence on the HCG-based VCSELs performance, and the simulation results are very consistent with the experimental observation. Figure 3.16 shows a finite difference time-domain (FDTD) simulation of the transmitted mirror losses for the first and second order transverse modes in a standard top DBR with 24 pairs and a 6 μm size (9 periods) TE-HCG based mirror. The red lines show the mirror losses of the fundamental (solid) and the second order (dotted) mode for a 6 μm TE-HCG-based mirror. When the aperture size increases, the mirror loss curve first goes down, then up, and can be explained by the following: the HCG is designed in such a way that it provides higher reflectivity for surface normal

incident light than for incident lights, which deviate from the surface normal direction. For a specific mode, when aperture size is large, the divergence angle is small; a small divergence angle will experience a higher reflectivity from HCG. Therefore, the mirror loss decreases when the aperture size increases at the beginning. However, when the aperture size approaches the HCG size, due to the spreading of the light, the light close to (or outside) the edge of the HCG will experience a lower reflectivity (or little reflectivity). Therefore, when the aperture size approaches the HCG mirror size, the mirror loss of the HCG starts to increase again. For the same size oxide aperture, higher order transverse mode usually has a larger divergence angle (or larger transverse k vector). Therefore, in Figure 5.16, the mirror loss of the second order mode for the HCG-based mirror is always higher than the mirror loss of the fundamental mode. In fact, for a $6\ \mu\text{m}$ HCG-based mirror, the mirror loss of the second order mode is so high that it never reaches the lasing condition. This explains why HCG-based VCSEL can maintain single mode operation even when the oxide aperture size is relatively large.

As a comparison, in Figure 5.16, the mirror losses of a 22 pairs of DBR structures are plotted in blue lines. Because the DBR structure has a much weaker angular dependence for reflectivity compared to a HCG-based mirror, the mirror losses for fundamental mode and 2nd order mode are very close to each other in DBR. When the aperture size is larger than $2\ \mu\text{m}$, both fundamental and 2nd order mode will reach lasing condition. Hence, the device will lase in multimode.

Figure 3.17 shows measured emission spectra of a TE-HCG-based VCSEL with $5.5\ \mu\text{m}$ HCG size and DBR-based VCSEL, both with similar aperture size ($\sim 5\ \mu\text{m}$). DBR-based device is highly multimode while HCG-based device is single mode. This clearly

shows that a finite size HCG can differentiate against higher order modes, allowing for larger aperture single mode devices than is possible with a device with a conventional DBR top mirror.

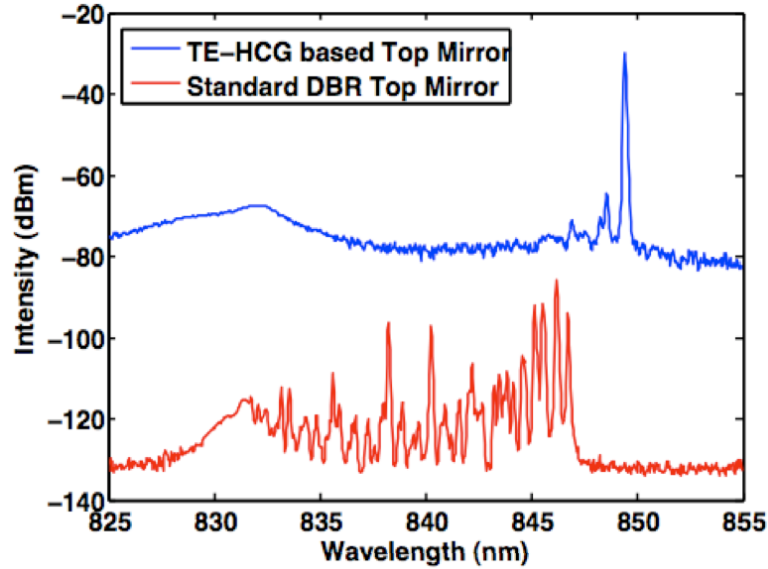


Figure 3.17 Measured emission spectra of TE-HCG-based VCSEL with 5.5 μm HCG size and DBR-based VCSEL with similar aperture size ($\sim 5 \mu\text{m}$). DBR-based device is highly multimode while HCG-based device is single mode.

3.6.3 Large Aperture Single Mode Device

In order to achieve a large aperture single mode HCG-based VCSEL, a set of VCSELs with different aperture size and with a larger grating area of $12 \times 12 \mu\text{m}^2$ were fabricated. Similar to the set of devices in the previous section, the oxide aperture sizes range from 1-10 μm . Figure 3.18 shows the measured emission spectra for the fabricated $12 \times 12 \mu\text{m}^2$ HCG-based VCSELs with oxide aperture size ranging from 2 to 10 μm , while biased at 2 times the threshold current. Similarly, devices with oxide aperture between 2 to 6 μm lase with single fundamental mode emission and with a large side mode suppression ratio of 35-42 dB. Since the grating area is larger, devices with oxide

aperture of 7-9 μm would still lase, but their optical emission shifts into the multimode regime. Interestingly, for the devices with the largest oxide aperture of 10 μm , the laser would again emit with a single mode output.

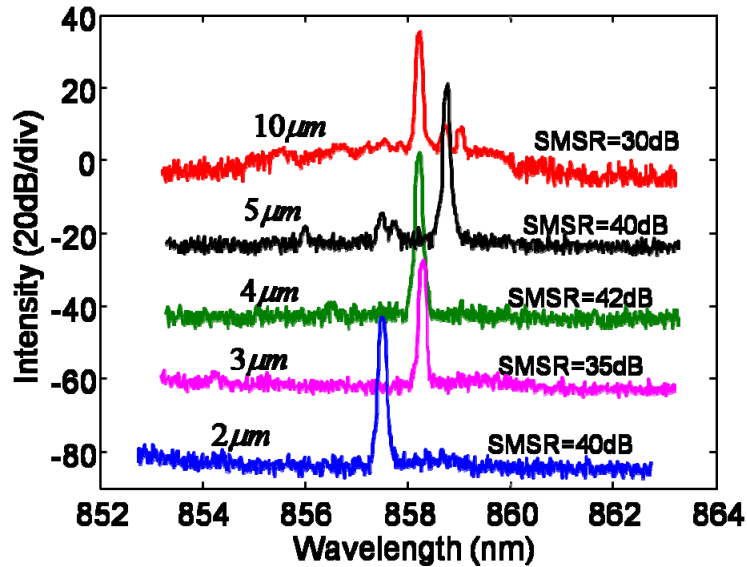


Figure 3.18 Measured optical emission spectra of TM-HCG VCSELs with $12 \times 12 \mu\text{m}^2$ grating top mirror and different oxide aperture sizes. A 10 μm aperture single mode HCG-based VCSEL is obtained.

Figure 3.19 (a) shows the measured LI characteristic for a HCG VCSEL with $12 \times 12 \mu\text{m}^2$ grating area and a 10 μm oxide aperture. Although the device exhibits a relatively large threshold current of 4 mA, it lases up to 10mA of injected current bias and outputs a maximum power of ~ 2.5 mW. Figure 3.19(b) shows the measured emission spectra of this device biased at $1.2I_{\text{th}}$, $1.5I_{\text{th}}$, and $1.8I_{\text{th}}$. The laser maintains a stable, single transverse mode emission with a SMSR of 30dB. However, the device lases at a higher order transverse mode instead of the fundamental mode. This is because of current crowding effect at the inner edges of the oxide current constrictions, which leads to the preferential gain, and thus to the excitation of the higher-order transverse modes.

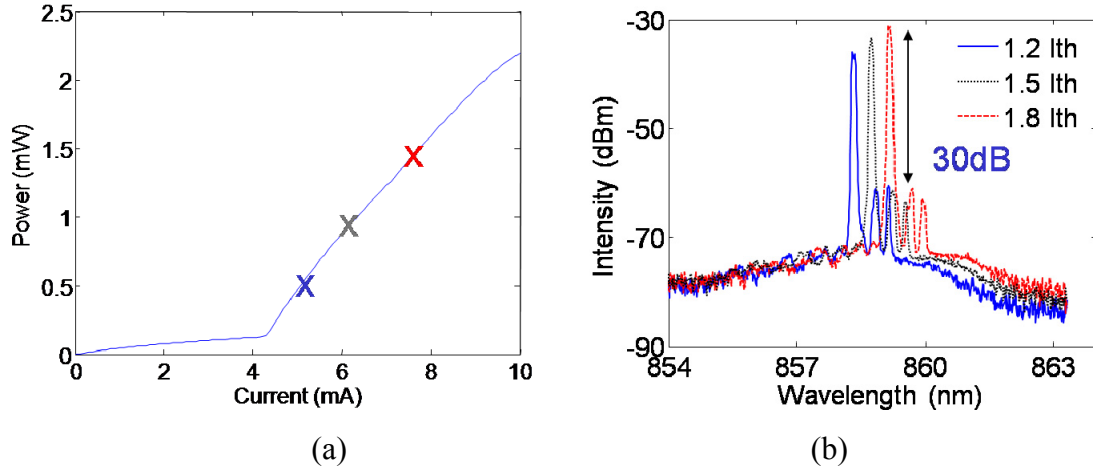


Figure 3.19 (a) The measured light intensity as a function of the injected current for a VCSEL with a $12 \times 12 \mu\text{m}^2$ HCG top mirror. (b) the emission septum for each device when biased at $1.2I_{th}$, $1.5I_{th}$, and $1.8I_{th}$. The HCG VCSEL operates in single mode (30 dB SMSR) despite having the large $10 \mu\text{m}$ oxide aperture.

3.6.4 HCG Size Dependence

To study the HCG size dependence and to experimentally determine the smallest HCG size required to achieve lasing condition, we fabricated a set of TM-HCG-based VCSELs with a variation in the HCG size from 2×2 to $12 \times 12 \mu\text{m}^2$ with a step of $2 \mu\text{m}$, while keeping all other parameters constant (i.e. grating dimensions, VCSEL geometries and oxide aperture size). All the devices have the same oxide aperture size of $2 \mu\text{m}$. For TM-HCG-based VCSELs, all the devices with a grating area larger than $4 \times 4 \mu\text{m}^2$ operate in the CW lasing condition with single mode optical emission. Among these devices, we observed that the smallest HCG required for a VCSEL to achieve lasing operation is $4 \times 4 \mu\text{m}^2$. Figure 3.20 shows the scanning electron microscope image of such TM-HCG-based VCSEL with an ultra compact HCG top mirror, where a very compact and freely suspended $4 \times 4 \mu\text{m}^2$ HCG is located in the center of the VCSEL mesa. On the contrary, lasing operation could not be obtained for the fabricated HCG VCSELs with a grating

area less than $4 \times 4 \mu\text{m}^2$, attributed to insufficient reflectivity originated from abrupt ending at the edge of the HCG and the $\sim 1 \mu\text{m}$ alignment inaccuracy.

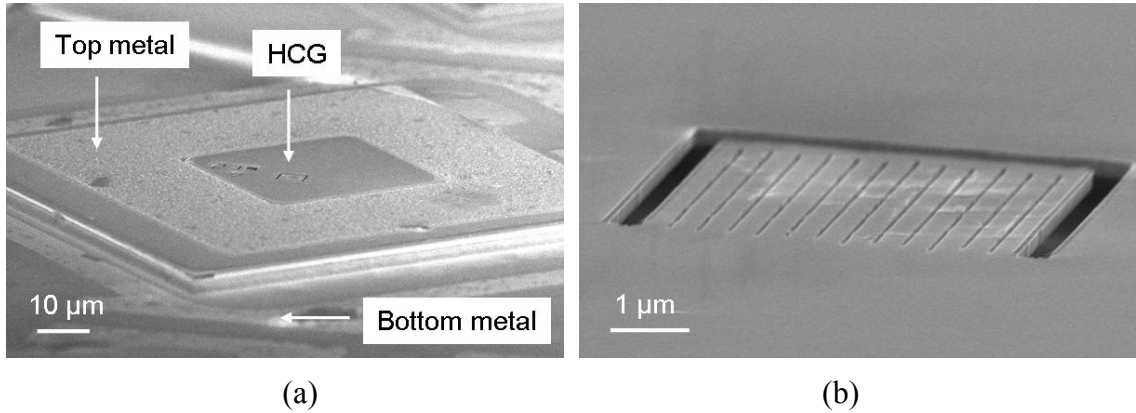


Figure 3.20 (a) SEM images of an ultra compact TM-HCG-based VCSEL utilizing a $4 \times 4 \mu\text{m}^2$ TM-HCG as the top mirror. (b) SEM image of the freely suspended TM-HCG, which consists of merely 11 $\text{Al}_{0.6}\text{Ga}_{0.4}\text{As}$ grating stripes with a thickness of 230 nm.

Similarly, a set of TE-HCG-based VCSELs were also fabricated with a variation in the HCG area from 2×2 to $8 \times 8 \mu\text{m}^2$ with a step of 620 nm (period of the TE-HCG). For TE-HCG-based VCSELs, we obtained single mode CW lasing operation for all the devices with a grating area larger than $3 \times 3 \mu\text{m}^2$. We obtained devices lasing with HCG as few as 4 periods or a size of $3 \mu\text{m} \times 3 \mu\text{m} \times 145 \text{ nm}$, with a mass of just 5 picograms! This means only 4 periods of TE-HCG can already provide reflectivity as high as 99.5%. Figure 3.21 shows an SEM image of the smallest working HCG-based VCSEL. The reduced HCG size limit can be attributed to the better alignment accuracy between the HCG and oxide aperture during this specific TE-HCG fabrication.

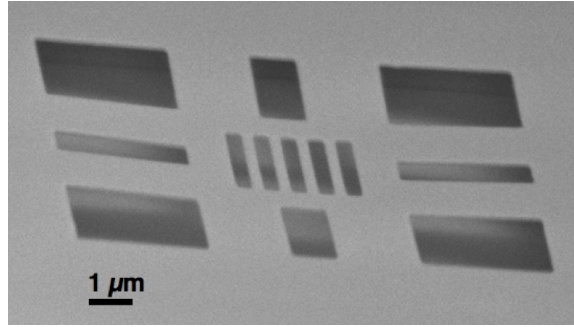


Figure 3.21 SEM image of the freely suspended TE-HCG with only 4 periods or a size of $3\ \mu\text{m} \times 3\ \mu\text{m}$.

Figure 3.22 (a) and (b) show a series of SEM images of TM- and TE-HCG top mirror with different sizes. VCSELs with all these HCGs achieved single mode lasing condition.

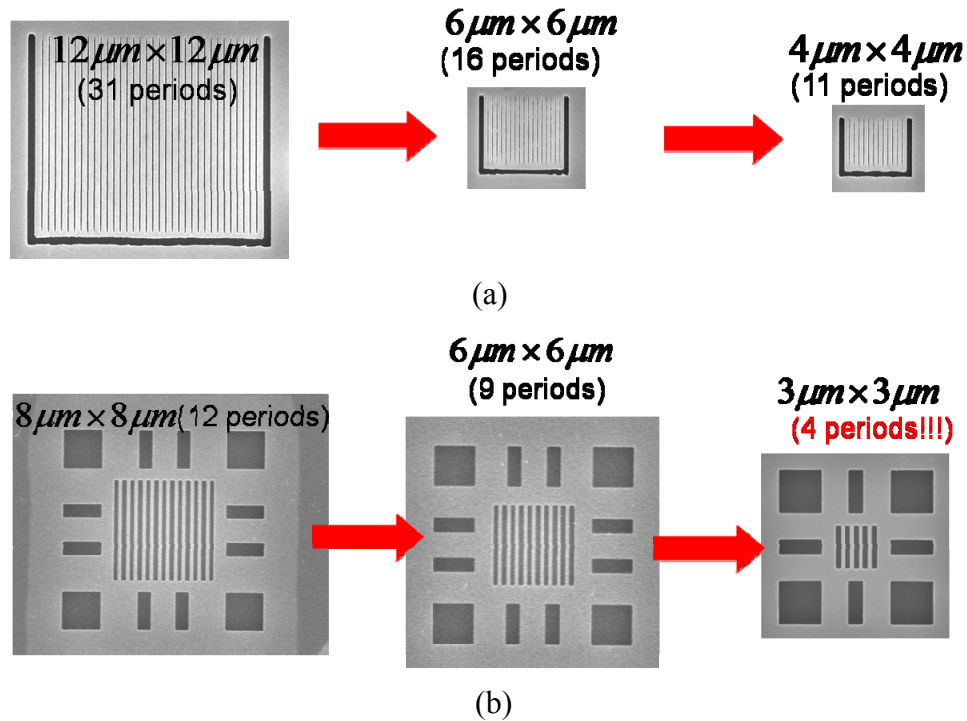


Figure 3.22 SEM images of the fabricated (a) TM-HCG and (b) TE-HCG mirrors on VCSELs, each with a different grating area as shown. VCSELs with all these HCGs achieved single mode lasing condition.

Light intensity-Current (LI) characteristics are measured for the lasing TE-HCG-based VCSELs with different grating sizes. All the devices have a 2 μm oxide aperture. . Figure 3.23 shows the LI curves of devices with different numbers of periods of TE-HCG. Device performance is fairly uniform for the devices with larger TE-HCGs. Threshold is stable at about 1 mA. Once the number of periods becomes less than 7, or the size of the HCG reaches 5 μm , the measured laser threshold current exhibits an inverse relationship to the grating area. The device threshold increases and slope efficiency decreases as the number of periods is further reduced.

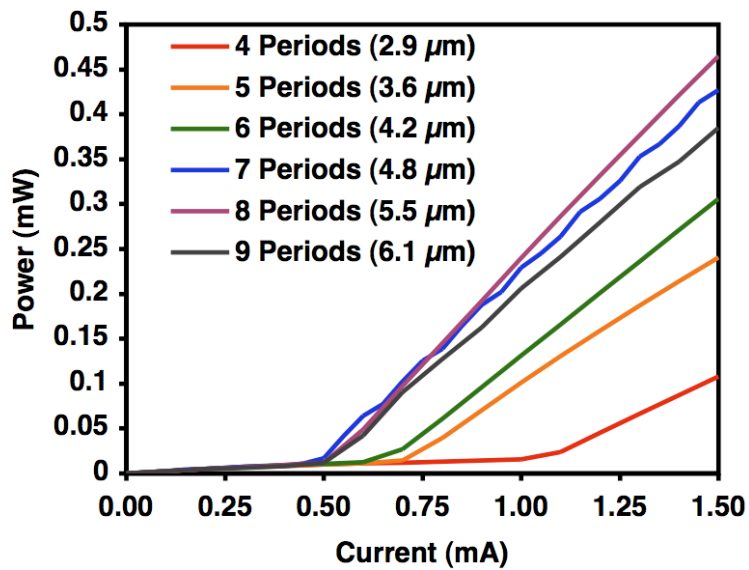


Figure 3.23 Optical characteristics for HCG VCSELs, showing the light intensity versus injected current for the set of identical TE-HCG VCSELs with different grating sizes and 2 μm oxide apertures.

Finite difference time domain (FDTD) simulation is performed to estimate the loss in reflectivity when the HCG size is reduced. Figure 3.24 shows the FDTD simulation of the mirror loss of the TE-HCG-based top mirror structure as the number of HCG periods is

reduced, as seen by a Gaussian beam of 2.5 and 3 μm diameter. The simulation shows the reflectivity to be relatively constant until the number of periods is reduced to less than 7 (4.8 μm). This indicates that although the physical mechanism responsible for the HCG structure's high reflectivity relies on periodicity, only a few periods are needed to obtain an extremely high ($> 99.5\%$) reflectivity. Also, the mirror loss is seen to increase at slightly larger apertures in the 3 μm beam case than in the 2.5 μm beam case. In both cases, once the HCG size is much larger than the aperture, the mirror loss will drop to a saturated low level and there will be almost no difference in threshold for different HCG sizes. This result agrees very well with the experimental observation in Figure 2.23.

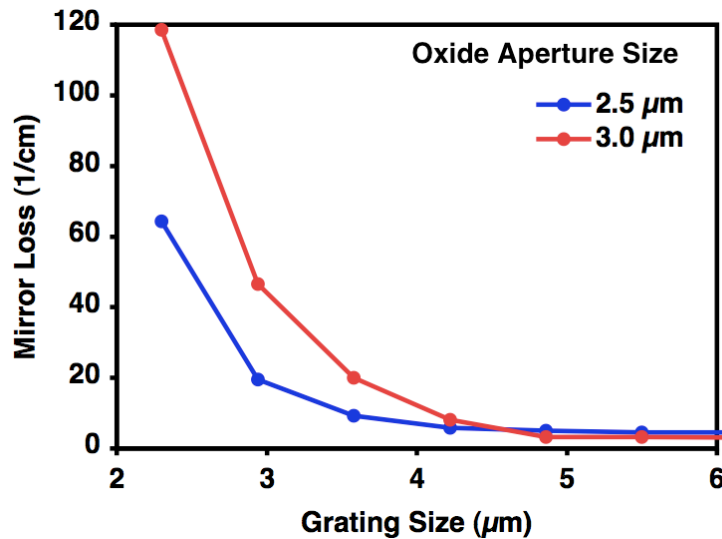


Figure 3.24 FDTD simulation of mirror loss for TE-HCGs at different finite grating sizes with two sizes of oxide apertures 2.5 μm and 3.0 μm . The HCG mirror loss is nearly constant until it has less than 4.8 μm (7 periods), indicating that the HCG does not require many periods to achieve high reflectivity.

3.7 Large Fabrication Tolerance

3.7.1 Introduction

A HCG-based VCSEL fabrication process includes a standard VCSEL fabrication process, followed by a HCG fabrication process. In order to achieve low-cost manufacturing, it is desirable to have a large fabrication tolerance for HCG dimensions. In this section, we will present both simulation and experimental demonstration of the large fabrication tolerance for HCG-based VCSELs, in particular the effects of lithographical variations. We will present the experimental study on gratings with uniform dimensions, as well as gratings with non-uniform geometries within the grating. We will also look at the lithography alignment tolerance for HCG-based VCSELs. We show that HCG can afford a very large fabrication tolerance and that low-cost, high-throughput fabrication processes, such as nano-imprinting [42], can be implemented for large volume batch processing.

In a HCG-based VCSEL, the grating thickness can be easily controlled by MOCVD or MBE epitaxial growth by maintaining accuracy in the order of nanometers. The grating period and duty cycle are determined by electron-beam lithography and reactive ion etching, which require some process calibrations in order to achieve the designed parameters. Among all the parameters, the most important one in the fabrication process is the grating air spacing. For TM-HCG, it is only ~ 100 nm, and for TE-HCG, it is ~ 400 nm. In this section, we will use TM-HCG-based VCSEL as an example with which to study the HCG fabrication tolerance.

3.7.2 Simulation and Experiment

In section 2.2.2, we studied the HCG dimension sensitivity of individual grating parameters based on rigorous coupled wave analysis (RCWA). However, as we just discussed, only grating period (A) and grating air spacing (a) are lithographically defined, and they are more likely to be affected by fabrication imperfection. In this section, we will mainly look at these two parameters. The contour plot in Fig. 3.25 shows the calculated fabrication tolerance window for a fixed wavelength of $0.84\ \mu\text{m}$, where both the grating period and grating spacing are varied. We can see the grating spacing (a), the critical dimension (CD) in HCG, has about $\pm 30\%$ fabrication tolerance while still maintaining a reflectivity of $>99.5\%$.

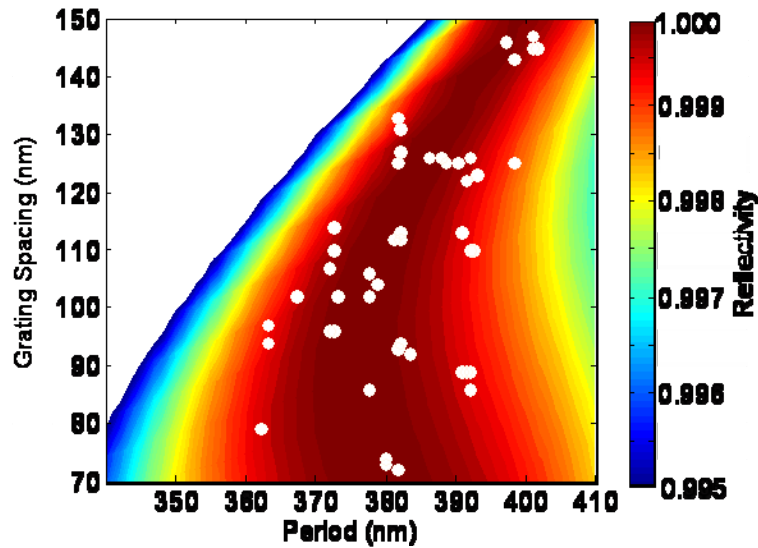


Figure 3.25 Simulated top mirror reflectivity as a function of grating spacing and period for fixed $\lambda = 840\ \text{nm}$. The white dots represent the combination of grating spacings and periods of the lasing TM-HCG-based VCSELs.

Experimentally, a large number of TM-HCG-based VCSELs with different combinations of grating spacing and period were patterned by using electron-beam

lithography. In Figure 3.25, the white dots represent the grating spacings and periods of a large ensemble of lasing, TM-HCG-based VCSELs measured by SEM. We demonstrated that TM-HCG structure can tolerate grating spacing variation from 80 nm to 120 nm ($\pm 20\%$ of CD of 100 nm), and a 40 nm change in grating period ($\sim 10\%$ of the design period of 380 nm), while still maintaining the VCSELs lasing. The thresholds of these VCSELs range from 0.3 mA to 1.8 mA, with oxide apertures ranging from 2 μm to 4 μm .

3.7.3 Dimension Tolerance for Uniform Gratings

HCG dimension sensitivity for both grating air spacing and grating period is experimentally studied. Figure 3.26 shows the spectra for a set of four closely spaced HCG-based VCSELs with different grating air spacing from 86 nm to 126 nm, but with the same grating period of 392 nm and the same oxide aperture of 2 μm , all biased at 1.4 times their threshold current. Despite the $\sim 40\%$ change in grating air spacing, all the devices lased with similar thresholds of $0.6\text{mA} \pm 0.15\text{mA}$ and slope efficiency from 0.16~0.58 mW/mA. As the efficiency has no obvious dependence on the HCG dimension, a large part of the variation is attributed to contact resistance variation, which is under investigation. The lasing wavelength blue shifts ~ 2 nm ($\Delta\lambda/\lambda=0.2\%$) when the grating spacing increases by 40 nm (40%).

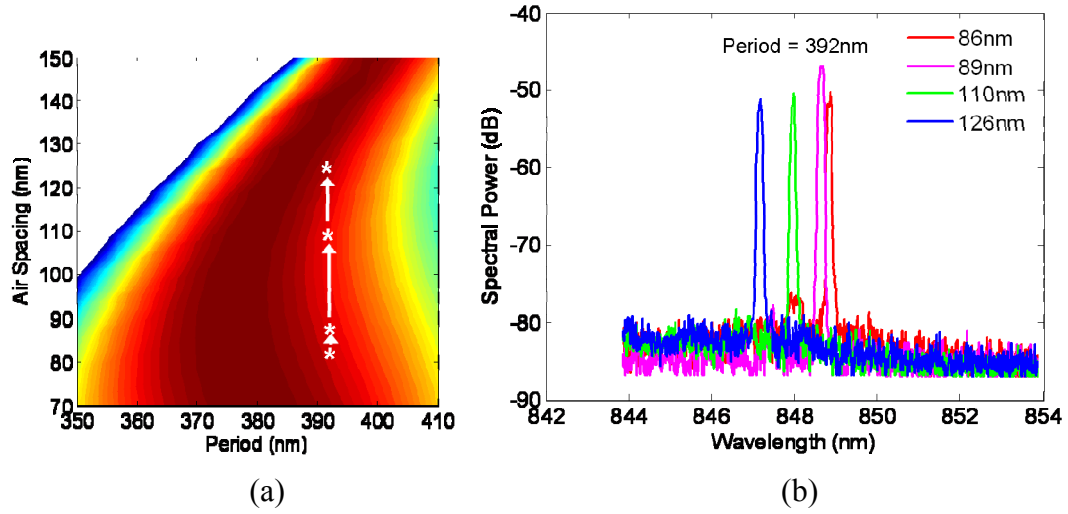


Figure 3.26 (a) Contour plot showing the relative parameters for four TM-HCG-based VCSELs with same period (392 nm) but with different grating spacing. (b) Measured spectra for fabricated TM-HCG-based VCSELs.

Similarly, a wavelength dependence study is performed for a set of four TM-HCG-based VCSELs with the same grating air spacing (94 nm) but different grating periods, ranging from 363nm to 392nm. All the devices lased with similar thresholds of $0.6\text{mA} \pm 0.15\text{mA}$ and slope efficiency from $0.25 \sim 0.59 \text{ mW/mA}$. Similarly, there was no trend of efficiency in the HCG period. The lasing wavelength (measured at 1.4 times threshold) also only red shifts $\sim 2 \text{ nm}$ ($\Delta\lambda/\lambda=0.2\%$) when the grating period is varied by 30 nm ($\sim 10\%$) as shown in Figure 3.27. This is a sharp contrast to that of typical VCSELs, where a layer thickness change of 1% translates into 0.1~1% change of the emission wavelength [33].

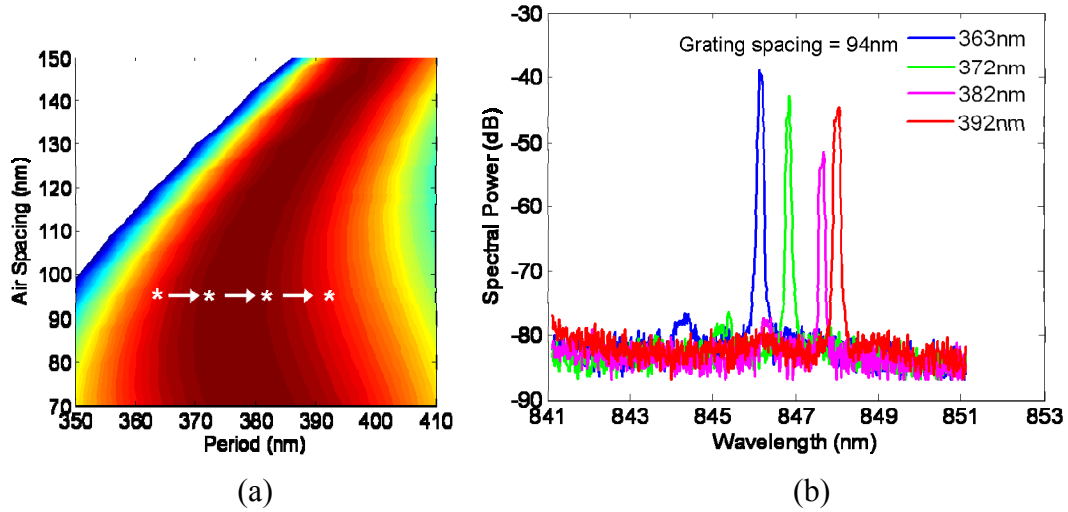


Figure 3.27 (a) Contour plot showing the relative parameters for four TM-HCG-based VCSELs with same grating spacing (94 nm) but with different grating periods. (b) Measured spectra for the fabricated TM-HCG-based VCSELs.

3.7.4 Dimension Tolerance for Non-uniform Gratings

In the previous section, we discussed HCGs with evenly distributed period and air spacing. In this section, to study the fabrication tolerance for HCGs with non-uniform grating spacing and period distribution within the same grating, each individual stripe of HCG was intentionally designed and fabricated with a random and non-uniform distribution. Figure 3.28 (a) shows the SEM image of a grating with a non-uniform distribution of the grating spacing, where the variation presumes a random Gaussian profile as shown in Figure 3.28 (b). The average grating spacing size is 97 nm and the standard deviation is as large as 27 nm, nearly $\pm 30\%$ of the average. Despite the large variation, the HCG-based VCSEL with the random grating still lased with a threshold current of ~ 0.55 mA as shown in Figure 3.28 (c).

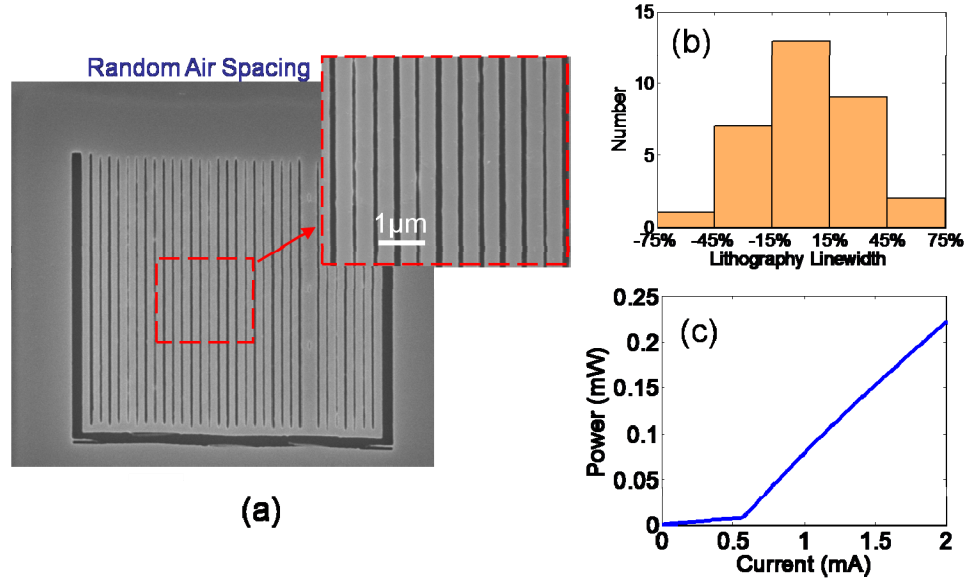


Figure 3.28 (a) SEM image of a non-uniform grating with random grating spacing. (b) Grating spacing distribution of the non-uniform grating. (c) LI curve of a HCG-based VCSEL with the non-uniform grating.

Similarly, we also studied gratings with a non-uniform distribution of period. Figure 3.29 (a) shows the SEM image of such a grating, and the period distribution of this grating follows the random Gaussian profile shown in Figure 3.29 (b). The average of the period is 374 nm and the standard deviation is 18 nm. The LI curve of the HCG-based VCSEL with this grating is shown in Figure 3.29 (c). The results from these non-uniform HCG-based VCSELs show large fabrication tolerances of lithography imperfections for the HCG.

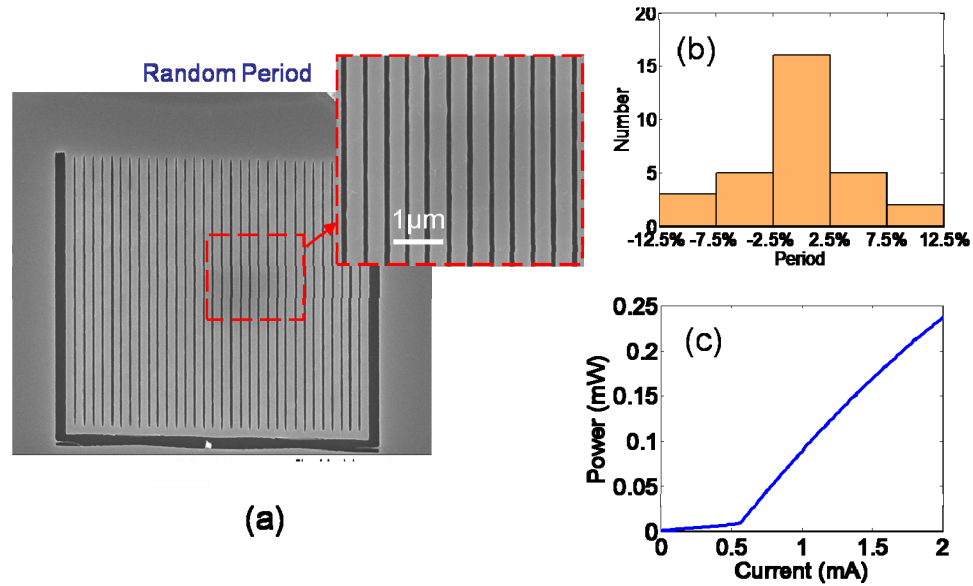


Figure 3.29 (a) SEM image of a non-uniform grating with random grating periods. (b) Grating period distribution of the non-uniform grating. (c) LI curve of a HCG-based VCSEL with the non-uniform grating.

The large fabrication tolerance of the HCG structure originates from its broadband nature and wavelength scalability. HCG is a broadband high reflective mirror (in this design, the high reflective band $\Delta\lambda/\lambda > 12\%$ for reflectivity $> 99.5\%$). Also, by varying the geometric dimension of HCG, the reflective spectrum of the HCG can be scaled accordingly. Therefore, to achieve a high reflectivity for a specific wavelength, variations in HCG parameters can be tolerated as long as the high reflective stop band still covers that wavelength. This leads to the large fabrication tolerance of the HCG-based VCSEL fabrication. Although we used TM-HCG-based VCSEL in this study, TE-HCG-based VCSEL has a similar tolerance for fabrication imperfection.

3.7.5 Lithography Alignment Tolerance

In section 3.6.4, we showed that the TM-HCG can be as small as $4 \times 4 \mu\text{m}^2$ while still maintaining the high reflectivity required to achieve lasing condition, and the smallest

TE-HCG size can be as small as $3 \times 3 \mu\text{m}^2$. Therefore, for the HCG with a relatively large size (10-12 μm), a few μm of lithography misalignment between the grating center and the VCSEL mesa (hence the oxide aperture) is tolerable. This is true as long as the HCG area is sufficiently large to cover the emission beam of the laser. Figure 3.30 shows a SEM image of a $12 \times 12 \mu\text{m}^2$ TM-HCG with an estimated aperture alignment tolerance window.

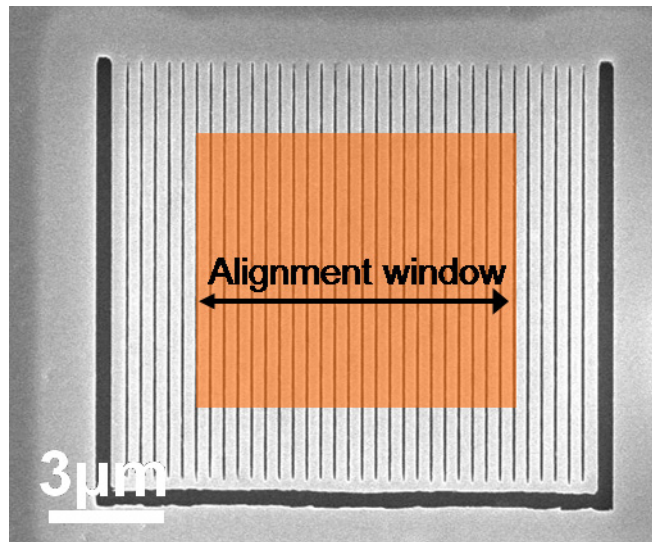


Figure 3.30 SEM image of a $12 \times 12 \mu\text{m}^2$ TM-HCG with an estimated aperture alignment tolerance window.

3.8 Summary

We present a novel HCG-based VCSEL where the conventional DBR mirror is replaced with a single-layer HCG mirror. Both TM-HCG-based and TE-HCG-based VCSEL are designed and experimentally demonstrated with excellent optical lasing performance. A systematic and comprehensive review of the experimental and numerical simulation results is presented to demonstrate many desirable attributes of HCG-based

VCSELs, including polarization selection, transverse mode control, and a large fabrication tolerance.

We show that HCG-based VCSELs exhibit strong polarization selection and that the output emission polarization can be controlled by lithography process. An orthogonal polarization suppression ratio (OPSR) of 36dB is obtained under CW operation, and an OPSR of 28 dB is obtained under dynamic modulation.

We also show that, due to the angular dependence of HCG, HCG can effectively discriminate the higher-order transverse modes for oxide-VCSELs with up to a 6 μm aperture with a large side-mode suppression ratio >40 dB. Furthermore, a single mode, high output power of ~ 2.5 mW was experimentally demonstrated using a HCG-based VCSEL with a 10 μm oxide aperture. The size dependence of HCG is also studied. We show that to provide reflectivity higher than 99.5%, the smallest TM-HCG can be as little as $4 \times 4 \mu\text{m}^2$ (11 periods) and the smallest TE-HCG can be only $3 \times 3 \mu\text{m}^2$ (4 periods!).

Finally, we report the experimental demonstration of the large fabrication tolerance for HCG-based VCSELs. We investigate gratings with uniform dimensions, as well as gratings with non-uniform geometries within the grating. For uniform gratings, HCG-VCSELs work well with as large as $\pm 20\%$ variation in the HCG critical dimension (the grating air spacing). For non-uniform, random gratings, this variation can be even higher, up to $\pm 30\%$. We demonstrate that emission wavelength only varies 2 nm ($\Delta\lambda/\lambda=0.2\%$) with 40% change in grating spacing or 8% change in grating period. The large fabrication tolerance makes HCG-VCSEL well suited for low-cost and high-throughput manufacturing technology, such as nano-imprinting.

Chapter 4 HCG-based Tunable VCSELs

4.1 Introduction

Tunable lasers are widely recognized as highly desirable components for dense wavelength-division multiplexing (DWDM) systems [43]. A wavelength-tunable semiconductor laser is constructed by combining an optical micro-electromechanical (MEM) mirror with a VCSEL [44-47]. These mechanically tunable lasers have been studied extensively for various applications, including: telecommunication [44,48], bio-molecular and chemical sensing [49], spectroscopy [50], and chip-scale atomic clock [51,52]. The MEM tunable structures are desirable because they provide for a large and continuous tuning range with high precision and fast response. The monolithic integration of VCSEL and MEMS brings together the best of both technologies and results in an unprecedented performance in wavelength tunable lasers with simple electrical control.

Previous demonstrations of MEM tunable VCSELs used a MEM design that was relatively large, typically $\sim 200 \mu\text{m}$ long and $10\text{-}20 \mu\text{m}$ wide. The main reason for such a

large size is due to the thickness of the top DBR, which is held on the end of the micromechanical structure [44]. The wavelength tuning is accomplished by applying a voltage between the top DBR and the laser's active region, across the air gap. The applied bias generates the electrostatic force, which attracts the top DBR downward toward the substrate. This physical movement changes the optical length of the laser cavity and thus produces a change (blue-shift) in the laser emission wavelength. In order to achieve a large tuning range with a small voltage, the entire MEM structure must be scaled with the DBR thickness. The large mass of the movable mechanical structures translates into a slow tuning speed and high actuation power, as well as processing difficulties.

The HCG is naturally suitable for forming a tunable MEM structure. With its ultra-thin layer, 10-20 times thinner than a typical DBR, the other two dimensions of the MEM structure can be reduced by similar numbers, resulting a 1,000-8,000 times mass reduction and a 60~160 times increase in tuning speed. This allows for a wavelength-tunable light source with potentially tens of nanoseconds switching speed and suggests various new areas of practical applications such as bio- or chemical sensing, chip-scale atomic clocks, and projection displays.

In this chapter, we present a HCG-based tunable VCSEL by integrating a single-layer compact HCG with nano-electromechanical actuators to create a movable reflector. Due to the small mass of the HCG, a record-fast wavelength tuning is experimentally demonstrated.

4.2 Design

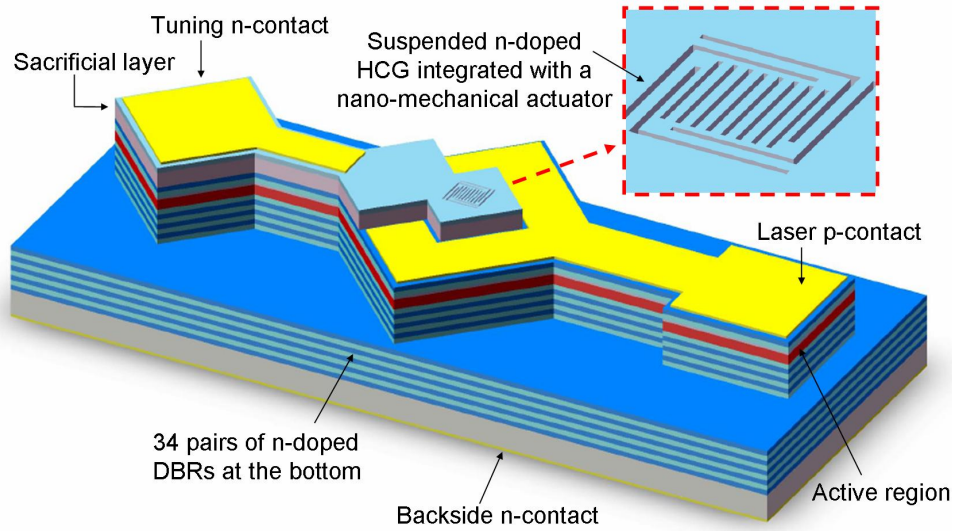


Figure 4.1 Schematic of the HCG-based tunable VCSEL using the highly reflective subwavelength high-contrast grating as its top mirror, instead of conventional distributed Bragg reflectors.

Figure 4.1 shows the device schematic and the cross-section of the tunable VCSEL. The device consists of an n-doped HCG top mirror, a sacrificial layer, two (or four) pairs of p-doped DBR, an AlAs oxidation layer, a cavity layer containing the active region, and a bottom standard n-doped DBR mirror, all monolithically grown on a GaAs substrate. The main difference from the regular HCG-based VCSELs is that, in the tunable structure, the sacrificial layer (to be removed, forming the airgap) is typically undoped and the HCG layer is n-doped, instead of both being p-doped. Electrical current injection is conducted through the middle laser p-contact (via 2 pairs of p-doped DBRs above the cavity layer) and the backside n-contact (via substrate). An aluminum oxide aperture is formed on the AlAs layer, just above the active region, to provide current and optical confinement.

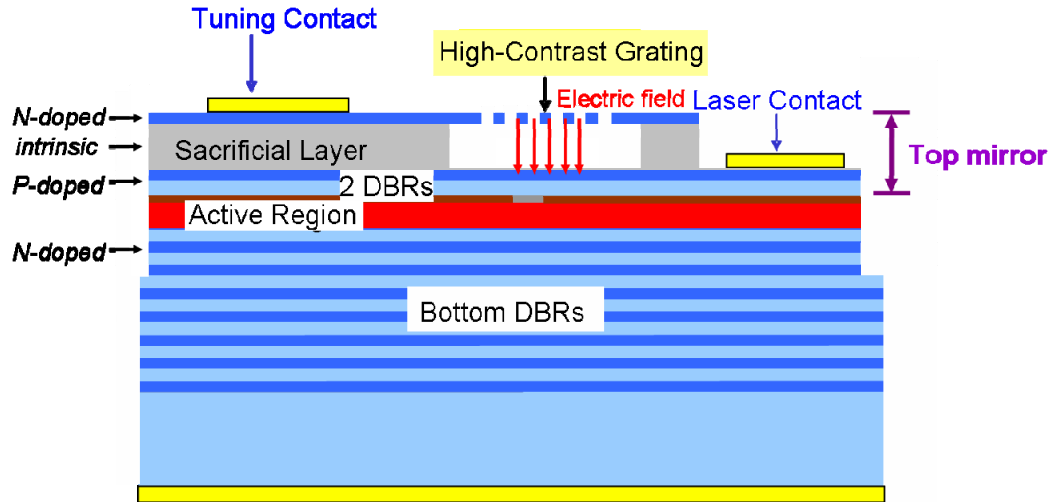


Figure 4.2 Schematic showing the cross-section epitaxial design of a HCG-based tunable VCSEL using the highly reflective HCG top mirror.

The cross-sectional design of the device is shown in Figure 4.2. The HCG is freely suspended above a variable airgap and supported via a nano-mechanical structure. Various MEM supporting structures, including cantilever, bridge, folded-beam (shown in Figure 4.1), and membrane (4-fold supported bridge), are fabricated to experimentally study their trade-offs in voltage and tuning speed. The tuning contact is fabricated on the top *n*-doped HCG layer. The top two contacts provide a bias across the gap between the HCG and the active region. Using a reverse bias in this junction, the electric field resulting from the p-n junction charges attracts the HCG downwards, which thus shortens the laser cavity length and blue-shifts the lasing wavelength. The tuning range is limited primarily by the movable distance to approximately 1/3 of the airgap and the reverse breakdown voltage [44].

The HCG-based tunable VCSEL epitaxy wafer has the following layer structure: the bottom, silicon-doped DBR is composed of 34 pairs of $\text{Al}_{0.12}\text{Ga}_{0.88}\text{As}$ / $\text{Al}_{0.9}\text{Ga}_{0.1}\text{As}$. The nominally undoped, one- λ cavity contains three 6 nm GaAs quantum wells surrounded by

8 nm $\text{Al}_{0.3}\text{Ga}_{0.7}\text{As}$ barriers and sandwiched by an $\text{Al}_{0.6}\text{Ga}_{0.4}\text{As}$ cladding layer. To provide current injection into the active region, 2 pairs (or 4 pairs) of carbon-doped $\text{Al}_{0.12}\text{Ga}_{0.88}\text{As}$ / $\text{Al}_{0.9}\text{Ga}_{0.1}\text{As}$ are used immediately above the active region. Within that, a 30 nm $\text{Al}_{0.98}\text{Ga}_{0.02}\text{As}$ is used as the thermal oxidation layer. Above the current injection layer is a 1.1 μm un-doped GaAs sacrificial layer and a silicon-doped $\text{Al}_{0.6}\text{Ga}_{0.4}\text{As}$ HCG layer. The HCG layer thickness is 235 nm for TM-HCG design and 140 nm for TE-HCG design. The detailed HCG design parameters can be found in Chapter 2.

4.3 Fabrication

The fabrication process flow of a HCG-based tunable VCSEL is shown in Figure 4.5. The process starts with an epitaxial GaAs wafer grown by metal organic chemical vapor deposition (MOCVD) (Figure 4.5 (a)). The first step is mesa formation by etching down to the bottom DBRs (Figure 4.5 (b)), followed by thermal oxidation to form the oxide aperture ($\sim 3 \mu\text{m}$) (Figure 4.5 (c)). The next step is the top and back-side contact metal depositions, created by using electron-beam evaporator to deposit Ni-Ge-Au metal alloy (Figure 4.5 (d)). Then, part of the mesa surface is etched to expose the p-doped current injection layer, on top of which the laser contact metal (Ti-Au) is deposited (Figure 4.5 (e)). After this, the HCG is patterned by electron-beam lithography on poly-methyl methacrylate (PMMA) photoresist and pattern-transferred by reactive ion etching, where the HCG is aligned to the mesa center (oxide aperture) (Figure 4.5 (f)). Finally, a selective etch process is carried out, followed immediately by a CO_2 critical point drying process, to remove the GaAs sacrificial material underneath the HCG layer and form the freely suspending grating structure (Figure 3.3 (g)).

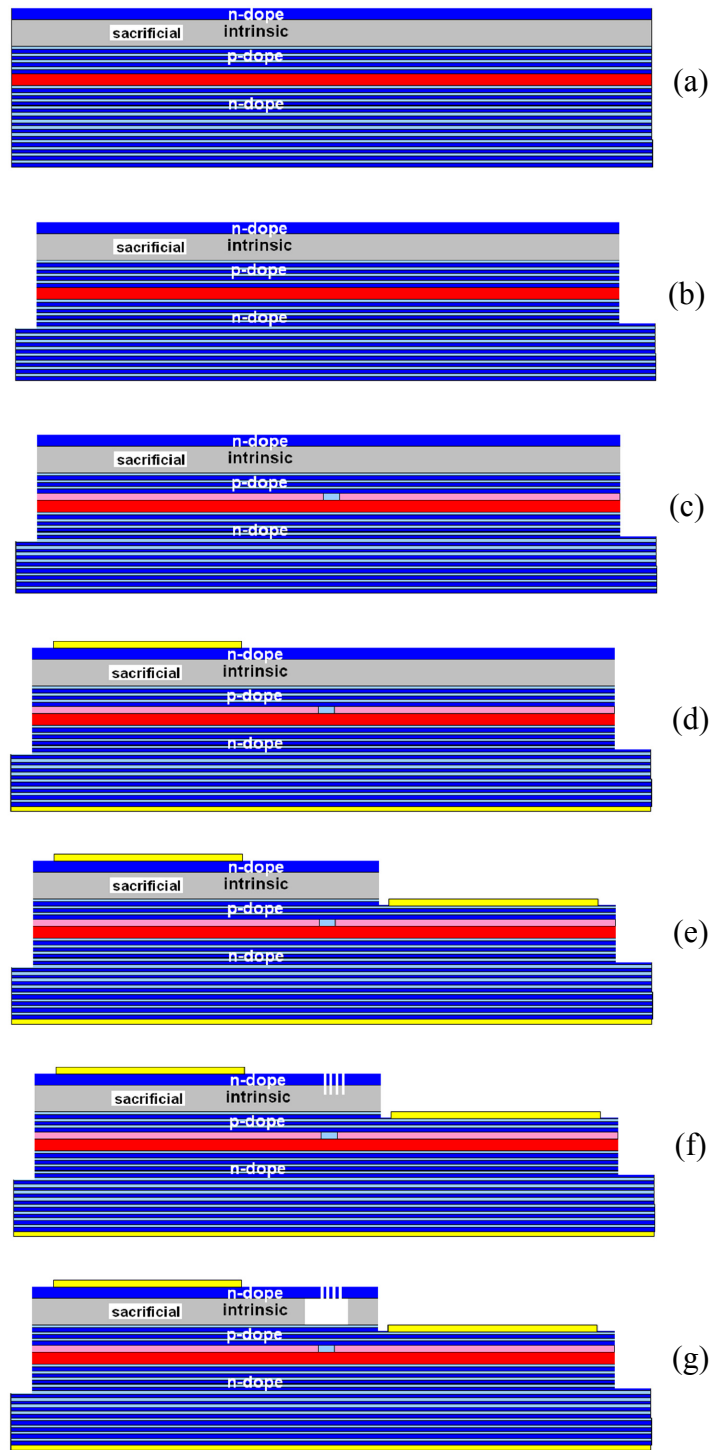


Figure 4.3 Fabrication process flow of a HCG-based tunable VCSEL. (a) starting epitaxial wafer (b) device mesa formation (c) thermal oxidation (d) top and back metal contact deposition (e) laser contact etch and deposition (f) electron-beam lithography and reactive ion etching (RIE) (g) selective wet etching removing sacrificial layer and critical point drying.

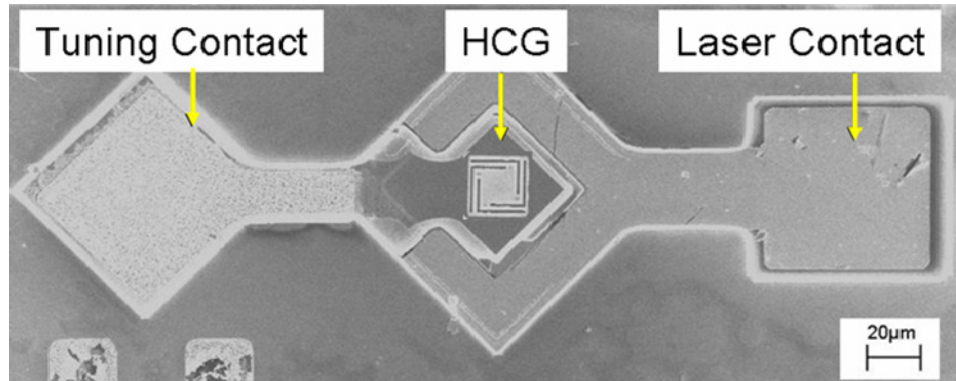


Figure 4.4 SEM image of the fabricated TM-HCG-based tunable VCSEL.

Figure 4.4 shows the top view SEM image of the fabricated TM-HCG-based tunable VCSEL with the HCG aligned to the oxide aperture in the mesa center. The tuning contact, laser contact, and HCG mirror are labeled in the figure. The MEM structure in this case is a folded-beam design.

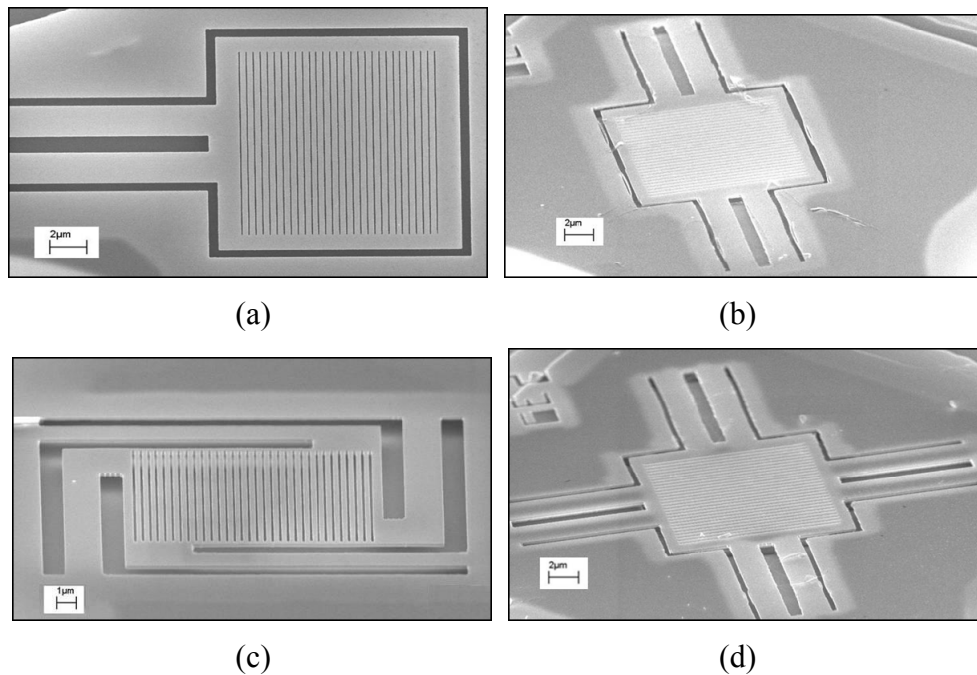


Figure 4.5 SEM image of the freely suspended HCG mirror with a variety of MEM structure including (a) cantilever, (b) bridge, (c) folded-beam, and (d) membrane.

In order to design for different mechanical stiffness depending on the application requirement, several different mechanical supporting structures were fabricated. Figure 4.5 shows the freely-suspended HCG mirror with a variety of MEM structure including cantilever, bridge, folded-beam, and membrane.

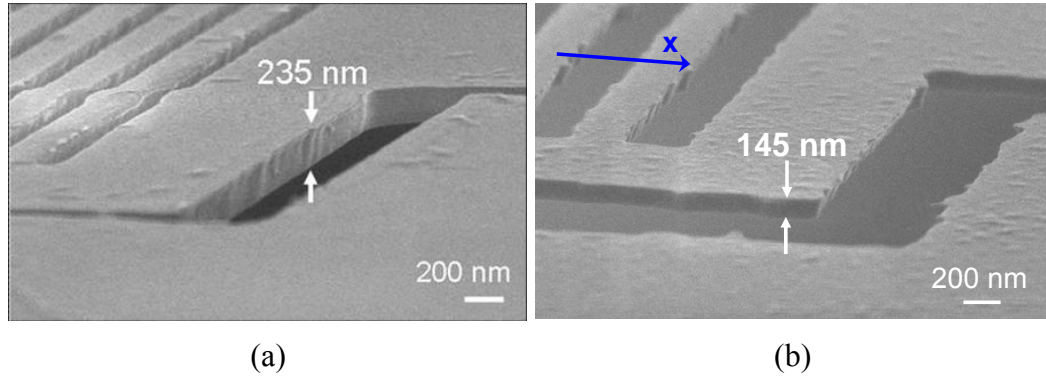


Figure 4.6 (a) SEM image of a fabricated TM-HCG with a grating thickness of 235 nm. (b) SEM image of a fabricated TE-HCG with a grating thickness of 145 nm.

Both TM-HCG-based and TE-HCG-based tunable VCSELs are fabricated. The SEM images in Figure 4.6 (a) and (b) clearly show the grating thicknesses of a TM-HCG and TE-HCG, respectively. The TM-HCG movable mirror has a thickness of 235 nm, while the thickness of the TE-HCG movable mirror is only 145 nm. Both HCGs provide similar ultra-high reflectivity and bandwidth, which is required for the top mirrors in VCSELs, as discussed in Chapter 2.

As a comparison, for a conventional MEM tunable VCSEL, the mechanical beam dimensions are usually about $\sim 200\text{-}300\ \mu\text{m}$ in length, $\sim 20\ \mu\text{m}$ in width, and $\sim 3\text{-}5\ \mu\text{m}$ in thickness. Figure 4.7 (a) shows the SEM images of a DBR-based MEM tunable VCSEL previously fabricated by our group. With the ultra-thin thickness of HCG, 10-20 times thinner than a typical DBR, the other two dimensions of the MEM structure can also be

reduced by similar numbers, resulting in a 1,000-8,000 times mass reduction and a 60~160 times increase in tuning speed. In Figure 4.7 (b), we show a SEM image of the smallest TE-HCG-based tunable VCSEL top mirror we fabricated. The HCG size is only $3 \times 3 \mu\text{m}^2$ and the HCG thickness is 140 nm. Clearly, by using HCG structure, tunable lasers with much a smaller size and a faster tuning speed can be obtained.

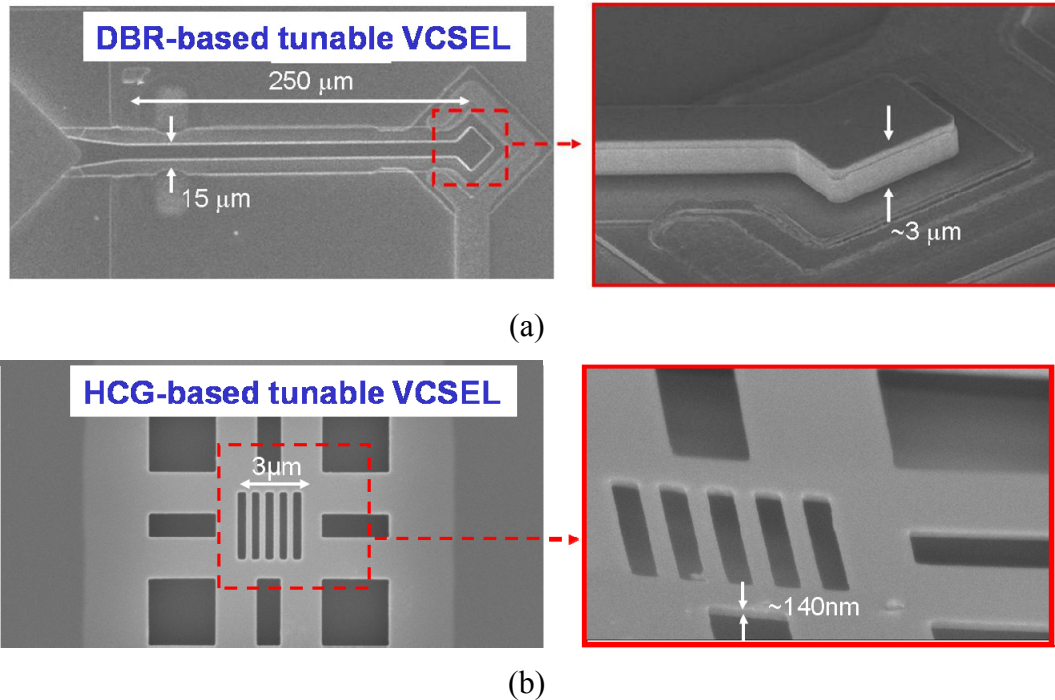


Figure 4.7 SEM images of (a) a DBR-based tunable VCSEL and (b) a HCG-based tunable VCSEL.

4.4 Optical Characteristics

Continuous-wave (CW) operation of HCG-based tunable VCSELs with excellent optical performance is demonstrated in this section. Figure 4.8 shows the output power and voltage versus current (LI and IV curves, respectively) for a typical tunable VCSEL with a TM-HCG and 2 pairs (or 4 pairs) of p-doped current injection DBR. With 2 pairs of p-doped DBR, the TM-HCG-based tunable VCSEL exhibits a very low threshold

current of 200 μA and an external slope efficiency 0.25 mW/mA. Compared to the one with 4 pairs of p-doped DBR, this threshold current is substantially lower. Since a p-doped region typically has a high free-carrier absorption, VCSELs with 2 pairs of p-doped DBRs may have a lower absorption loss, hence have a lower threshold current. We also noticed that, compared to the regular non-tunable TM-HCG-based VCSEL (Section 3.4.1), the threshold current of the tunable one is lower. We attribute this to the lower free-carrier absorption in n-doped HCG. In addition, compared to a tunable VCSEL with a similar epitaxy structure but that utilizes a DBR-based movable top mirror (with $I_{\text{th}} \sim 1.2$ mA), both the reduction of threshold current and slope efficiency can be observed. This indicates that a much higher effective reflectivity is obtained by utilizing the single-layer HCG top mirror, in addition to the reduction of free-carrier absorption loss.

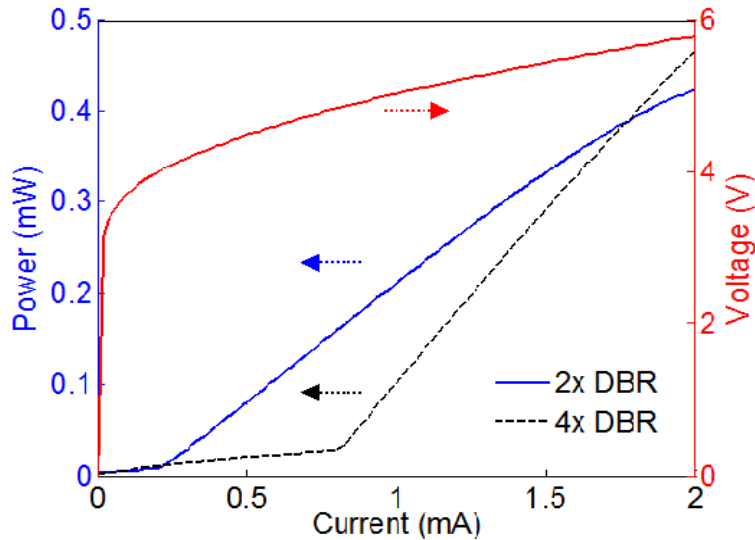


Figure 4.8 Optical characteristic of typical optical TM-HCG-based tunable VCSEL with 2 pairs and 4 pairs p-doped DBR, showing output power versus input current (LI) and voltage versus current (VI) under room temperature. For the HCG-based tunable VCSEL with 2 pairs of p-doped DBR, a very low threshold current of 200 μA is obtained.

There is usually a trade-off between threshold current and output power. While the ultra-high reflectivity in the HCG leads to a low threshold current but also lower VCSEL output power, reflectivity can be adjusted by optimizing the grating parameters lithographically to maximize VCSEL output power, but with only a slightly higher threshold current.

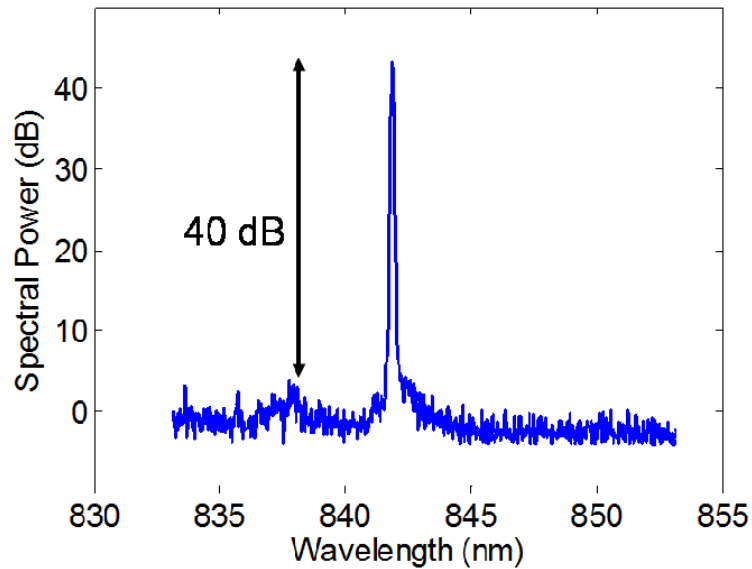


Figure 4.9 Measured single-mode emission spectrum for a TM-HCG-based tunable VCSEL, with a SMSR of 40 dB.

Figure 4.9 shows the measured device emission spectrum at 1 mA bias current. Single transverse mode emission with a >40 dB side-mode suppression ratio was obtained, where the discrimination of higher-order transverse modes is attributed to the finite grating effects in combination with the oxide aperture.

A TE-HCG-based VCSEL with 4 pairs of p-doped DBR is also fabricated. Figure 4.10 (a) shows the output power versus bias current (LI) curve of a device with a threshold current of 0.7 mA and output power >1.6 mW. External slope efficiency is 0.57 mW/mA. Figure 4.10 (b) shows a measured emission spectrum of the laser, when

biased at twice the threshold current. Single mode emission with a 40 dB side-mode suppression ratio was obtained.

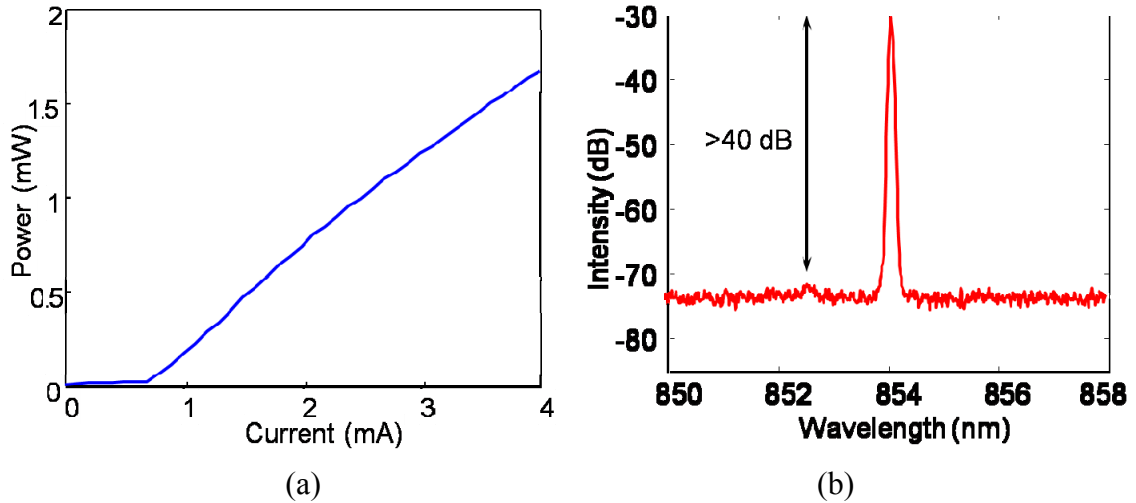


Figure 4.10 (a) Optical characteristic of typical optical TE-HCG-based tunable VCSEL showing output power versus input current (LI) under room temperature. The device has a low threshold current of 0.7 mA and an output power of >1.6 mW. (b) Measured single-mode emission spectrum when biased at twice the threshold current, showing a >40 dB SMSR

4.5 Wavelength Tuning Range

4.5.1 Tuning Principle

Electrostatic actuation of the MEM structure is used to change the effective cavity length of the VCSELs, and hence to tune the wavelength of the output light. The MEM tunable structures are desirable because they provide for a large and continuous tuning range with high precision and fast response. Wavelength tuning of the HCG-based tunable VCSEL is accomplished by applying a reverse voltage bias across the tuning contact and the laser contact, while a constant electrical current is applied between the laser and backside contact. When applying a reverse bias voltage across the tuning contacts, the electrostatic force deflects the cantilever beam, which translates to a

decrease in the laser emission wavelength. The reverse bias across the *pin* junction results in a negligibly small leakage current of ~ 10 nA, which does not affect the operation of the VCSEL current injection.

4.5.2 Devices With 4 Pairs of p-DBR

Figure 4.11 (a) shows the emission tuning spectra of a TM-HCG-based VCSEL with 4 pairs of p-DBR. The active region is electrically pumped at 1.8 times I_{th} , with various applied voltages across the tuning contact. A continuous wavelength tuning range of ~ 2.5 nm was obtained towards shorter wavelength. Figure 4.11(b) shows the emission wavelength as a function of the applied voltage and the corresponding spectral intensity under those tuning conditions. The wavelength tuning exhibits a quadratic-like behavior known to typical electrostatic actuation. In addition, the emission spectral intensity remains fairly constant throughout most of the tuning range.

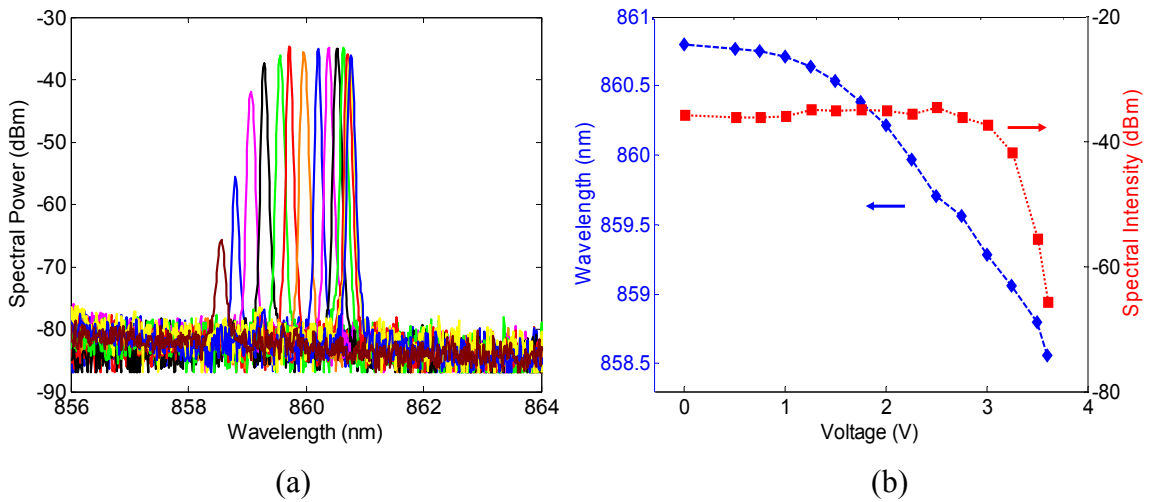


Figure 4.11 (a) CW tuning spectra for the TM-HCG-based tunable VCSEL with 4 pairs of p-DBRs under various external applied voltages across the HCG cantilever. (b) Measured emission wavelength as a function of applied external voltage and measured peak spectral intensity as a function of applied voltage.

Figure 4.12 shows the emission tuning spectra of a TE-HCG-based VCSEL with 4 pairs of p-DBR. The active region is electrically pumped at 1.5 mA under various applied tuning voltages, and a continuous wavelength tuning range of 4 nm was obtained with 7 V of external applied voltage. The laser remains in single mode emission throughout the entire tuning range.

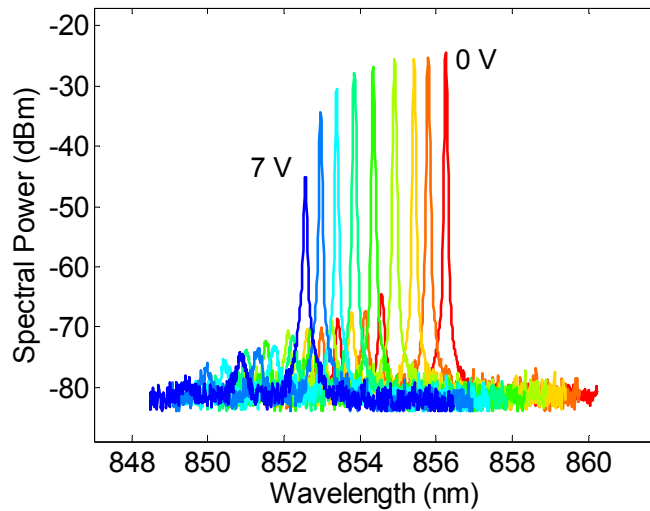


Figure 4.12 CW tuning spectra for the TE-HCG-based tunable VCSEL with 4 pairs of p-DBRs under various external applied voltages across the HCG cantilever.

For HCG-based tunable VCSELs with 4 pairs of p-DBR, the wavelength tuning range is limited at about 3-4 nm. This is mainly due to the 4 pairs of DBR, which reduce the wavelength tuning efficiency ($\Delta\lambda/\Delta\text{airgap}$ efficiency). For the same amount of HCG deflection, and the fewer the number of p-DBR is, the more emission wavelength change there will be. Therefore, by reducing the number of p-DBR pairs, we can get a larger wavelength tuning efficiency, and hence a larger wavelength tuning range. In the next section, we will present a HCG-based tunable VCSEL with 2 pairs of p-DBR, and indeed we get a much larger wavelength tuning range.

4.5.3 Devices With 2 Pairs of p-DBR

To further improve the tuning range of a HCG-based tunable VCSEL, devices with 2 pairs of p-DBR are fabricated. Figure 4.13 shows the measured wavelength tuning spectra of a fabricated TM-HCG-based VCSEL with 2 pairs of p-DBR. The movable TM-HCG mirror is integrated with a bridge structure for mechanical actuation. The device is electrically pumped at ~ 1.2 times the threshold current and actuated under various applied voltages across the tuning contact. An 8 nm continuous wavelength tuning toward the shorter wavelength is first obtained within 0-6 V of external applied voltage. The VCSEL stops lasing when the external applied voltage is further increased, as the optical loss becomes larger than the laser gain. Until the voltage reaches 9 V, the device starts lasing again, but at another longitudinal mode, and continuously tunes again for 13 nm over the applied voltage range of 9-14 V. With the total spectral overlap, an overall continuous wavelength tuning range of 18 nm is experimentally obtained.

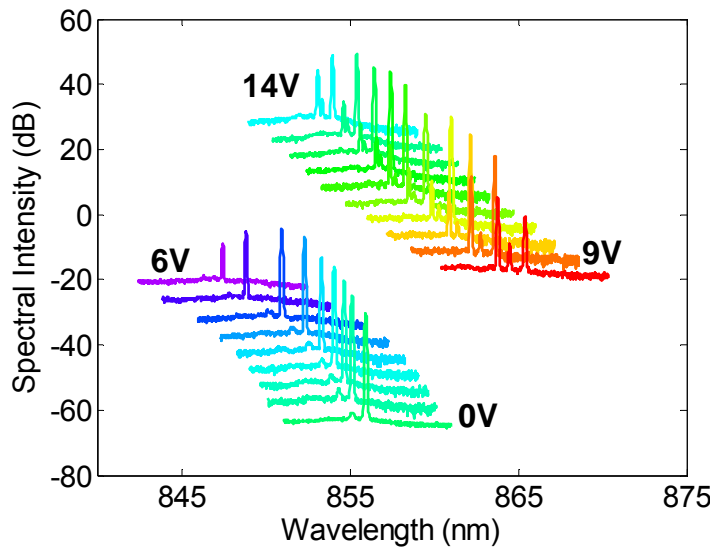


Figure 4.13 Measured continuous wavelength tuning spectra of a TM-HCG-based tunable VCSEL, with an 18 nm tuning range.

When the VCSEL is being tuned, threshold current and slope efficiency are measured as a function of emission wavelength. Figure 4.14 shows the threshold current and slope efficiency of the TM-HCG-based VCSEL under the respective tuning wavelength, indicating the increased optical loss when the laser wavelength is tuned toward both edges of the tuning spectrum.

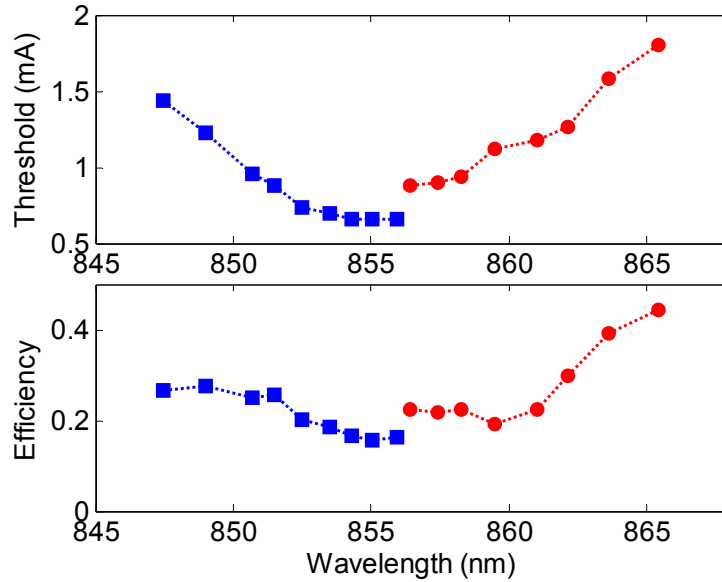


Figure 4.14 Measured laser threshold current and slope efficiency of the TM-HCG-based VCSEL under the corresponding emission wavelengths.

Numerical simulation is performed to understand the wavelength-tuning behavior. We calculated the emission wavelength as a function of the airgap thickness for the designed tunable VCSEL, as shown by the blue curves in Figure 4.15. In principle, the wavelength tuning range should be limited by the free-spectral range of the optical cavity (~ 40 nm), if the airgap can be changed from 1.2 to 0.8 μm for example. The reflection bandwidth of the HCG top mirror also varies as the airgap changes, since the airgap also contributes to the overall mirror reflectivity depending on its optical length.

In our experimental device, the airgap is originally designed to be 1.1 μm . It is moved from 1.1 μm to ~ 0.73 μm , with increasing voltage from 0 to 14V. The laser does not lase from 6-9V, which is attributed to a reduced mirror reflectivity and bandwidth as the cavity wavelength tunes towards the edge of the free spectral range. The white curve shows the 99.9% reflectivity line to illustrate the effect. We anticipate a larger wavelength tuning range of 35-40 nm by optimizing the HCG top mirror to yield a much broader reflection bandwidth, so that the wavelength tuning curve overlaps entirely within the high reflectivity bandwidth of HCG.

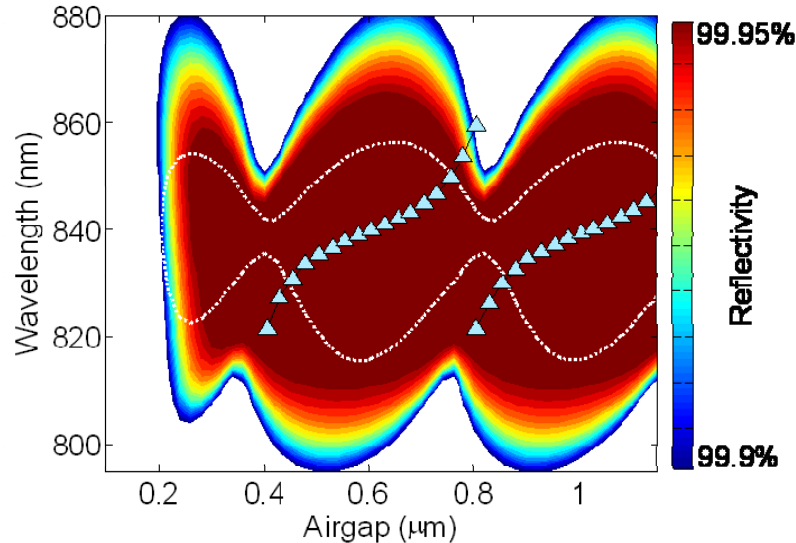


Figure 4.15 Calculated wavelength tuning behavior of the TM-HCG-based tunable VCSEL (blue curves) and the TM-HCG reflection bandwidth (color-coded contour) as a function of the airgap thickness. The dotted white curve is the $>99.9\%$ reflection line.

4.6 Wavelength Tuning Speed

4.6.1 Measurement Method

In order to measure the tuning speed of a HCG-based tunable VCSEL, the mechanical response of the HCG structure is measured by applying a sinusoidal AC

modulating voltage in addition to a DC voltage while the VCSEL is injected with constant current, as shown in Figure 4.15. The emission light is then collected by an optical fiber and sent to the optical spectrum analyzer. Since the signal integration time of an optical spectrum analyzer is much slower compared to the voltage modulation, a spectrally broadened emission can be observed as the nano-mechanical actuator (and hence the emission wavelength) is being modulated. By plotting the spectral broadening as a function of modulation frequency, we can obtain a Bode plot for the mechanical response of the HCG tuning structure. The mechanical resonant frequency of the HCG tuning structure and the wavelength tuning speed can then be calculated.

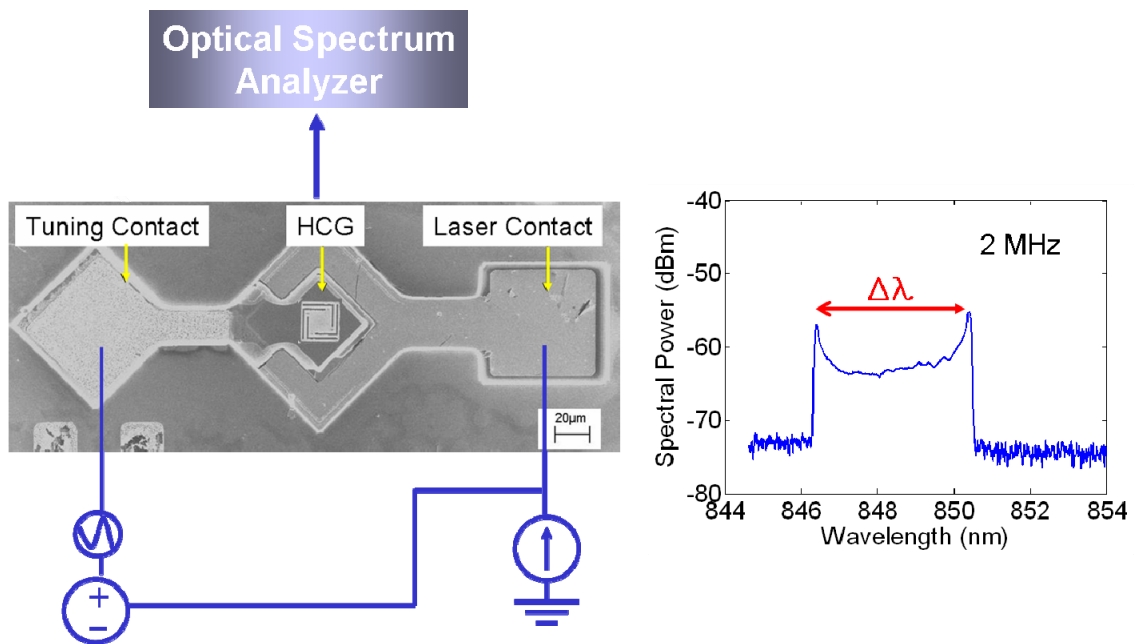


Figure 4.16 Optical setup used to characterize the mechanical frequency response for HCG structures, by using an optical spectrum analyzer to monitor the wavelength broadening under modulation.

4.6.2 TM-HCG-based Tunable VCSEL

By adopting the measurement method described in the previous section, the mechanical response of various TM-HCG tuning structures is measured, as shown in

Figure 4.17. Among the different mechanical structures, the membrane actuator exhibits the fastest mechanical resonant response with a 3dB frequency bandwidth of 3.3 MHz, or equivalently, the tuning speed of this device is calculated to be about 150 ns. Compared to the existing DBR-based electrostatic-actuated MEM VCSEL (with tuning speed $\sim 10 \mu\text{s}$), the demonstrated HCG-based tunable VCSEL has a $\sim 40\text{-}50$ times faster wavelength tuning speed.

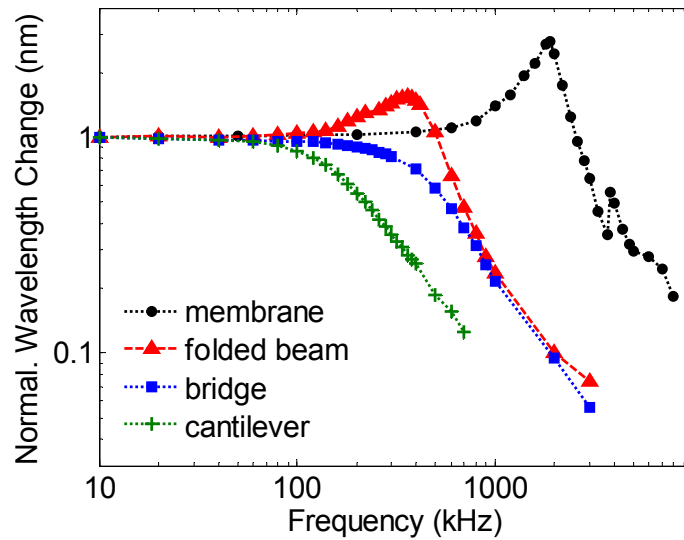


Figure 4.17 Measured mechanical response of various HCG tuning structures by using an optical spectrum analyzer while modulating the mechanical actuator.

4.6.3 TE-HCG-based Tunable VCSEL

The thickness of TE-HCG is only half of the TM-HCG thickness, which results in a much smaller HCG mass and an even fast wavelength tuning speed. A set of TE-HCG-based tunable VCSELs with different HCG mirror sizes were fabricated for tuning speed measurement. Figure 4.18 shows the measured frequency response curves for devices with 4 different mirror sizes of 10×10 , 8×8 , 6×6 , and $4 \times 4 \mu\text{m}^2$. The resonance frequency and 3 dB frequency bandwidth for the devices with different mirror sizes are plotted in

Figure 4.19. The device with a $4 \times 4 \mu\text{m}^2$ TE-HCG mirror was measured with a peak resonant frequency of 5.3 MHz and 3 dB frequency bandwidth of 7.9 MHz. The tuning speed of this device is estimated to be ~ 60 ns. This is >150 times faster than the existing DBR-based tunable VCSELs ($\sim 10 \mu\text{s}$), and a 2.5 times improvement over the TM-HCG-based tunable VCSEL (~ 150 ns) in the previous section. The frequency response of the small TE-HCG also exhibits a higher Q due to the higher mechanical stiffness. Damping is primarily due to air drag on the mechanical actuators, which can be reduced by properly packaging the devices.

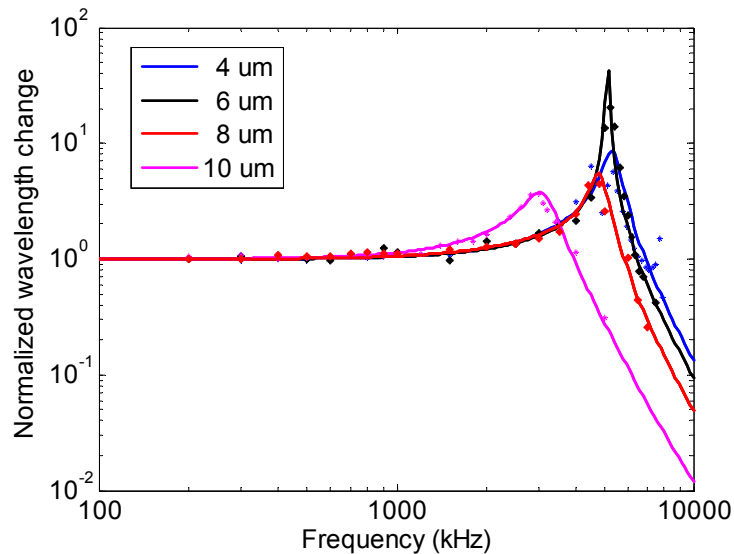


Figure 4.18 Measured frequency response of TE-HCG-based tunable VCSELs with mirror sizes of 4×4 , 6×6 , 8×8 and $10 \times 10 \mu\text{m}^2$.

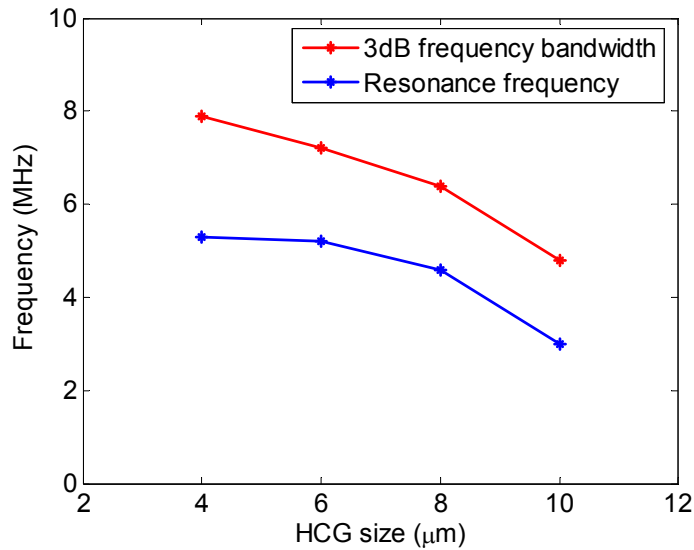


Figure 4.19 Measured resonance and 3 dB frequency as a function of TE-HCG mirror size.

4.6.4 Comparison

Various mechanically tunable VCSEL technologies are compared in Figure 4.20, which shows the calculated tuning speed and actuating voltage as a function of the mechanical beam length. As an illustration, the tuning speed and voltage trade-off is calculated for two mechanical actuators: cantilever and membrane. Clearly, when scaling down the mechanical actuators, especially from the DBR micro-electromechanical to HCG nano-electromechanical mirror, a drastic tuning speed improvement can be obtained while also reducing the required actuating voltage. The solid data points represent experimental data obtained here and in references, which shows excellent agreements with the calculation. With a thickness reduction that enables further scaling down of the mechanical component, an even faster tuning speed (close to 10 ns) can potentially be attained.

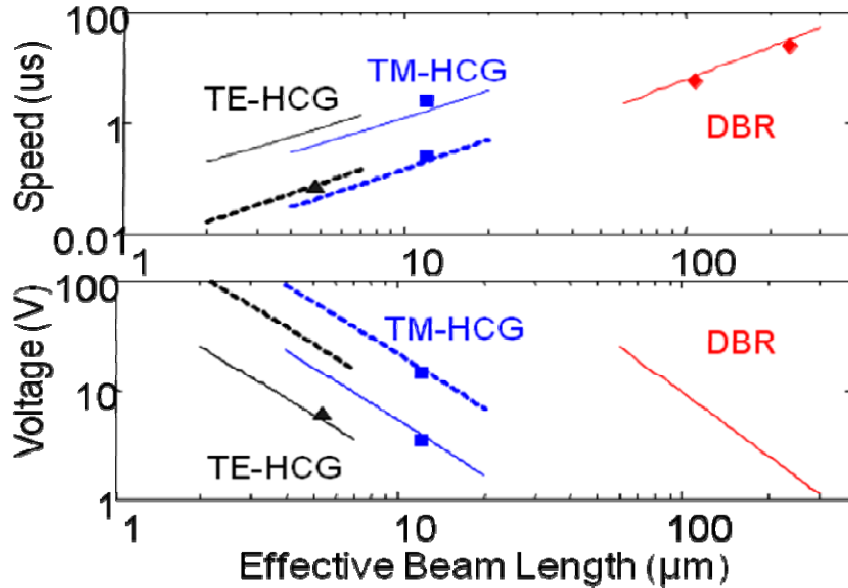


Figure 4.20 Calculated tuning speed and voltage as a function of mechanical beam length when utilizing different mirror structures (DBR, TM-HCG, and TE-HCG) integrated with different mechanical actuators: cantilever (solid) and membrane (dashed). The solid data points represent data obtained here and in references. Excellent agreements are obtained.

4.7 Summary

We presented an ultra-fast tuning, HCG-based tunable VCSEL. By integrating a mechanically movable actuator with a single-layer HCG as the VCSEL top mirror, single mode operation with SMSR > 40dB, an ultra-low threshold current (200 μ A), and a precise, wide, continuous wavelength tuning (\sim 18 nm) was obtained at room temperature. The small footprint of the HCG enables the scaling down of the mechanical actuating component, which results in a drastic reduction in mass and a 160 times improvement in tuning speed. A tunable VCSEL with \sim 60 ns wavelength tuning time is obtained, which is the fastest MEM tunable device reported to date. By using electrostatic actuation to control the airgap below the HCG, compact and efficient wavelength-tunable VCSELs with a precise and continuous tuning range and an ultra-low power consumption are

demonstrated. There are numerous applications for HCG-based tunable structures, including wavelength-tunable optoelectronic devices such as VCSELs, optical filters, detectors, and sensors.

Chapter 5

HCG-based Surface Normal High-Q Resonator

5.1 Introduction

High-quality (Q) factor optical resonators have attracted much attention with their various applications, which include lasers, single photon sources, optical filters, and sensors [53-58]. Various structures have been used to form high-Q resonators, including microdisks, photonic crystals, ring resonators, distributed Bragg reflectors (DBRs), and distributed feedback (DFB) structures [53,54,59-61]. Most of them employ a collinear configuration for the resonant optical mode and optical output. While such a configuration facilitates device integration in a cascaded fashion, it does not facilitate simple coupling with fiber or free-space optics. A high-Q resonator with surface-normal emission is of great interest for many applications, such as lasers, optical filters, and sensors.

Anomalies in periodically modulated grating structures have been widely studied [62-64], and it has been shown that gratings with a subwavelength modulation in the

refractive index can function as filters, due to the guided-mode resonance [64]. This resonance has been successfully exploited in the development of some sensor applications [65, 66], though the refractive index modulations in most previous gratings are relatively weak. In the previous chapters, we proposed a novel subwavelength high-index-contrast grating (HCG) as a broadband reflector for an optical beam propagating in the direction perpendicular to the grating plane. The very large periodic index contrast from the gratings in the in-plane direction results in an efficient coupling of the surface-normal waves with the in-plane waves, and hence, yields ultrahigh reflectivity over a broad spectrum. It has been shown that HCG can replace a conventional DBR structure as an alternative solution for vertical cavity surface emitting laser (VCSEL) mirrors. We further demonstrated tunable VCSELs with a HCG as a movable reflector.

In this chapter, we present a completely new high-Q resonator configuration using the high contrast grating. In particular, the in-plane high-contrast grating is designed to form a high-Q resonator, as well as to couple light in the surface-normal direction. We present a design with the Q factor as high as 500,000 by using the finite difference-time-domain (FDTD) numerical simulation. Experimentally, we designed and fabricated HCG-resonator (HCG-R) structures on a wafer consisting of InGaAs quantum wells sandwiched between AlGaAs layers. In contrast with the typical 20 nm wide photoluminescence (PL) spectrum, a very narrow band of 0.07 nm is obtained with the HCG-R structure, the measurement of which is limited by our instrumentation. A very high Q factor of 14,000 is inferred from this data. A much higher Q is expected with an optimization of the fabrication and characterization systems. The unique feature of high-Q with surface-normal emission is highly desirable, as the unique topology facilitates

convenient and high output coupling with free-space or fiber optics. This feature is promising for array fabrication of lasers and filters, as well as high throughput sensor arrays.

5.2 Design

5.2.1 Device Design and Simulation

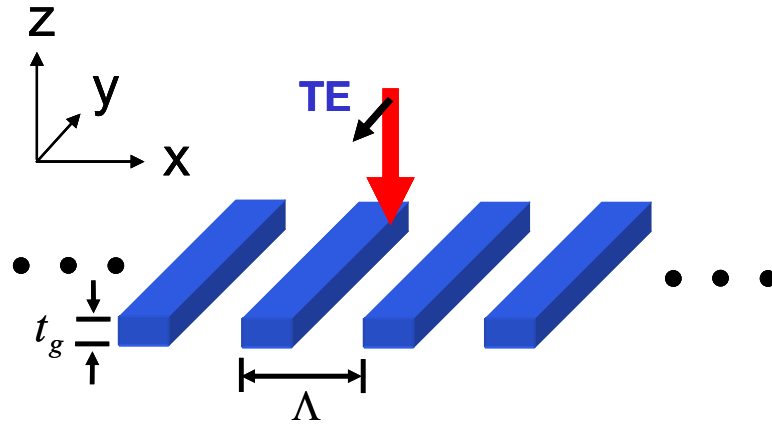


Figure 5.1 Schematic of a HCG structure with TE polarized light incident from surface normal direction.

The schematic of an infinite HCG structure is shown in Figure 5.1, with stripes that are periodic in the x direction and are infinite in both the x and y directions. The high-index material, which is freely suspended and fully surrounded by air as the low-index material, consists of $\text{Al}_{0.6}\text{Ga}_{0.4}\text{As}$ with three $\text{In}_{0.2}\text{Ga}_{0.8}\text{As}$ quantum wells embedded inside as an active material. The reflectivity spectrum of the resonator is calculated using Rigorous Coupled Wave Analysis (RCWA) for a normal-incident TE-polarized plane wave with its electric field parallel to the gratings, shown as blue circles in Figure 5.2. The grating is specified by three parameters: the period (Λ), thickness (t_g), and duty cycle (η). Choosing the appropriate parameters, we can obtain a reflectivity spectrum with a

sharp asymmetric line shape, and whose reflectivity varies from 0 to 1 over a very narrow wavelength range. In this case, $\Lambda= 484$ nm, $t_g= 390$ nm, and $\eta= 64\%$.

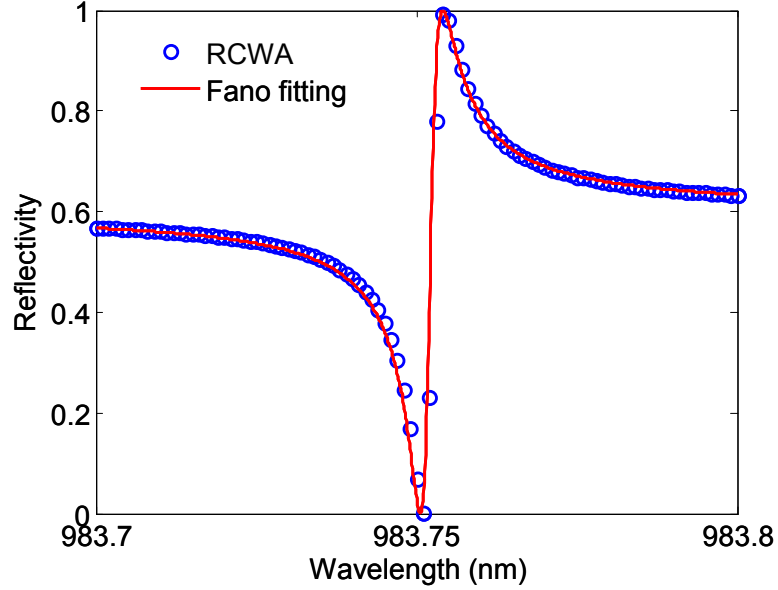


Figure 5.2 Simulated reflectivity spectrum of HCG grating using RCWA shown in blue circles. Red curve is the fitted Fano resonance line shape. Q factor is $\sim 500,000$.

This asymmetric resonance has been reported previously for photonic crystals and is referred to as Fano resonance [26]. It is the result of the interference between the normal incidence beam and the in-plane resonance of the HCG. The Q factor of the resonance can be extracted by fitting the simulated reflectivity spectrum with following Fano-resonance equation [26]:

$$R = \frac{r^2(\omega - \omega_0)^2 + t^2(1/\tau)^2 - 2rt(\omega - \omega_0)(1/\tau)}{(\omega - \omega_0)^2 + (1/\tau)^2} \quad (5.1)$$

where ω_0 and τ are the center frequency and the lifetime of the resonance, and r and t are the electric field reflectivity and transmittance of a uniform slab with the same thickness

as the HCG layer and with an effective dielectric constant. The Q factor of the resonance can be calculated using $Q = \omega_0 \tau$. The red curve in Figure 5.2 shows the fitted Fano-resonance curve based on equation 5.1. The extracted Q factor in this case is calculated to be $\sim 500,000$.

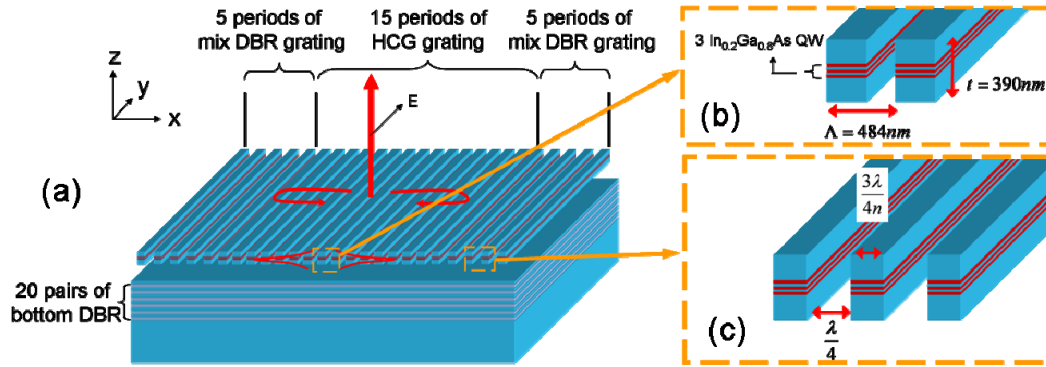


Figure 5.3 (a) Schematic of HCG high-Q resonator. (b) Schematic of middle HCG grating with three $\text{In}_{0.2}\text{Ga}_{0.8}\text{As}$ quantum wells embedded inside grating layer. (c) Schematic of side mix-DBR grating mirror which is a combination of 1st-order and 3rd-order DBR gratings.

For device applications, however, it is essential to consider a finite-sized HCG. To prevent light leakage from all four symmetric directions, i.e. $\pm x$ and $\pm z$, we considered a structure with distributed Bragg reflectors (DBRs) at the $\pm x$ ends and below the HCG, as shown in Figure 5.3. In this structure, the HCG grating consists of n -period gratings with three $\text{In}_{0.2}\text{Ga}_{0.8}\text{As}$ quantum wells sandwiched between $\text{Al}_{0.6}\text{Ga}_{0.4}\text{As}$ layers, as shown in Figure 5.3 (b), where n varies from 3 to 15. The end-DBRs are a combination of 1st-order DBR gratings and 3rd-order DBR gratings for ease of fabrication, as shown in Figure 5.3 (c). The air spacing has a width of $\lambda/4$ (1st-order), and the semiconductor strip width is $3\lambda/4$ (3rd-order). The bottom-DBR consists of 20 pairs of $\lambda/4$ -thick AlAs/GaAs layers grown on the substrate to reflect the $-z$ emission light.

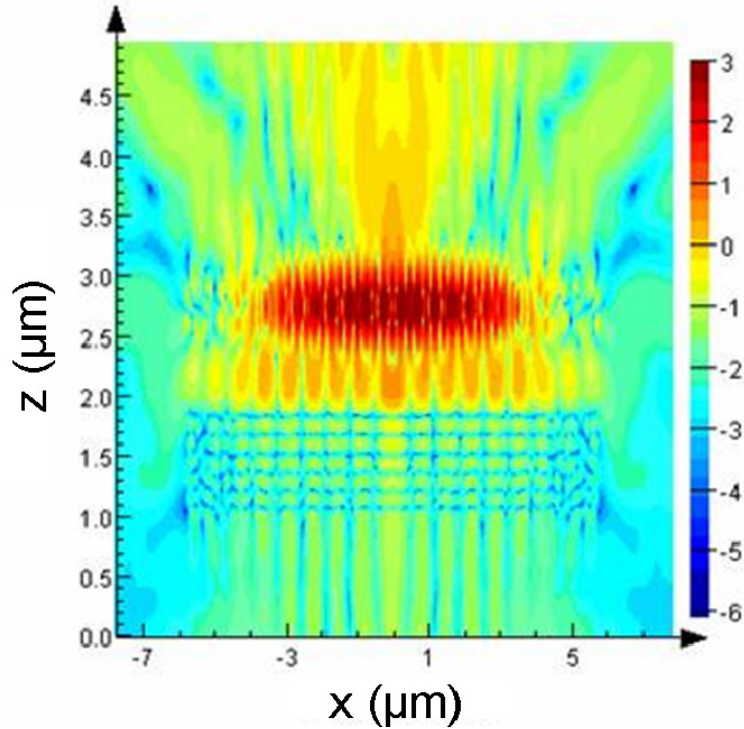


Figure 5.4 Simulated electric field intensity profile in the HCG resonator using finite-difference time-domain (FDTD) method. Color is labeled in log scale. Q is estimated to be 500,000.

Figure 5.4 shows the numerical simulation result of the field intensity profile in the HCG high-Q resonator using the finite-difference time-domain (FDTD) method. In the calculation, a TE-polarized (an electric field parallel with the grating) dipole source is excited in the center of the HCG resonator for a short period of time. After the dipole source is terminated, the electric field intensity profile of the resonator is monitored and recorded. The simulation shows that energy can be well-confined inside the HCG resonator, and that the output light only emits in the surface-normal direction. In this simulation, only 4 pairs of bottom DBR are used, instead of 20 pairs (used in experiment), to save the simulation time.

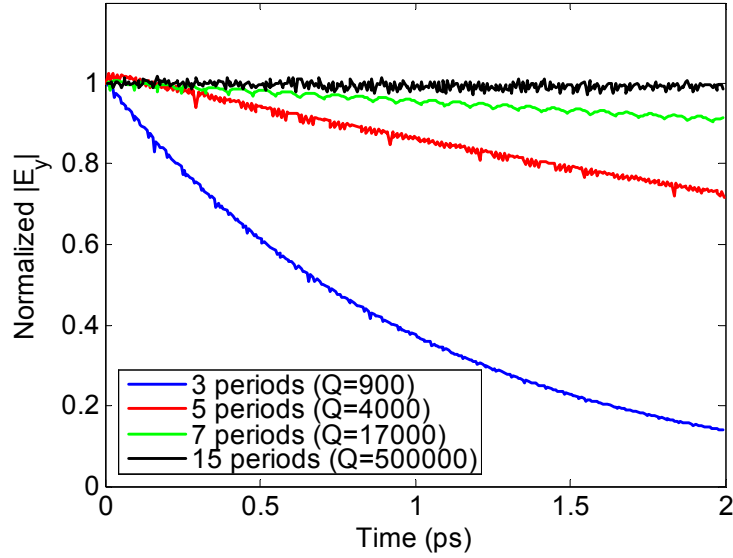


Figure 5.5 Normalized electrical field decay as a function of time in the HCG resonator for different number of HCG periods (3 periods, 5 periods, 7 periods and 15 periods). Q is estimated to be 900, 4000, 17000 and 500000 respectively.

Figure 5.5 shows the electric field intensity inside the resonator as a function of time after the excitation is turned off. Devices with different numbers of HCG periods are simulated. As shown in Figure 5.5, electric field intensity decays exponentially with time. Based on this decay rate, the Q factor of the resonance can be calculated can be calculated as the following equation:

$$Q = 2\pi f \frac{|E|^2}{\frac{d|E|^2}{dt}} \quad (5.2)$$

Using equation 5.2, for the devices with 3, 5, 7 and 15 periods of HCG, the Q factor is calculated to be 900, 4000, 17000 and 500,000 respectively. Figure 5.6 shows the simulated electric field intensity profiles in these HCG resonators.

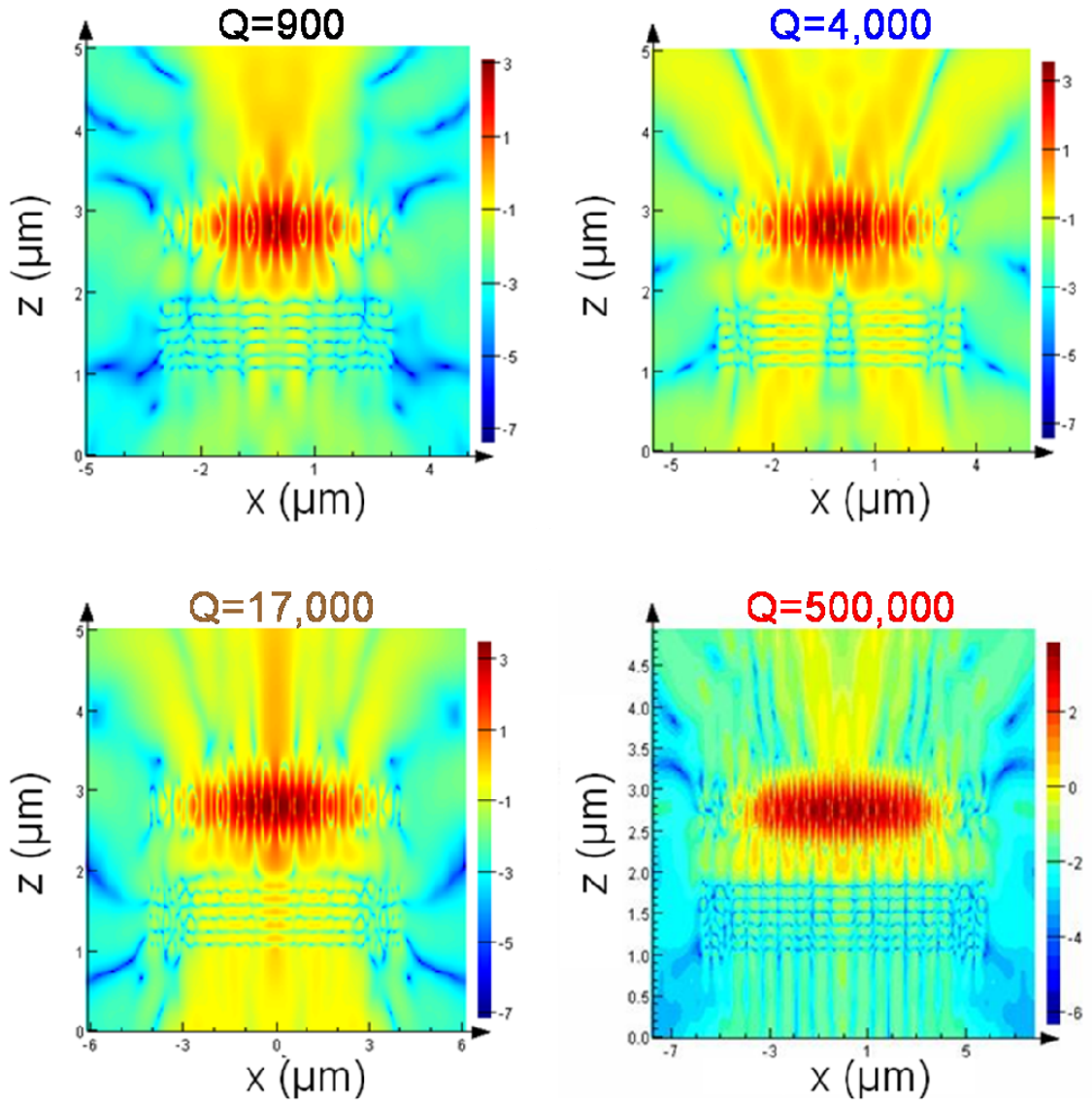


Figure 5.6 Simulated electric field intensity profiles in the HCG resonators with different number of HCG periods (3 periods, 5 periods, 7 periods and 15 periods). Q is estimated to be 900, 4000, 17000 and 500000 respectively.

Next, optical gain is incorporated into the $\text{In}_{0.2}\text{Ga}_{0.8}\text{As}$ quantum wells in the FDTD simulation. Assuming the grating material is lossless, the threshold gain required in the quantum well for lasing is as low as 30 cm^{-1} for the high-Q resonator design with 15 periods of HCG.

5.2.2 Sensitivity Study and Applications

We also studied the HCG resonant wavelength as a function of grating dimensions and refractive indices. It is interesting to note that the wavelength peak can be designed to be highly sensitive to the thickness of an extra layer deposited on the HCG, but that the wavelength and Q value are highly insensitive to the HCG index or temperature variations. These attributes make the HCG-R highly desirable for sensors and uncooled optoelectronic device applications.

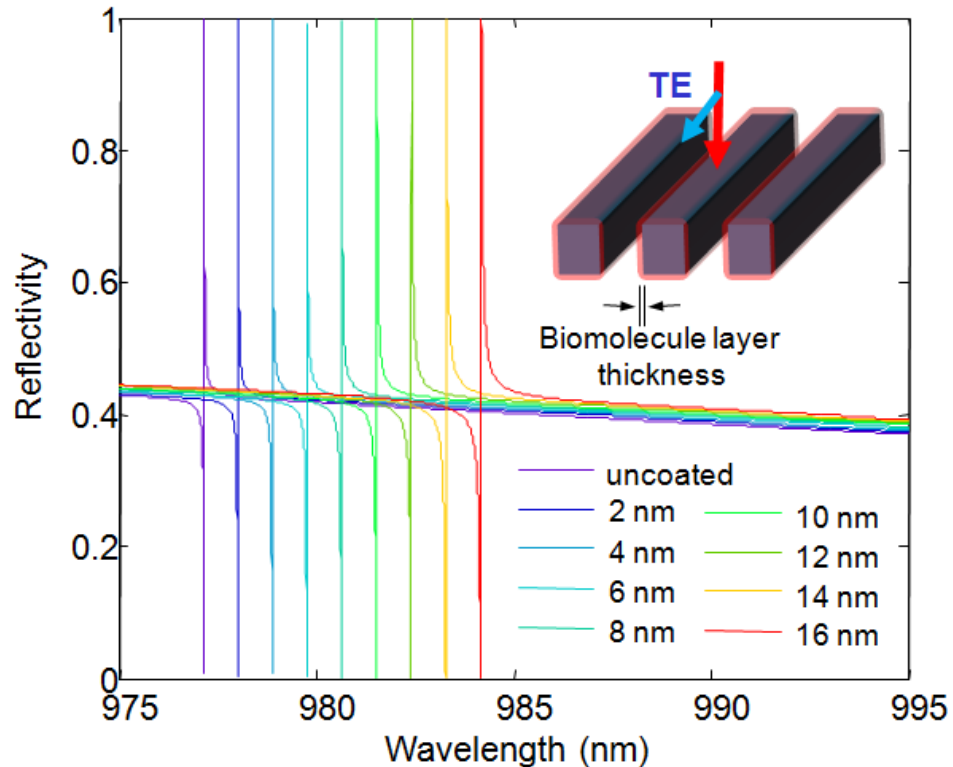


Figure 5.7 Simulation results for a HCG biosensor. The resonant wavelength red shift when biomolecule layers with different thicknesses are deposited onto the HCG structure.

The HCG we simulated had dimensions Λ , t_g , and η equal to 502 nm, 385 nm, and 64%, respectively. The refractive indices of the high and low index materials are 3.15 and

1, respectively. Figure 5.7 shows the calculated spectra of a HCG having various thickness of refractive index of 1.3 material deposited on it. The HCG wavelength increases greatly, at a rate of 0.44 nm/nm, with deposited material, which is significantly larger than the 0.27 nm/nm obtained for guided-mode resonator sensors [65]. This large sensitivity is due to the high index contrast of the HCG grating and a larger overlap of the optical field with the biomaterials, which can be wrapped around the gratings in an HCG-R. In addition, the linewidth remains small due to the high Q value. Both factors will contribute to a rapid and easy detection of small thickness changes.

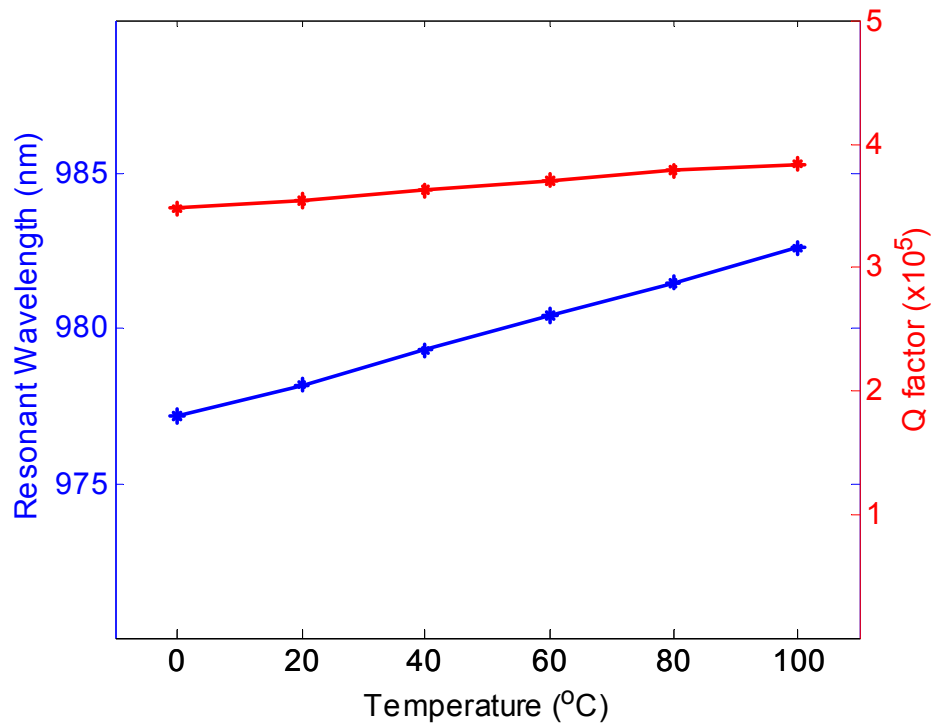
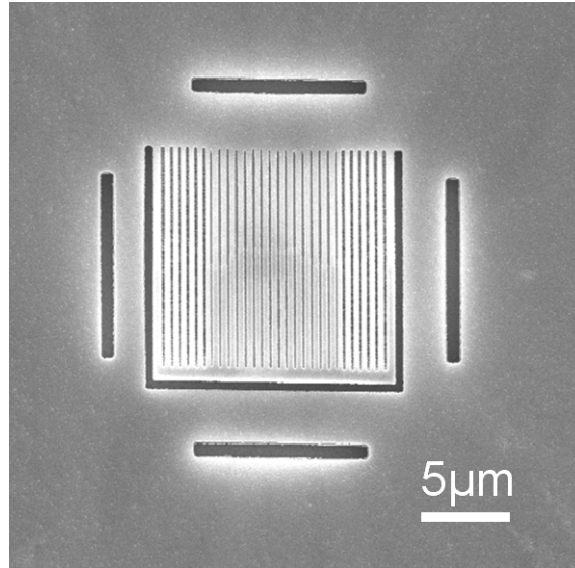


Figure 5.8 Simulation results for HCG resonant wavelength and Q factor as a function of temperature. Resonant wavelength only shifts 0.5 Å/K and the Q factor of the HCG cavity remains almost constant when temperature is changed from 0 °C to 100 °C.

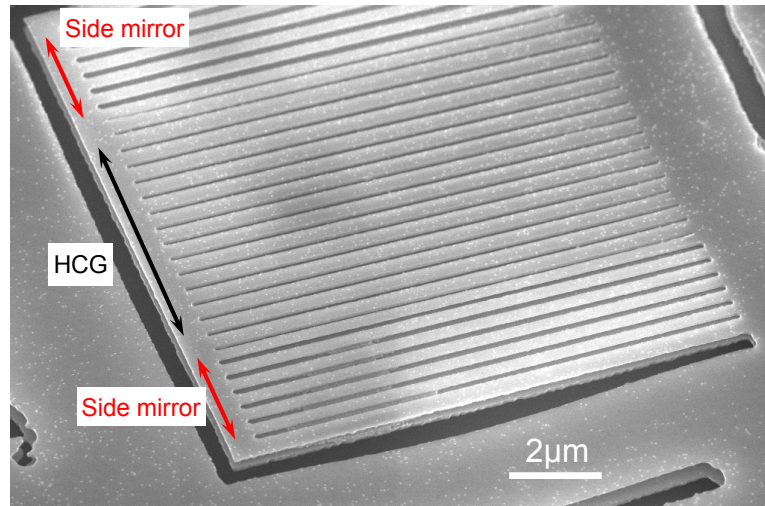
For applications such as lasers and filters, it is desirable for the resonant wavelength and Q value to be temperature insensitive. Figure 5.8 shows the simulation results for HCG resonant wavelength and Q factor as a function of temperature. The refractive index temperature dependence of the grating material is assumed to be $2 \times 10^{-4}/\text{K}$ [67]. Figure 4(b) shows that the HCG-based laser resonant wavelength shifts only $0.5 \text{ \AA}/\text{K}$, and that the Q factor of the HCG cavity remains almost constant when temperature is changed from $0 \text{ }^\circ\text{C}$ to $100 \text{ }^\circ\text{C}$. As a comparison, the emission wavelength shifts $1 \text{ \AA}/\text{K}$ in a DBR laser or VCSEL, and $3 \text{ \AA}/\text{K}$ for a Fabry-Perot laser. This improvement in the temperature stability mainly comes from the large index contrast with a low index material, whose refractive index does not change when temperature is changed.

5.3 Experiment

The proposed HCG high-Q resonator is experimentally demonstrated. The device was grown by metal organic chemical vapor deposition (MOCVD) on a GaAs substrate. The grating structure was patterned by electron-beam lithography on poly-methyl methacrylate (PMMA) photoresist and then etched by reactive ion etching (RIE). A wet chemical-based selective etching, followed by critical point drying, was used to remove the sacrificial material underneath the HCG layer and to form the freely suspended grating. Figure 5.9 (a) shows scanning electron microscopy (SEM) image of the top view of a fabricated HCG high-Q resonator. Figure 5.9 (b) shows the side view of the same device, with center HCG labeled in black and side mix-DBR mirror labeled in red.



(a)



(b)

Figure 5.9 SEM images of (a) the top view and (b) the side view of a fabricated HCG high-Q resonator.

Low-temperature (4K) photoluminescence (PL) was measured using a Ti:Sapphire laser at 800 nm wavelength. The emission spectrum of the wafer without the HCG-R structure is plotted in blue in Figure 5.10, showing a typical PL spectrum of the InGaAs quantum wells with a full-width half-maximum (FWHM) linewidth of 20 nm. The HCG

resonator emission is shown as the red curve in Figure 5.10. A very narrow PL emission linewidth is obtained. The inset shows the zoomed-in emission with a FWHM linewidth as narrow as 0.07 nm, which is limited by our spectrometer resolution. This translates to a Q factor as high as 14,000.

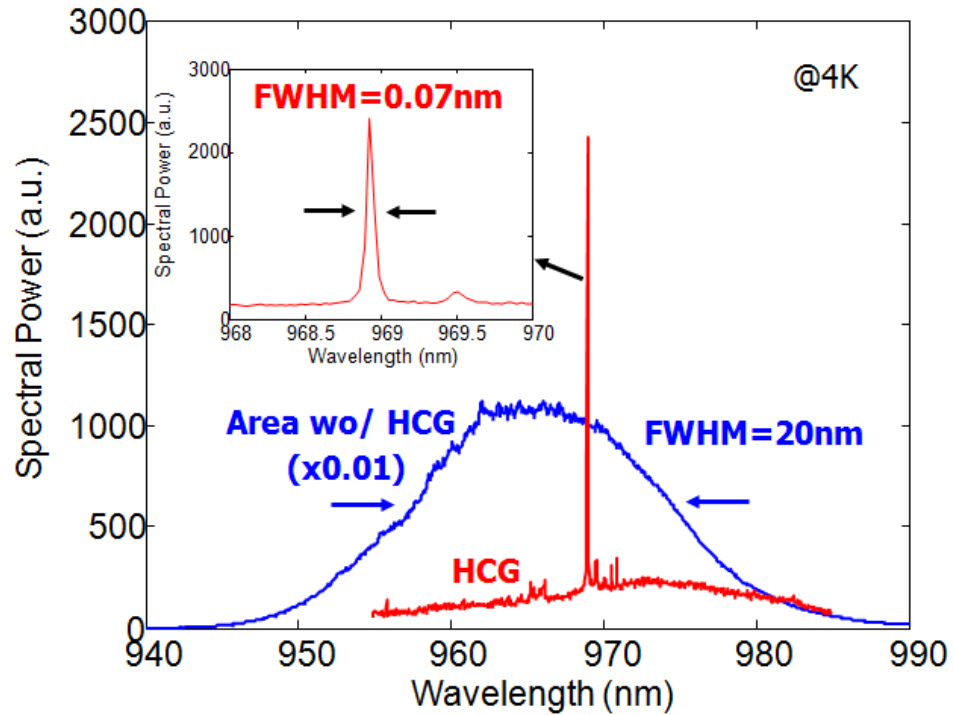


Figure 5.10 Emission spectrum of HCG resonator (in red) and emission spectrum in the area without grating (in blue). The inset shows a zoomed-in picture of the HCG emission spectrum. The FWHM of the HCG resonator emission peak is $\sim 0.07\text{nm}$ and Q is ~ 14000 .

Figure 5.11 shows the PL emission spectra under different pumping levels. With increasing pumping power, no further narrowing of the spectrum was observed, most likely due to our instrumental limitations. Future experiments will include measurements with improved resolution and time-resolved PL.

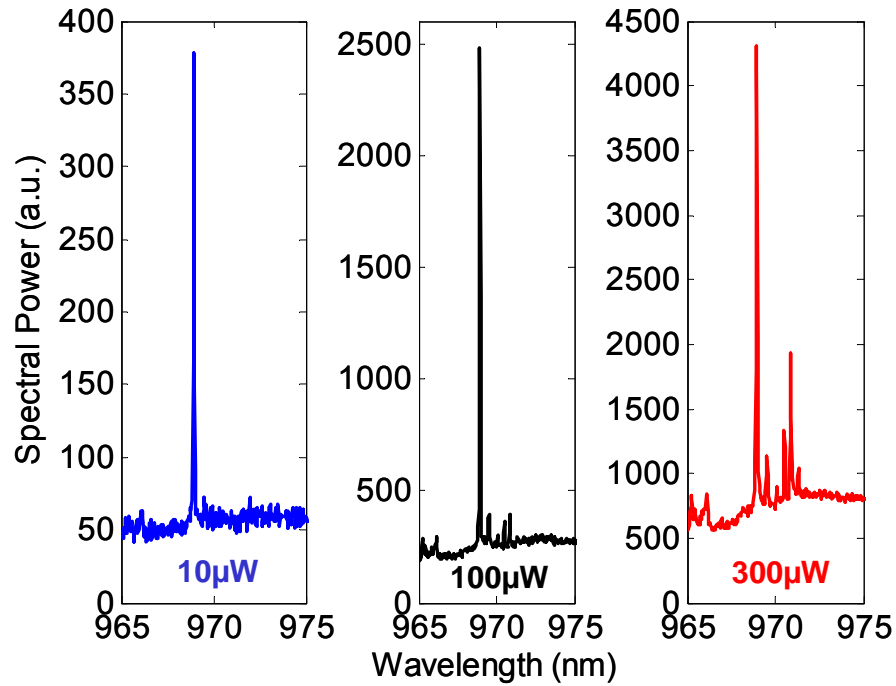


Figure 5.11 Emission spectra of HCG resonator under $10\mu\text{W}$, $100\mu\text{W}$, $300\mu\text{W}$ optical pumping, respectively.

5.4 Summary

We presented a high-Q resonator structure using a high contrast subwavelength grating for the first time. A Q factor of $\sim 500,000$ was obtained by numerical simulation. In addition, we demonstrated the very high sensitivity of the wavelength peak to the thickness of material coated on the HCG. This topology makes the device an excellent candidate for high throughput sensing of biological or chemical agents. The Q value and wavelength are insensitive to temperature variation, making them well suited for uncooled device applications. Finally, a Q value of 14,000 is experimentally demonstrated by the PL of an HCG-R, with the inclusion of an active quantum well region.

The HCG resonator proposed here has many desirable attributes that lend it to being an excellent platform for devices such as lasers, modulators, detectors, filters, and sensors. First, the epitaxial structure is very thin, which significantly relaxes the stringent requirements typically found in thick epitaxy (several microns) used for optoelectronic devices. Therefore, it may open the door for devices in a wavelength regime where epitaxy presents a major challenge. Secondly, the surface-normal emission facilitates simple and highly efficient output coupling for free-space or fiber optics. Finally, this structure facilitates scalability. By expanding the grating size, it is easy to increase the Q or tailor a designable passband for filters by the inclusion of sections of HCGs with different dimensions.

Chapter 6

HCG-based Low Loss Hollow-core Waveguide

6.1 Introduction

The ability to generate long optical delays with low intrinsic loss is useful for a wide range of applications, including optical signal processors, RF filtering, optical buffers, and optical sensing. Optical fibers have been used for these applications with advantages such as ultra-low loss, dispersion and nonlinearity, and an exceedingly large bandwidth. However, they are bulky, heavy, and lack manufacturing scalability. Lithographically defined, chip-scale waveguides have been reported in SiO₂/Si and III-V material systems. They are desirable because they are compact, light-weight, and can be integrated with other optoelectronic devices. The lowest reported loss achieved to date in chip-based waveguides is on the order of 1 dB/m [68], three to four orders of magnitude higher than that of optical fibers. This loss is unacceptably high for most applications requiring 0.01 dB/m. The fundamental reasons for the high losses are: direct band-edge absorption, free

carrier absorption, and absorption due to interaction with optical phonons [69]. In addition, these devices are expected to have high nonlinearity and dispersion.

Hollow-core waveguides (HW) are highly promising for achieving fiber-like ultra-low loss, nonlinearity and dispersion because of the elimination of the core material. There have been advances in hollow-core waveguides, ranging from waveguides using a metallic shell, to ones using distributed Bragg reflector (DBRs), to ones with photonic crystals (PhCs), etc [70-72]. The basic principle is to guide the optical beam propagating through the air by multiple reflections at the cladding mirrors. A hollow-core PhC optical fiber has shown an extremely low loss of ~ 0.001 dB/m [72]; however, the lowest loss for a chip-based hollow-core waveguide is still high, at ~ 10 dB/m using DBRs [71]. The major loss of the waveguide comes from the reflectivity of the cladding DBR mirrors not being high enough. Ultrahigh reflectivity is essential to achieve ultra-low loss hollow waveguides.

In this chapter, we propose a novel ultra-low loss, hollow-core waveguide structure using HCGs as the high reflectivity cladding to reflect light at a small glancing angle. We show that HCGs with periodicity parallel to the direction of propagation can confine light in the waveguide. Instead of causing the backward wave reflection normally expected of traditional periodic structures, the HCG forms a high reflectivity glancing incidence mirror for the guided wave. This is a totally unexplored concept in guided-wave optics: propagation parallel to the direction of periodicity of a periodic structure. We show a HCG hollow-core slab waveguide design with an exceedingly low propagation loss (< 0.01 dB/m), using both rigorous coupled wave analysis (RCWA) and

finite-difference time-domain (FDTD) numerical simulation. In addition, we show a potential 2D design with loss estimated to be less than 0.01 dB/m.

6.2 1D HCG Hollow-core Waveguide

6.2.1 Basic Principle

The schematic of a HCG structure is shown in Figure 6.1. High index gratings (blue) are surrounded by low index material, typically air or oxide. The gratings are typically made of semiconductors and have a high refractive index >3 . There are three physical parameters which control the reflectivity of the grating: period (Λ), thickness (t_g), and duty cycle (η). The thickness and period are subwavelength. The incident angle of the light, θ , is measured from the plane of the grating. In our previous chapters, we showed that when light is incident on the grating in surface-normal condition, i.e. $\theta=90^\circ$, the grating exhibits a very broadband high reflectivity. The unusually high broadband reflectivity arises from the high index contrast between the gratings and their surroundings. In addition, the period of the grating is sub-wavelength. No diffraction orders other than the zeroth are present.

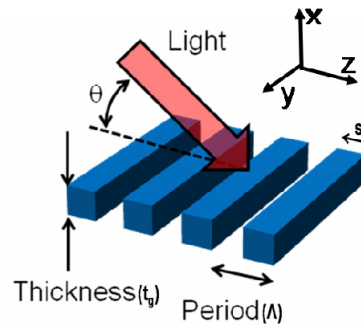


Figure 6.1 Schematic of high contrast grating (HCG). High index gratings (blue) are surrounded by low index material, typically air. The incident angle, θ , is measured from the plane of the grating.

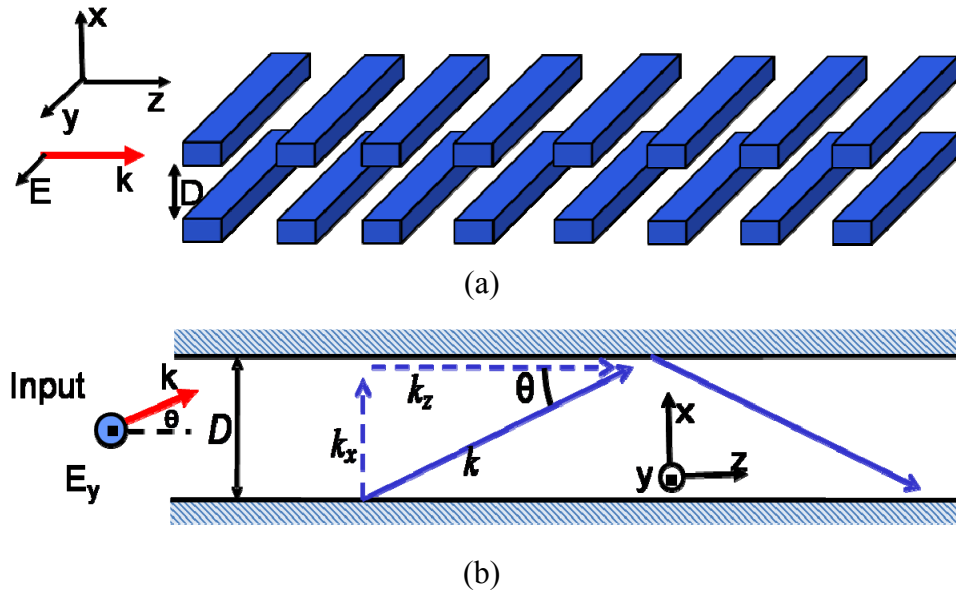


Figure 6.2 (a) Schematic of a 1D HCG hollow-core slab waveguide structure consisting of two reflecting HCGs. (b) Ray optics model for guided mode in a hollow-core slab waveguide. Two reflective surfaces extend infinitely in the y - z plane and light propagates in the z direction. The spacing D between the planes forms the core of the waveguide. Light within the core can be expressed via a plane wave expansion, where the plane waves within the core are characterized by the wave vector k .

In this work, we use HCG as a hollow-core waveguide cladding with extremely high reflectivity. The schematic of a 1D HCG-HW slab waveguide structure is shown in Figure 6.2 (a). It consists of two reflecting HCGs that are periodic in the z direction and infinite in y directions. The two HCGs are spaced a distance D apart. In this study, we consider the input light is launched in z direction with TE polarization (electric field parallel with the grating fingers). Light in the core of the waveguide can be expanded into a series of plane waves bouncing between the reflecting HCG planes at different angles. Due to the high reflectivity of the HCG, a simple ray-optics model may be used to

estimate the propagation properties of the HCG-HW as shown in Figure 6.2 (b). A ray which propagates through a HW of size D at angle θ travels a distance $D/\tan\theta$ per bounce. At each bounce, there is a loss of $\delta=1-R$, where R is the reflectivity of the HCG at angle θ . Assuming there is no material loss in the hollow waveguide core (air), the optical propagation loss per unit length over a distance L is

$$\alpha(dB/m) = -\frac{10}{L} \log\left(\frac{P_t}{P_i}\right) = -\frac{10}{L} \log(R^N) = -\frac{10}{L} N \log(R) = -10 \frac{\tan\theta}{D} \log(R) \quad (6.1)$$

where N is the number of bounces in distance L and $N = L \tan\theta / D$.

Given that, $\delta \ll 1$, $\log(R) = \frac{\ln(1-\delta)}{\ln 10} \approx -0.43\delta$ and $\theta \ll 1$, $\tan\theta \approx \theta$, therefore the waveguide loss can be estimated as

$$\alpha(dB/m) \cong 4.3 \frac{\theta}{D} \delta \quad (6.2)$$

For a propagating mode, the round-trip phase shift incurred by the wave from crossing the waveguide in the transverse direction, is a multiple of 2π . A discrete set of angles satisfies this condition and forms the modes of the waveguide. Provided that there is no significant phase shift associated with the reflections, the modal angles are

$$k_x D = \frac{2\pi}{\lambda} \sin\theta \cdot D = m\pi; m = 1, 2, \dots \quad (6.3)$$

Thus the modes of a HW are determined only by D . Each mode can be described in terms of its characteristic angle θ . For small θ and large D , $\theta \cong \sin\theta = m\lambda / 2D$ and the propagating loss is inversely proportional to the square of D .

6.2.2 Design and Simulation

Rigorous coupled wave analysis (RCWA) is used to obtain the HCG reflectivity spectra at different incident angle θ , and loss is calculated using equation 6.1. Figure 6.3 (a) shows a waveguide loss contour plot (dB/m) vs. HCG parameters Λ and s , for a HW with a core size D of 15 μm (corresponding to $\theta=3^\circ$) at $\lambda = 1.55 \mu\text{m}$ with t_g fixed at 410 nm. The loss of 0.1dB/m and 0.01dB/m are shown by the black and white contours, respectively. Figure 6.3 (b) shows loss contour plot vs. t_g and s for the case when Λ is fixed at 665 nm. Once again the loss of 0.1dB/m and 0.01dB/m are shown by the black and white contours, respectively. These figures show reasonable tolerance of variations is obtained to accommodate fabrication imperfection.

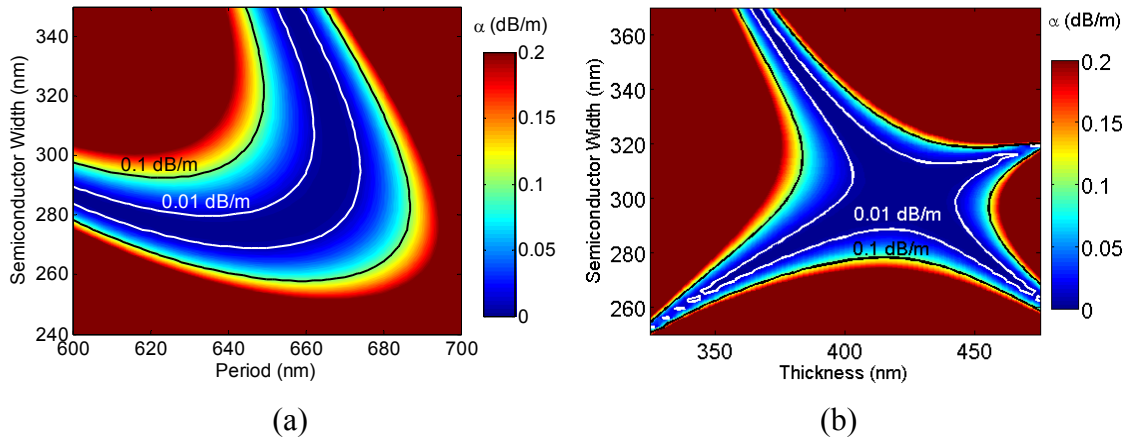


Figure 6.3 Calculation of waveguide loss α (dB/m) at 1.55 μm for a 15- μm core slab HCG-HW as a function of (a) grating period and semiconductor width (b) thickness and semiconductor width. 0.1dB/m and 0.01dB/m lines are labeled in the plots.

One fascinating aspect of HCG is the ability to design a large spectral width despite the stringent reflectivity requirement. The following grating parameters are used to achieve a broad spectral width: $\Lambda = 730 \text{ nm}$, $t_g = 1.04 \mu\text{m}$, $\eta = 65\%$, high index grating $n=3.6$ and low index air $n=1$. Figure 6.4 shows the fundamental mode propagation loss of a

15 μm core HCG-HW as a function of wavelength. Large spectral widths of 130 nm and 80 nm can be achieved for loss requirements of 0.1dB/m and 0.01dB/m, respectively.

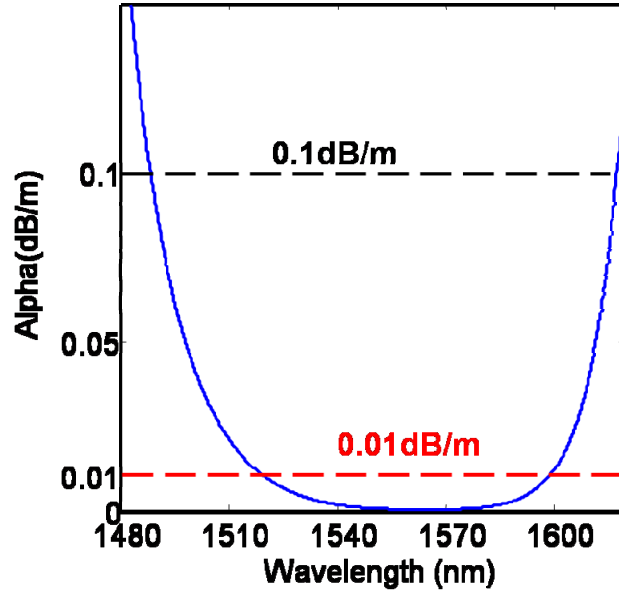


Figure 6.4 Calculation of waveguide loss α (dB/m) at 1.55 μm for a 15- μm core slab HCG-HW as a function of wavelength. 0.1dB/m and 0.01dB/m lines are labeled in the plots.

As the HW loss is inversely proportional to D^2 , it is desirable to design a large core waveguide. However, a large D leads to a large number of modes, which may be detrimental. The HCG-HW offers a unique advantage: simultaneously having a large core and maintaining a single polarization and transverse mode. This is because of the HCG reflectivity angular and polarization dependence, thus we can design the HCG to yield higher loss for larger θ , i.e. higher order modes, such that they are preferentially filtered out. Figure 6.5 plots α vs. incident angle for $D=15\mu\text{m}$, with the first four modes marked on the curve. The loss for the fundamental mode is as low as 0.0026dB/m. The 2nd order mode loss is also rather low at 0.057dB/m. However, choosing launching conditions with

symmetric transverse field components would excite only the odd order modes, so that the next mode is the 3rd mode, whose loss is 200 times higher than that of the 1st mode. With this angular loss dependence, HCG-HW can simultaneously achieve low loss for the fundamental mode and high suppression towards higher order modes.

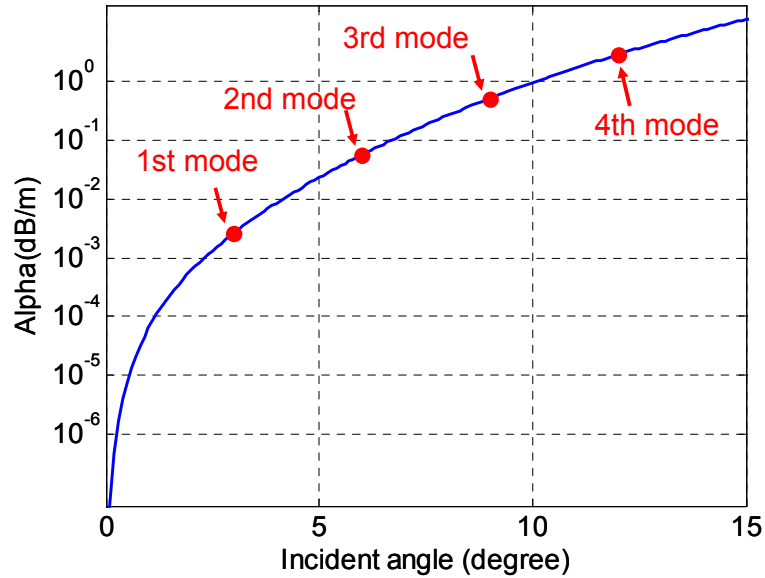


Figure 6.5 Propagation loss of 1D slab HCG-HW vs θ for the first four TE modes in a 15 μm HCG-HW. Due to symmetry, one can avoid launching into the second order mode. Hence the difference between the first and third order modes is the most important for modal screening. In this case, the loss of 3rd mode (2nd lowest odd order mode) is drastically higher, 200 times, than that of the 1st mode.

Next, finite-difference time-domain (FDTD) numerical simulation is used to calculate the propagation loss of the HCG-HW. Figure 6.6 shows the 2D electric field intensity profile of a HCG-HW with a 15 μm core size along the propagation direction. In this simulation, TE-polarized light with a mode profile matching the fundamental mode is launched into a 2 mm long HCG-HW. The spectrum width of the launched light is about 4 nm. As shown in Figure 6.6, the light intensity is guided inside the hollow core, and the

field intensity outside the HCG-HW is only 10^{-8} of the intensity at the center of the hollow core. This agrees with the $\delta \sim 10^{-8}$ result which is obtained by using RCWA.

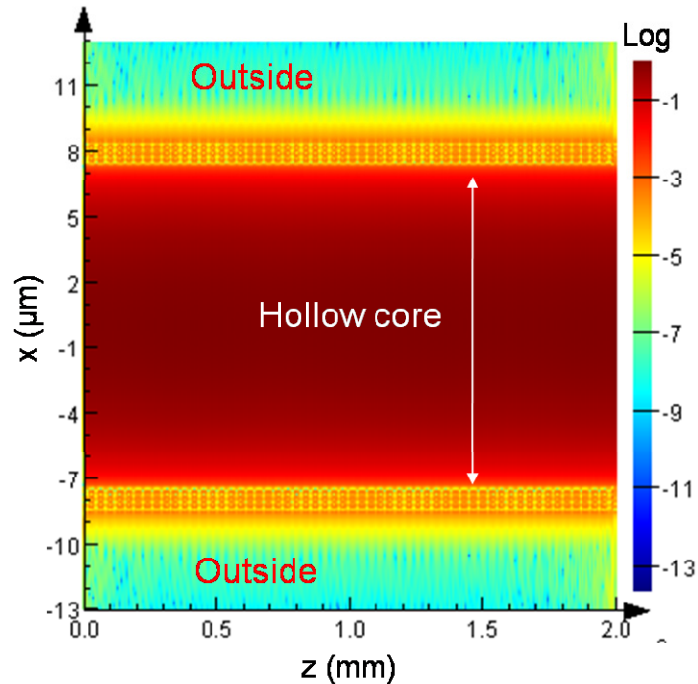


Figure 6.6 Simulated electric field intensity profile of HCG-HW. Color is labeled in log scale. The field intensity outside the HCG-HW is only 10^{-8} of the intensity at the center of the hollow core.

Due to simulation boundary conditions and the abrupt cutoff of the HCG walls at the start and end of the waveguide, only the middle 0.8 mm is used for calculating the waveguide propagation loss. Figure 6.7 shows the normalized E_y intensity at the center of the hollow core as a function of waveguide length z . Since we are looking for a less than 10^{-5} intensity drop over the waveguide length, high frequency noises from the simulation are removed from the data and linear regression is used to extract the loss from the data, as plotted in the red dash line in Figure 6.7. A waveguide propagation loss of $0.006 \pm 0.0024 \text{ dB/m}$ with 95% fitting confidence bounds is obtained. Currently the 2 mm

simulated waveguide length is limited by our computational power. A more accurate loss number can be achieved by simulating longer waveguide length.

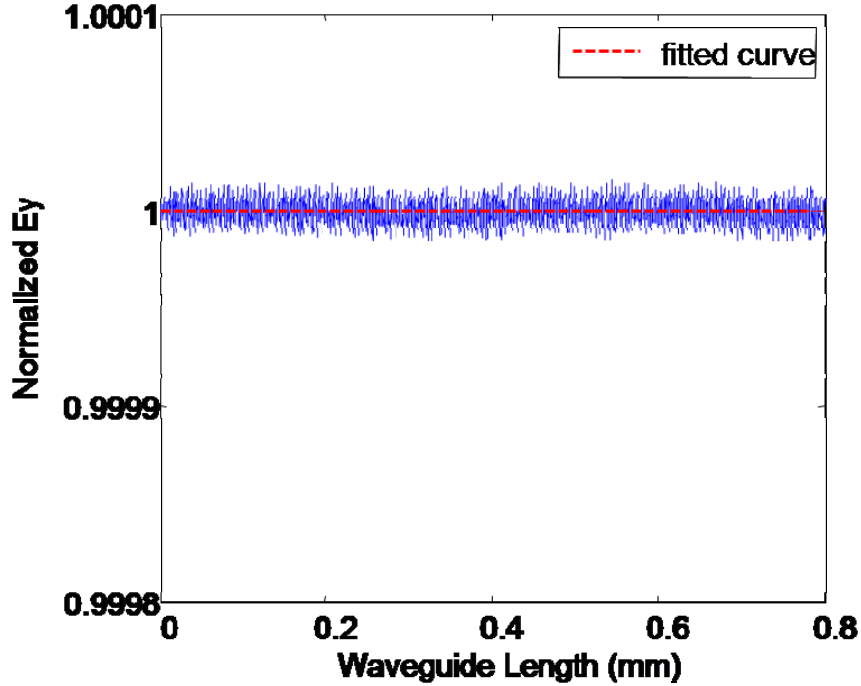


Figure 6.7 Normalized electrical field inside HCG-HW as a function of waveguide length. Linear regression is used to fit the curve as plotted in the red dash line. A waveguide propagation loss of $0.006 \pm 0.0024 \text{ dB/m}$ with 95% fitting confidence bounds is obtained.

While other highly reflective structures, such as DBR or PhC, require multiple layers to achieve a high reflectivity, the HCG structure can achieve a very high light confinement in a HW by using a single layer of cladding grating. Because of this, the field penetration depth in a HCG-HW cladding is significantly reduced compared to DBR or PhC based HW. In addition, as shown in the FDTD simulation results, the field intensity inside grating is very low, only 10^{-4} to 10^{-3} of the intensity at the center of the waveguide core. Using the field profile data from FDTD simulation, we integrate the total field energy inside the hollow-core as well as the total energy inside the HCG

cladding layer. The result we get shows that the energy inside HCG layers is only 10^{-7} to 10^{-6} of the total energy inside waveguide core, a much lower number than the ones in other HW structures.

For a fabricated waveguide structure, it has been long recognized that the scattering loss from interference roughness and fabrication imperfection can degrade the waveguide performance and introduce scattering loss. Scattering loss is can be estimated using Reyleigh scattering cross-section as $\alpha(dB/m) = 4.3(S_{inc}/P_{tot})\sigma_R\rho_S$, where S_{inc} is the incident Poynting vector at the vicinity of the scattering centers, P_{tot} is the total power carried through the waveguide and ρ_S is the surface density of the scattering centers, and σ_R is the Rayleigh scattering cross-section. The scattering loss for HCG-HW is expected to be very low because the power near and inside the reflecting HCG is almost zero (only 10^{-7} to 10^{-6} of the total power), which means that S_{inc} is extremely small. In addition, the small penetration depth of HCG also provides less chance for scattering centers on HCG surface to interact with the field, which also results in a lower scattering loss.

6.2.3 Nonlinearity

In data communication, nonlinearity can severely degrade signals in both analog and digital system-level applications of low loss waveguides. HCG-HW can significantly reduce nonlinear effects in data transmission, since the optical power is tightly confined in “linear” air, which means that a very small fraction of the optical field interacts with the grating material. From FDTD simulation results, the field intensity located in the high-index solid region is only 10^{-7} to 10^{-6} of the intensity in the core of the waveguide. Therefore, we estimate that the overall reduction in the effective nonlinear coefficient per

unit length is $\sim 10^6$ to 10^7 lower than in regular silicon waveguides, which means the HCG-HW can handle a higher power over a longer distance, thereby dramatically increasing the overall system performance.

6.2.4 Dispersion

The dispersion of a waveguide consists of material dispersion and waveguide dispersion. For a chip-scale silicon waveguide, the dispersion is dominated by the material dispersion, which is as high as 1000 ps/nm/km [73]. However, for HCG-HW, from the FDTD simulation result, the field intensity located in the high-index silicon region is only 10^{-7} to 10^{-6} of the intensity in the core of the waveguide. Therefore, the material dispersion contribution is less than 10^{-3} ps/nm/km, which can be ignored. The waveguide dispersion relationship of the HCG-HW can be estimated by ray optics. For the fundamental mode:

$$k_z = \frac{2\pi}{\lambda} \sqrt{1 - \left(\frac{\lambda}{2D}\right)^2} \quad (6.4)$$

Group velocity can be calculated as:

$$v_g = c \sqrt{1 - \left(\frac{\lambda}{2D}\right)^2} \quad (6.5)$$

where c is the speed of light in vacuum. Based on equation 6.5, the dispersion parameter d can be calculated:

$$d = \frac{d}{d\lambda} \left(\frac{1}{v_g} \right) = \frac{\lambda}{4D^2 c} \left(1 - \left(\frac{\lambda}{2D}\right)^2 \right)^{-\frac{3}{2}} \quad (6.6)$$

Our calculation shows that for the fundamental mode of the HCG-HW, the dispersion parameter d equals 5.8 ps/nm/km at 1.55 μm for $D=15 \mu\text{m}$. This dispersion number indicates that the proposed HCG-HW can support a >2 THz RF modulation over a length of 5 m [74].

6.2.5 Temperature Variation

For optical delay line application, temperature variations will lead to index changes in conventional waveguides, and hence result in degradation of delay phase precision. Given that the optical field penetration into the HCG is only 10^{-7} to 10^{-6} , the HCG-HW will be highly robust against temperature variation. Assuming a typical index change coefficient of 10^{-4} per degree in the semiconductor part of HCG, a change of 80°C over 150 m would translate into 50 fs time delay precision or 0.05% of 2π in phase shift for a 10 GHz signal, an extremely high 10^{-8} / $^\circ\text{C}$ total phase delay precision.

6.3 2D HCG Hollow-core Waveguide

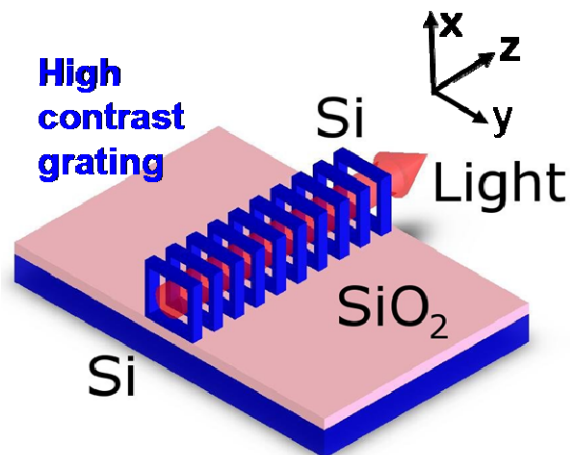


Figure 6.8 Schematic of a 2D rectangular HCG-HW.

2D confined HCG-HW can be designed using a rectangular waveguide structure as shown in Figure 6.8. RCWA and ray optics are used to optimize the dimensions of the HCG cladding, as shown in Figure 6.9. Compared to just one characteristic angle in the 1D HCG-HW, 2D HCG-HW cladding grating has two incident characteristic angles, θ and φ , which are the angle between incident beam and y - z plane and the angle between incident beam and x - z plane, respectively. For specific θ and φ , high reflectivity can be obtained by optimizing the grating dimensions.

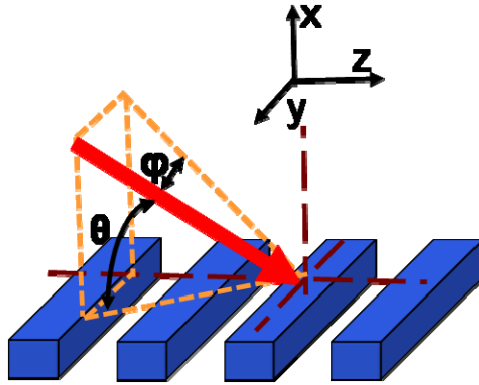


Figure 6.9 Schematic of HCG cladding grating in 2D rectangular HCG-HW. There are two incident characteristic angles θ and φ , which are the angle between incident beam and y - z plane and the angle between incident beam and x - z plane, respectively.

Figure 6.10 shows a round trip ray trace looking along the z axis direction.

$$k_x = k \sin \theta = 2\pi \sin \theta / \lambda, \quad k_x D_x = m\pi; m = 1, 2, \dots \quad (6.7)$$

$$k_y = k \sin \varphi = 2\pi \sin \varphi / \lambda, \quad k_y D_y = n\pi; n = 1, 2, \dots \quad (6.8)$$

where (m, n) are mode numbers. Similar to the method used in 1D HCG-HW loss calculation, we can use ray optics and RCWA simulation to estimate the loss of 2D rectangular HW-HCG for a different mode (m, n) . This mode is quite similar in its “threading through” waveguide nature to the HE modes in fiber. To achieve high

reflectivity with all 4 cladding gratings, the dimensions of the top and bottom HCGs are designed to be different from those of the left and right HCGs. For top HCGs, $\Lambda = 674$ nm, $t_g = 460$ nm and $\eta = 46\%$. The bottom HCG sits on $2.5 \mu\text{m}$ SiO_2 and its dimensions are $\Lambda = 570$ nm, $t_g = 390$ nm and $\eta = 46\%$, whereas for left and right HCGs, $\Lambda = 622$ nm, $t_g = 782$ nm, $\eta = 80\%$. This structure only supports the low loss propagation for one mode and one polarization, in this case, HE (1,1) mode where the majority of E-field components are along y direction. For a $25\mu\text{m}$ by $25\mu\text{m}$ hollow-core waveguide with these HCG claddings, we estimate that the loss of the fundamental mode (1,1) is 0.009 dB/m. Further optimization of the 2D confined HCG-HW design with even lower loss is still under investigation.

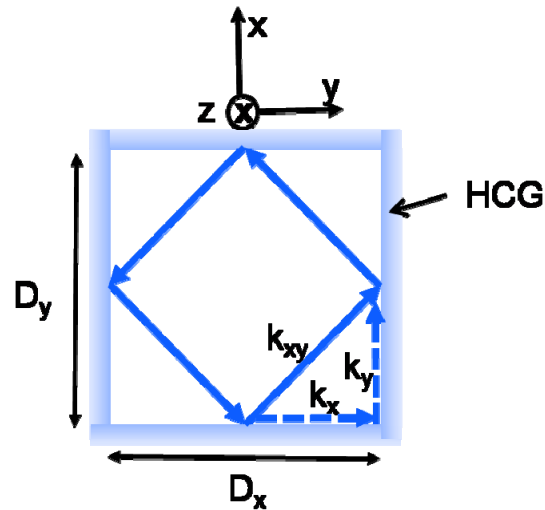


Figure 6.10 A round trip ray trace looking along the z axis direction. The sizes of the hollow-core in x and y direction are D_x and D_y , respectively.

6.4 Summary

We presented an ultra-low loss hollow waveguide structure using high contrast subwavelength grating. A waveguide propagation loss less than 0.01dB/m was obtained

by both rigorous coupled wave analysis and finite-difference time-domain numerical simulation. This loss value is three orders of magnitude lower than the lowest loss in the current chip-scale hollow waveguides. We also showed examples of HCG-HW designs with an extremely broad bandwidth ($\sim 100\text{nm}$) and a large fabrication tolerance. In addition, due to the unique angular and polarization dependence of the HCG reflection spectrum, HCG-HW enables single-mode operation with a core that is one order of magnitude larger than conventional waveguides. Finally, HCG-HW can significantly reduce nonlinear effects and dispersion in data transmission, and it is insensitive to temperature variation. With all these desirable attributes, HCG-HW can be an ideal candidate for on-chip optical communication, compact low loss optical delay lines, and interferometric sensors.

Chapter 7 Conclusion

In this dissertation, we presented a novel single-layer subwavelength high-index-contrast grating (HCG). HCGs can serve as surface normal broadband ($\Delta\lambda/\lambda \sim 35\%$), high-reflectivity (>99%) mirrors, which can be used to replace conventional distributed Bragg reflectors (DBRs) in optical devices. Different designs of HCGs can also serve as narrow band, surface emitting, high-quality (Q) factor optical resonators or shallow angle reflectors. We reviewed the recent advances in high-index-contrast grating and its applications in optoelectronic devices, including vertical-cavity surface-emitting lasers (VCSELs), high-Q optical resonators, and hollow-core waveguides.

We first presented a novel HCG-based VCSEL where the conventional DBR mirror is replaced with a HCG-based mirror. A systematic and comprehensive review of the experimental and numerical simulation results was presented to demonstrate many desirable attributes of HCG-based VCSELs, including polarization selection, transverse mode control, and a large fabrication tolerance.

Next, we presented an ultra-fast tuning, HCG-based tunable VCSEL. By integrating a mechanically movable actuator with a single-layer HCG as the VCSEL top mirror, precise, wide, continuous wavelength tuning (~ 18 nm) was achieved at room temperature. The small footprint of the HCG enables each of the mechanical actuator dimensions to be scaled down by at least a factor of 10, resulting in a greater than 1000 times reduction in mass, and an increase in the mechanical resonant frequency. It also allows for a record-fast, HCG-based tunable VCSEL with a tuning time in the ~ 10 ns range to be obtained.

Besides the HCG-based VCSELs/tunable VCSELs, we also presented a HCG-based surface normal high-Q resonator with a simulated Q-factor as large as 500,000 and an experimentally measured Q-factor of $\sim 14,000$. The unique feature of a high-Q with surface normal emission is highly desirable, as the topology facilitates a convenient and high output coupling with free-space or fiber optics. This feature is promising for array fabrication of lasers and filters, as well as high throughput sensor arrays.

In addition, we proposed a HCG-based hollow-core waveguide design with an ultralow propagation loss of < 0.01 dB/m, three orders of magnitude lower than the lowest loss of the state-of-art chip-scale hollow waveguides. This novel HCG hollow-core waveguide design will serve as a basic building block in many chip-scale integrated photonic circuits, enabling system-level applications including optical interconnects, optical delay lines, and optical sensors.

BIBLIOGRAPHY

- [1] D. Rittenhouse, "Explanation of an optical deception," *Trans. Amer. Phil. Soc.*, vol. 2, pp.37-42, 1786.
- [2] J. Fruanhofer, "Kurtzer Bericht von den Resultaten neuerer Versuche óber die Seseetze des lichtet, und die Theorie derselbem," *Ann. D. Phys.*, vol. 74, pp. 337-378, 1823.
- [3] M. C. Hutley, *Diffraction gratings*, Academic Press, 1982.
- [4] H. Rowland, "Preliminary notice of results accomplished on the manufacture and theory of gratings for optical purposes," *Phil. Mag. Suppl.*, vol. 13, pp. 469-474, 1882.
- [5] O.M. Lord Rayleigh, "On the dynamical theory of gratings," *Proc. Royal Soc. (London), Ser. A*, vol. 79, pp. 399-416, 1907.
- [6] M. Nevière, G. Cerutti-Maori, and M. Cadllhac, "Sur une nouvelle méthode de resolution du problème de la diffraction dune onde plane par un réseau infiniment conducteur," *Opt. Commun.*, vol. 3, pp. 48-52, 1971.
- [7] M. Nevière, P. Vincent, and R. Petit, "Sur la théorie du réseau conducteur et ses applications a l'optique," *Nouv. Rev. Opt.*, vol. 5, pp. 65-77, 1974.
- [8] M. G. Moharam and T. K. Gaylord, "Rigorous coupled-wave analysis of planar-grating diffraction," *J. Opt. Soc. Am.*, vol.71, pp. 811-818, 1981.
- [9] M. G. Moharam and T. K. Gaylord, "Rigorous coupled-wave analysis of dielectric surface-relief gratings," *J. Opt. Soc. Am.*, vol. 72, pp. 1385-1392, 1982.
- [10] C. Botten, M. S. Craig, R. C. McPhedran, J. L. Adams, and J. R. Andrewartha, "The dielectric lamellar diffraction grating," *Opt. Acta*, vol. 28, pp. 413-428, 1981.
- [11] C. Botten, M. S. Craig, R. C. McPhedran, J. L. Adams, and J. R. Andrewartha, "The finitely conducting lamellar diffraction grating," *Opt. Acta*, vol.28, pp. 1087-1102, 1981.
- [12] D. Maystre, "Sur la diffraction dune onde plane par un réseau métallique de conductivité finie," *Opt. Commun.*, vol. 6, pp. 50-54, 1972.
- [13] D. Maystre, "A new general integral theory for dielectric coated gratings," *J. Opt. Soc. Am.*, vol. 68, pp. 490-495, 1978.

- [14] J. Chandezon, D. Maystre, G. Raoult, "A new theoretical method for diffraction gratings and its numerical application," *J. Optics (Paris)*, vol. 11, pp. 235-241, 1980.
- [15] J. Chandezon, M.T. Dupuis, G. Cornet, and D. Maystre, "Multicoated gratings: A differential formalism applicable in the entire optical region," *J. Opt. Soc. Am.*, vol. 72, pp. 839-846, 1982.
- [16] L. Zhuang, S. Schablitsky, R. C. Shi, and S. Y. Chou, "Fabrication and performance of thin amorphous Si subwavelength transmission grating for controlling vertical cavity surface emitting laser polarization," *J. Vac. Sci. Technol. B*, Vol. 14, pp. 4055-4057, 1996.
- [17] S. Goeman, S. Boons, B. Dhoedt, K. Vandeputte, K. Caekebeke, P. V. Daele, and R. Baets, "First demonstration of highly reflective and highly polarization selective diffraction gratings (GIRO-gratings) for long-wavelength VCSELs," *IEEE Photon. Tech. Lett.*, vol. 10, pp. 1205-1207, 1998.
- [18] A. Haglund, S. J. Gustavsson, J. Vukusic, P. Jedrasik, A. Larsson, "High-power fundamental-mode and polarisation stabilised VCSELs using sub-wavelength surface grating," *Electron. Lett.*, vol. 41, pp. 805- 807, 2005.
- [19] C. F. R. Mateus, M. C. Y. Huang, D. Yunfei, A. R. Neureuther, and C. J. Chang-Hasnain, "Ultrabroadband mirror using low-index cladded subwavelength grating," *IEEE Photon. Technol. Lett.*, vol. 16, pp. 518-520, 2004.
- [20] K. Yee, "Numerical solution of initial boundary value problems involving maxwell's equations in isotropic media," *IEEE Transactions on Antennas and Propagation*, vol. 14, pp. 302-307, 1988.
- [21] K. S. Kunz and R. J. Luebbers, *The Finite Difference Time Domain Method for Electromagnetics*. Boca Raton: CRC Press, 1993.
- [22] C. F. R. Mateus, M. C. Y. Huang, C. Lu, C. J. Chang-Hasnain, and Y. Suzuki, "Broad-band mirror (1.12-1.62 μm) using a subwavelength grating," *IEEE Photon. Technol. Lett.*, vol. 16, pp. 1676-1678, 2004.
- [23] F. Koyama, H. Uenohara, T. Sakaguchi, and K. Iga, "GaAlAs/GaAs MOCVD growth for surface emitting laser," *Japanese Journal of Applied Physics, Part 1 (Regular Papers & Short Notes)*, vol. 26, pp. 1077-81, 1987.
- [24] T. Sakaguchi, F. Koyama, and K. Iga, "Vertical cavity surface-emitting laser with an AlGaAs/AlAs Bragg reflector," *Electronics Letters*, vol. 24, pp. 928-9, 1988.
- [25] J. Gustavsson, Å. Haglund, J. Vukušić, J. Bengtsson, P. Jedrasik, and A. Larsson, "Efficient and individually controllable mechanisms for mode and polarization

- selection in VCSELs, based on a common, localized, sub-wavelength surface grating," *Opt. Express*, vol. 13, pp. 6626-6634, 2005.
- [26] S. H. Fan, W. Suh, and J. D. Joannopoulos, "Temporal coupled-mode theory for the Fano resonance in optical resonators," *J. Opt. Soc. Am. A*, vol. 20, pp. 569-572, 2003.
- [27] K. Iga, "Surface-emitting laser-its birth and generation of new optoelectronics field," *IEEE J. Sel. Top. Quant. Electron.*, vol. 6, pp. 1201-1215, 2000.
- [28] C. Wilmsen, H. Temkin, and L. A. Coldren, *Vertical-Cavity Surface-Emitting Lasers*. New York: Cambridge University Press, 1999.
- [29] F. Koyama, "Recent advances of VCSEL photonics," *J. Lightwave Technol.*, vol. 24, pp. 4502-4513, 2006.
- [30] W. Hofmann, N. H. Zhu, M. Ortsiefer, G. Bohm, Y. Liu, and M. C. Amann, "High speed (>11 GHz) modulation of BCB-passivated 1.55 μm InGaAlAs-InP VCSELs," *Electron. Lett.*, vol. 42, pp. 976-978, 2006.
- [31] C.C. Kao, Y. C. Peng, H. H. Yao, J. Y. Tsai, Y. H. Chang, J. T. Chu, H. W. Huang, T. T. Kao, T. C. Lu, H. C. Kuo, S. C. Wang, C.F. Lin, "Fabrication and performance of blue GaN-based vertical-cavity surface emitting laser employing AlN/GaN and Ta₂O₅/SiO₂ distributed Bragg reflector," *Appl. Phys. Lett.*, vol 87, pp. 081105, 2005.
- [32] A.N. Baranov, Y. Rouillard, G. Boissier, P. Grech, S. Gaillard, and C. Alibert, "Sb-based monolithic VCSEL operating near 2.2 μm at room temperature," *Electro. Lett.*, vol 34, pp. 281-282, 1998.
- [33] C. J. Chang-Hasnain, J. P. Harbison, G. Hasnain, A. C. Von Lehmen, L. T. Florez, and N. G. Stoffel, "Dynamic, polarization, and transverse mode characteristics of vertical cavity surface emitting lasers," *IEEE Journal of Quantum Electronics*, vol. 27, pp. 1402-9, 1991.
- [34] A. Mizutani, N. Hatori, N. Nishiyama, F. Koyama, and K. Iga, "InGaAs/GaAs vertical-cavity surface emitting laser on GaAs (311)B substrate using carbon auto-doping," *Japanese Journal Appl. Phys.*, vol. 37, pp. 1408-1412, 1998.
- [35] S. J. Schablitsky, Z. Lei, R. C. Shi, and S. Y. Chou, "Controlling polarization of vertical-cavity surface-emitting lasers using amorphous silicon subwavelength transmission gratings," *Applied Physics Letters*, vol. 69, pp. 7-9, 1996.
- [36] J. M. Ostermann, P. Debernardi, and R. Michalzik, "Optimized integrated surface grating design for polarization-stable VCSELs," *IEEE Journal of Quantum Electronics*, vol. 42, pp. 690-8, 2006.

- [37] A. Haglund, J. S. Gustavsson, J. Bengtsson, P. Jedrasik, and A. Larsson, "Design and evaluation of fundamental-mode and polarization-stabilized VCSELs with a subwavelength surface grating," *IEEE Journal of Quantum Electronics*, vol. 42, pp. 231-40, 2006.
- [38] K. D. Choquette, K. M. Geib, C. I. H. Ashby, R. D. Twesten, O. Blum, H. Q. Hou, D. M. Follstaedt, B. E. Hammons, D. Mathes, and R. Hull, "Advances in selective wet oxidation of AlGaAs alloys," *IEEE Journal of Selected Topics in Quantum Electronics*, vol. 3, pp. 916-26, 1997.
- [39] Y.A. Wu, G. S. Li, W. Yuen, C. Caneau, C. J. Chang-Hasnain, "High-yield processing and single-mode operation of passive antiguide region vertical-cavity lasers," *IEEE Journal of Selected Topics in Quantum Electronics*, vol. 3, pp. 429-434, 1996.
- [40] A. Haglund, J. S. Gustavsson, J. Vukusic, P. Modh, and A. Larsson, "Single fundamental-mode output power exceeding 6 mW from VCSELs with a shallow surface relief," *IEEE Photonics Technology Letters*, vol. 16, pp. 368-70, 2004.
- [41] A. J. Danner, J. J. Raftery, Jr., P. O. Leisher, and K. D. Choquette, "Single mode photonic crystal vertical cavity lasers," *Applied Physics Letters*, vol. 88, pp. 91114-1-3, 2006.
- [42] S. Zankovych, T. Hoffmann, J. Seekamp¹, J-U. Bruch and C.M. Sotomayor Torres, "Nanoimprint lithography: challenges and prospects", *Nanotechnology*, vol. 12, pp. 91-95, 2001.
- [43] Connie J. Chang-Hasnain, "VCSEL For Metro Communications", *Chapter in Optical Fiber Communications, IV A, Components*, pp. 666-698, ed. Ivan Kaminow and Tingye Li, Academic Press, 2002.
- [44] C. J. Chang-Hasnain, "Tunable VCSEL," *IEEE J. Select. Topics Quantum Electron.*, vol. 6, pp. 978-987, 2000.
- [45] S. Decai, W. Fan, P. Kner, J. Boucart, T. Kageyama, Z. Dongxu, R. Pathak, R. F. Nabiev, and W. Yuen, "Long wavelength-tunable VCSELs with optimized MEMS bridge tuning structure," *IEEE Photon. Technol. Lett.* vol. 16, pp. 714-716, 2004.
- [46] F. Riemenschneider, M. Maute, H. Halbritter, G. Boehm, M. C. Amann, and P. Meissner, "Continuously tunable long-wavelength MEMS-VCSEL with over 40-nm tuning range," *IEEE Photon. Technol. Lett.* vol. 16, pp. 2212-2214, 2004.
- [47] M. C. Y. Huang, K. B. Cheng, Y. Zhou, B. Pesala, C. J. Chang-Hasnain, and A. P. Pisano, "Demonstration of piezoelectric actuated GaAs-based MEMS tunable VCSEL," *IEEE Photon. Technol. Lett.* vol. 18, pp. 1197-1199, 2006.

- [48] J. S. Harris, Jr., "Tunable long-wavelength vertical-cavity lasers: the engine of next generation optical networks?" *IEEE J. Select. Topics Quantum Electron.* vol. 6, pp. 1145-1160, 2000.
- [49] C. F. R. Mateus, M. C. Y. Huang, C. J. Chang-Hasnain, J. E. Foley, R. Beatty, P. Li, and B. T. Cunningham, "Ultra-sensitive immunoassay using VCSEL detection system," *Electron. Lett.* vol. 40, pp. 649-651, 2004.
- [50] M. Lackner, M. Schwarzott, F. Winter, B. Kogel, S. Jatta, H. Halbritter, and P. Meissner, "CO and CO₂ spectroscopy using a 60 nm broadband tunable MEMS-VCSEL at 1.55 μ m," *Opt. Lett.* vol. 31, pp. 3170-3172, 2006.
- [51] S. Knappe, P. Schwindt, V. Shah, L. Hollberg, J. Kitching, L. Liew, and J. Moreland, "A chip-scale atomic clock based on 87Rb with improved frequency stability," *Opt. Express*, vol. 13, pp. 1249-1253, 2005.
- [52] J. Kitching, "Miniature atomic clock makes its debut," *Opto & Laser Europe*, pp. 22-3, 2004.
- [53] D. Armani, T. Kippenberg, S. Spillane, and K. Vahala, "Ultra-high-Q toroid microcavity on a chip," *Nature*, vol. 421, pp. 925-928, 2003.
- [54] T. Asano, B.-S. Song, Y. Akahane, and S. Noda, "Ultrahigh-Q nanocavities in two-dimensional photonic crystal slabs," *IEEE J. Sel. Top. Quantum Electron.*, vol. 12, pp. 1121-1134, 2006.
- [55] D. Ohnishi, T. Okano, M. Imada, and S. Noda, "Room temperature continuous wave operation of a surface-emitting two-dimensional photonic crystal diode laser," *Opt. Express*, vol. 12, pp. 1562-1568, 2004.
- [56] W.-H. Chang, W.-Y. Chen, H.-S. Chang, T.-P. Hsieh, J.-I. Chyi, and T.-M. Hsu, "Efficient single-photon sources based on low-density quantum dots in photonic-crystal nanocavities," *Phys. Rev. Lett.*, vol. 96, pp. 117401-1-117401-4, 2006.
- [57] H. Takano, Y. Akahane, T. Asano, and S. Noda, "In-plane-type channel drop filter in a two-dimensional photonic crystal slab," *Appl. Phys. Lett.*, vol. 84, pp. 2226-2228, 2004.
- [58] E. Chow, A. Grot, L. Mirkarimi, M. Sigalas, and G. Girolami, "Ultracompact biochemical sensor built with two-dimensional photonic crystal microcavity," *Opt. Lett.*, vol. 29, pp. 1093-1095, 2004.
- [59] J. Niehusmann, A. Vörckel, P. H. Bolivar, T. Wahlbrink, W. Henschel, and H. Kurz, "Ultrahigh-quality-factor silicon-on-insulator microring resonator," *Opt. Lett.*, vol. 29, pp. 2861-2863, 2004.

- [60] A. Löffler, J. Reithmaier, G. Sek, C. Hofmann, S. Reitzenstein, M. Kamp, and A. Forchel, "Semiconductor quantum dot microcavity pillars with high-quality factors and enlarged dot dimensions," *Appl. Phys. Lett.*, vol. 86, pp. 111105, 2005.
- [61] H. A. Haus and Y. Lai, "Narrow-band distributed feedback reflector design," *J. Lightwave Technol.*, vol. 9, pp. 754-760, 1991..
- [62] R. Magnusson and S. Wang, "New principle for optical filters," *Appl. Phys. Lett.*, vol. 61, pp. 1022-1024, 1992.
- [63] S. Peng and G. M. Morris, "Experimental demonstration of resonant anomalies in diffraction from two-dimensional gratings," *Opt. Lett.*, vol. 21, pp. 549-551, 1996.
- [64] M. Neviere, R. Petit and M. Cadilhac, "About the theory of optical crating coupler-waveguide systems," *Opt. Comm.*, vol. 8, pp. 113-117, 1973.
- [65] C. F. R. Mateus, M. C. Y. Huang, J. E. Foley, P. R. Beatty, P. Li, B. T. Cunningham, and C. J. Chang-Hasnain, "Compact label-free biosensor using VCSEL-based measurement system," *IEEE Photon. Technol. Lett.*, vol. 16, pp. 1712, 2004.
- [66] M. Lu, S. S. Choi, C. J. Wagner, J. G. Eden and B. T. Cunningham, "Label free biosensor incorporating a replica-molded, vertically emitting distributed feedback laser" *Appl. Phys. Lett.*, vol. 92, pp. 261502, 2008.
- [67] J. P. Kim and A. M. Sarangan, "Temperature-dependent Sellmeier equation for the refractive index of Al_xGa_{1-x}As," *Opt. Lett.*, vol. 32, pp. 536, 2007.
- [68] H.Ou " Different index contrast silica-on-silicon waveguides by PECVD," *Electron. Lett.*, vol. 2, pp. 212-213, 2003.
- [69] P. Y. Yu and M. Cardona, *Fundamentals of Semiconductors: Physics and Material Properties*, Springer, 2001.
- [70] J. N. McMullin, R. Narendra and C. R. James, "Hollow metallic waveguides in silicon V-grooves," *IEEE Photon. Technol. Lett.*, vol. 5, pp. 1080-1082, 1993.
- [71] Y. Sakurai and F. Koyama, "Control of group delay and chromatic dispersion in tunable hollow waveguide with highly reflective mirrors," *Jpn. J. Appl. Phys.*, vol. 43, pp. 1091-1093, 2004.
- [72] P. Roberts, F. Couny, H. Sabert, B. Mangan, D. Williams, L. Farr, M. Mason, A. Tomlinson, T. Birks, J. Knight, and P. St. J. Russell, "Ultimate low loss of hollow-core photonic crystal fibres," *Opt. Express*, vol. 13, pp. 236-244, 2005.

- [73] H. K. Tsang, C. S. Wong, T. K. Liang, I. E. Day, S. W. Roberts, A. Harpin, J. Drake, and M. Asghari "Optical dispersion, two-photon absorption and self-phase modulation in silicon waveguides at 1.5 μm wavelength", *Appl. Phys. Lett.*, vol. 80, pp. 416-418, 2002.
- [74] K. Jackson, S. Newton, B. Moslehi, M. Tur, C. Cutler, J. Goodman, H. J. Shaw, "Optical fiber delay-line signal processing," *IEEE Trans. Microwave Theory Tech.*, vol. 33, pp. 193-204, 1985.